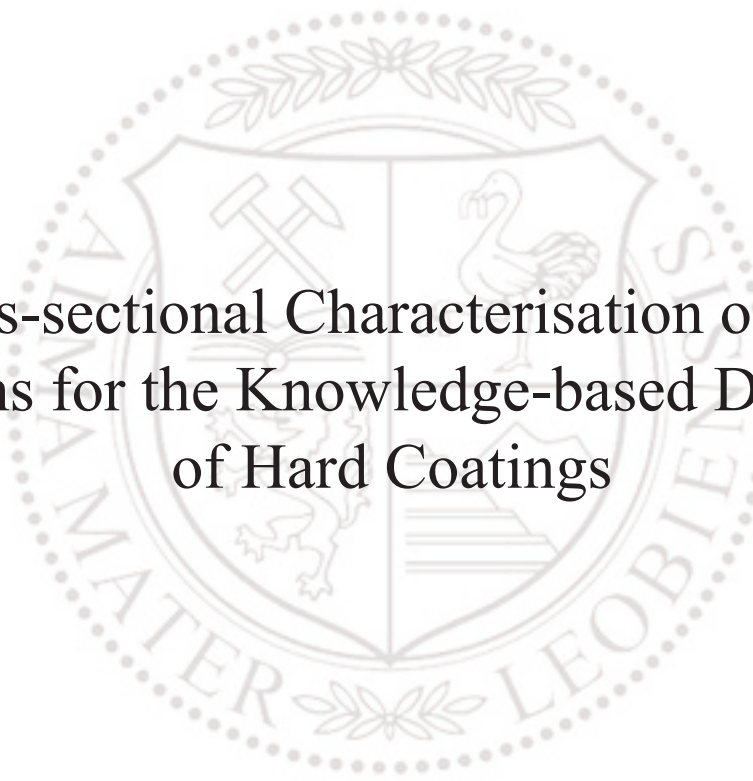




Chair of Materials Physics

Doctoral Thesis



Cross-sectional Characterisation of Thin
Films for the Knowledge-based Design
of Hard Coatings

Mag.rer.nat. David Gruber

January 2021

Eidesstattliche Erklärung

I declare on oath, that I wrote this thesis independently, did not use other than the specified sources and aids, and did not otherwise use any unauthorised aids.

I declare that I have read, understood and complied with the guidelines of the senate of Montanuniversität Leoben for *good scientific practice*.

Furthermore, I declare that the electronic and printed versions of the submitted thesis are identical, both formally and with regard to content.

Leoben, Januar 2021

David Gruber



MONTANUNIVERSITÄT · LEOBEN
DEPARTMENT · FÜR · WERKSTOFF-
WISSENSCHAFT · LEHRSTUHL
FÜR · MATERIALPHYSIK · 2021

Nothing dates faster than people's fantasies about the future.

Robert Hughes
The Shock of the New, 1979

Danksagung

Wissenschaft in unserer Zeit ist nur denkbar als wissenschaftliches Zusammenarbeiten. Dies hier ist der Ort, all jenen meinen Dank auszusprechen, die Anteil haben am Werden dieser Dissertation.

Mein aufrichtigster Dank gilt zuallererst meinem Doktorvater Prof. Jozef Kečkéš, der mich durch all die Jahre und Phasen dieses Dissertationsvorhabens geleitet und begleitet hat. Er war mir in allen Lagen ein wahrer Mentor. Seine wissenschaftlichen Ratschläge und breiter Erfahrungsschatz haben erheblichen Anteil am Entstehen dieser Arbeit.

Ausdrücklich danken will ich auch Prof. Christian Mitterer, der diese Arbeit als Zweitbetreuer begleitet hat. Die Zusammenarbeit mit ihm war hervorragend, ich konnte stets auf seine Unterstützung bauen.

Besonderes Augenmerk möchte ich auf die Unterstützung richten, die mir durch Kommilitonen und Kollegen der Montanuniversität Leoben und des Erich-Schmid-Instituts für Materialwissenschaft zuteil wurde. Michael Meindlhumer, Michael Tkadletz und Juraj Todt standen mir allezeit mit Rat und Unterstützung in theoretischen wie experimentellen Fragen zur Seite. Jakub Zálešák versorgte mich mit brillanten TEM-Aufnahmen und führte mich in die Probenpräparation mit fokussierten Ionenstrahlen ein. Tobias Ziegelwanger war mir eine große Hilfe bei mikromechanischen Versuchen.

Zahlreiche Proben für Nano-Diffraktions-Experimente bedurften aufwendiger Präparation – hier habe ich Gabriele und Herwig Felber, Daniela Kečkéšova und Peter Kutleša vom Erich-Schmid-Institut für ihre Unterstützung zu danken.

Ferner danke ich Thomas Klünsner und Bernhard Sartory vom Materials Center Leoben für ihre freundliche Unterstützung.

Schlüsselexperimente dieser Dissertation wurden an den Synchrotron-Strahlungsquellen ESRF in Grenoble und PETRA III, DESY in Hamburg durchgeführt. Ich möchte mich an dieser Stelle für die erfahrene Unterstützung und erfolgreiche Zusammenarbeit bei den Mitarbeitern der Beamlines ID13 und ID16B am ESRF, sowie der Beamline P05 an PETRA III, DESY herzlich bedanken.

Für die hervorragende Projektzusammenarbeit danke ich auch Christoph Czettel von CERATIZIT Austria.

Zuletzt möchte ich den Blick auf meine Familie und Freunde lenken, die mich durch diese wunderbare Doktorandenzeit begleitet haben. Ich danke euch für die schönen gemeinsamen Stunden.

Die vorliegende Arbeit wurde durch finanzielle Mittel aus dem Programm COMET im Rahmen des K2-Zentrums Integrated Computational Material, Process and Product Engineering (IC-MPPE), Projekt-Nr. 859480 unterstützt. Dieses Programm wurde gefördert durch die Bundesministerien für Verkehr, Innovation und Technologie (BMVIT) und Digitalisierung und Wirtschaftsstandort (BMDW), vertreten durch die Österreichische Forschungs-Förderungsgesellschaft (FFG), sowie die Länder Steiermark, Oberösterreich und Tirol. Ferner wird die Nutzung von Forschungsinfrastruktur an den Synchrotron-Beamlines ID16B und ID13 am ESRF in Grenoble, Frankreich, sowie der Beamline P05 an PETRA III, DESY in Hamburg, Deutschland honoriert.

Für Teile dieser Arbeit konnte experimentelle Infrastruktur von CEITEC-Nano in Brünn, Tschechien verwendet werden.

Acknowledgements

Science in our days is, more than ever before, a collaborative process. This is the place to express my gratitude to all the people who have a share in the making of this work.

I would like to express my deepest gratitude to my supervisor Prof. Jozef Kečkéš who, through all the years and stages of this dissertation project, was a true mentor to me. I owe much to his extensive scientific advice and wealth of experience.

My grateful thanks are also extended to Prof. Christian Mitterer for co-supervising this thesis. He was very supportive and provided valuable feedback.

I am particularly grateful for the invaluable support, advice and intellectual stimulus from my former colleagues at Montanuniversität Leoben and Erich Schmid Institute. Michael Meindlhumer, Michael Tkadletz and Juraj Todt advised me in a wide range of theoretical and experimental topics, offering their specialist knowledge, support and experience whenever needed. Jakub Zálešák provided me with magnificent TEM micrographs and introduced me to the intricacies of focused ion beam milling. When conducting micro-mechanical experiments, I could always count on the excellent support of Tobias Ziegelwanger.

Technical staff at Erich Schmid Institute was very supportive in the preparation and manipulation of samples for nano-diffraction experiments and electron microscopy. In particular I would like to thank Gabriele and Herwig Felber, Daniela Kečkéšová and Peter Kutleša. I am furthermore grateful for the advice and assistance given by Thomas Klünsner and Bernhard Sartory of Materials Center Leoben.

Experiments for this thesis have been conducted at synchrotron light sources ESRF, Grenoble and PETRA III, DESY, Hamburg. The scientific and technical support from beamline scientists at beamlines ID13 and ID16B at ESRF and PO5 at PETRA III is highly appreciated.

I would also like to thank Christoph Czettel of CERATIZIT Austria GmbH for the excellent co-operation in our joint project.

Finally, I would like to draw my attention to my family and friends who accompanied me through this marvellous PhD time. I thank you for the many pleasant hours we spent together.

This work was financially supported by project COMET within the K2 centre Integrated Computational Material, Process and Product Engineering (IC-MPPE), project no. 859480) This programme was supported by the Austrian federal ministries for transport, innovation and technology (BMVIT) and for digital and economic affairs (BMDW), represented by the Austrian research funding association (FFG), and the federal states of Styria, Upper Austria and Tyrol.

Use of research infrastructure at synchrotron beamlines ID16B and ID13 at ESRF, Grenoble, France and PO5 at PETRA III, DESY, Hamburg, Germany is gratefully acknowledged.

For parts of this work experimental infrastructure was used at CEITEC Nano, Brno, Czech Republic.

Kurzfassung

Dünne Schichten kommen aufgrund ihrer speziellen funktionalen Eigenschaften in einem breiten Anwendungsspektrum zum Einsatz. Eines ihrer Einsatzgebiete ist der Schutz zerspanender Werkzeuge durch Beschichtung mit Hartstoffschichten, wobei Werkzeuglebensdauer und -leistung erheblich gesteigert werden können.

Dabei liegen bei den meisten Dünnschichten Querschnitts- (d.h. Tiefen-)gradienten der Mikrostruktur vor. Äquivalente Gradienten sind bei den mechanischen und funktionalen Eigenschaften zu beobachten. Diese Gradienten können Folge des Schicht-Abscheidvorganges aus der Gasphase sein, oder nachträglich durch äußere Faktoren (mechanische oder thermische Belastung, Oxidation) eingebracht werden. Sie erweisen sich als leistungskritisch in einer Vielzahl von Anwendungsfällen, so auch beim Einsatz beschichteter Schneidwerkzeuge. Ihre Charakterisierung ist von entscheidender Bedeutung für das Auffinden von Struktur-Eigenschafts-Beziehungen und die darauf aufbauende wissensbasierte Weiterentwicklung funktionaler Dünnschichten.

Die Abbildung dieser Gradienten, stellt dabei hohe Anforderungen an die Ortsauflösung der verwendeten Untersuchungsverfahren. Um den Querschnittsverlauf nano-skaliertter Schichtstrukturen und -eigenschaften aufzulösen, wurden im Rahmen dieser Arbeit *Synchrotron-Röntgen-Nanobeugung*, *Nanoindentation*, *Elektronenmikroskopie* sowie *Experimente mit Mikro-Biegebalken* eingesetzt.

Neben der entscheidenden Rolle von Struktur- und Eigenschaftsgradienten in Hartstoffschichten auf Schneidwerkzeugen, ist auch das Verhalten des schichtnahen Substratbereiches von erheblichem Interesse für das Verständnis und die Modellierung von Zerspanungsvorgängen. Ein Teil dieser Arbeit befaßt sich daher mit der Untersuchung des Verhaltens schichtnaher WC-Co-Regionen unter zyklischer thermischer Belastung durch Laserbestrahlung.

Die vorliegende Arbeit stellt zwei Modellfälle querschnittsaufgelöster, nano-analytischer Charakterisierungen von Dünnschichten vor, während eine dritte Studie sich mit Plastifizierungsvorgängen in schichtnahen WC-Co-Substratregionen beschäftigt. Bei den vorgestellten Studien handelt es sich um:

- Die Anwendung von Synchrotron-Röntgen-Nanobeugung, Transmissions-Elektronenmikroskopie und In-situ-Experimenten mit Mikro-Biegebalken zur querschnittsaufgelösten Charakterisierung des Oberflächen-Oxidationsverhaltens einer CVD-TiN/TiB₂-Hartstoffschicht. Dabei konnte die Auswirkung der Oxidation auf Gradienten von Mikrostruktur, Eigenspannungszustand und mechanische Eigenschaften en détail untersucht, und die ausgeprägte Oxidationsbeständigkeit der TiB₂-Schichtlage bestätigt werden.

- Die querschnittsaufgelöste Untersuchung einer CVD-Diamantschicht, bestehend aus jeweils einer nanokristallinen wie einer polykristallinen Schichtlage. Unter Verwendung von Synchrotron-Röntgen-Nanobeugung, Elektronen-Rückstreubeugung, Nanoindentation und Mikro-Biegebalken-Versuchen konnten komplexe Beziehungen der Gradienten von Mikrostruktur, Eigenspannungszustand, mechanischen Eigenschaften und angewandten Abscheidebedingungen ermittelt werden.
- Den Einsatz eines komplexen experimentellen Aufbaus, bei dem Synchrotron-Röntgenbeugung in Kombination mit punktueller Laserbestrahlung von mit TiCN und α -Al₂O₃ beschichteten WC-Co-Wendeschneidplättchen angewandt wurde. Dies ermöglichte die Aufzeichnung von Temperatur- und Spannungsverläufen in lokal erhitzten schichtnahen Substratbereichen bei zeitlicher Auflösung im Millisekunden-Bereich. Diese Daten gewähren detaillierten Einblick in die Plastifizierungsmechanismen des WC-Co-Verbundes.

Abstract

Thin films are used in a wide range of applications due to their unique functional properties. One particular role is the protection of cutting and milling tools by hard thin coatings. This results in significantly improved tool lifetime and performance.

Most thin films exhibit cross-sectional (*i.e.* depth) gradients of microstructure, mechanical and functional properties. These gradients can be connected to specific conditions during film growth from the vapour phase, or be the consequence of exposure to post-deposition external factors, *e.g.* mechanical or thermal loads or oxidation. The gradients are decisively linked to functional performance in a large number of thin film applications, including hard coatings on cutting tools. Their characterisation is of critical importance in establishing structure-property relationships and the knowledge-based improvement and design of thin films.

Measuring nano-scale thin film structure and property gradients requires dedicated high-resolution experimental techniques. In order to resolve sub-micrometre thin film features and their physical properties, *synchrotron X-ray nano-diffraction*, *nano-indentation*, *electron microscopy* as well as *micro-cantilever bending experiments* were applied within the framework of this thesis.

In addition to the critical role of structure and property gradients within thin protective coatings on cutting tools, also the behaviour of the coating-near substrate region is of great interest for the understanding and modelling of cutting and milling processes. Part of this thesis is concerned with investigating the behaviour of substrate-near WC-Co regions when subjected to cyclic thermal shocks by laser irradiation.

This thesis presents two model cases of cross-sectional nano-analytics based characterisation of thin films, while a third study presented examines plastification phenomena in coating-near WC-Co substrate regions. In particular, the presented case studies are:

- A study of the surface-oxidation behaviour of a CVD TiN/TiB₂ protective coating, applying synchrotron X-ray nano-diffraction, transmission electron microscopy and in-situ micro-cantilever experiments. This allowed to examine the effect of surface oxidation on gradients of microstructure, residual stress and mechanical properties in detail, proving the favourable oxidation resistance of the TiB₂ sublayer.
- A cross-sectional study of a CVD diamond coating, consisting of a nanocrystalline bottom layer and a coarse-grained polycrystalline top layer. Complex cross-sectional correlations between thin film microstructure, residual stress, mechanical properties and

deposition conditions could be revealed by synchrotron X-ray nano-diffraction, transmission electron microscopy and in-situ micro-cantilever experiments.

- A study involving a complex synchrotron X-ray diffraction set-up with in-situ laser pulsing to characterise the time-dependent evolution of stresses and microstructure in locally irradiated WC-Co inserts coated with CVD with TiCN and α -Al₂O₃ films. With this set-up, the temperature and time dependent development of stress levels within the coating-near WC-Co substrate region could be recorded at millisecond time resolution. The acquired data provided detailed insight into the WC-Co composite plastification mechanism which governed the stress build-up and relaxation in the substrate material.

Contents

Danksagung	vii
Acknowledgement	ix
Kurzfassung	xi
Abstract	xv
1 Introduction	1
1.1 Thin films and hard coatings	1
1.2 Motivation and research contributions	2
2 Thin film synthesis	5
2.1 Physical vapour deposition	5
2.2 Chemical vapour deposition	6
2.3 Film growth and post-deposition treatment	8
3 Thin film characterisation	11
3.1 X-ray diffraction	11
3.1.1 Synchrotron XRD and nano-diffraction	12
3.1.2 Phase analysis	16
3.1.3 Crystallographic texture analysis	17
3.1.4 Morphology analysis	18
3.1.5 Stress analysis	19
3.2 Micromechanical testing	21
3.2.1 Nanoindentation	21
3.2.2 Micro-cantilever bending	24
4 Conclusions and outlook	29
References	32
List of appended publications	43
Publication A	45
Publication B	67
Publication C	87
List of acronyms	105

1 Introduction

1.1 Thin films and hard coatings

Surface modifications of objects have been used at least since early antiquity with the aim of achieving desired aesthetic or functional characteristics. Throughout history, man has utilised the unique properties of artificially crafted surfaces, be it to save precious materials or to produce objects with qualities inherent to their surface treatment, possessing qualities that reach beyond those achievable in bulk materials [1, 2]. As we stride ahead further into the new millennium, thin film materials, thin coatings and related materials systems are used in a multitude of roles, exploiting their specific inherent (physical, chemical, electronic, tribological, etc) properties or combinations of properties [3, 4]. Modern fields of application are, by implication, as varied as the spectrum of specific properties, ranging from optics [5], medical engineering [6] and tool protection [7, 8] to microelectronics and battery technology.

Most taxonomies distinguish between thin films used for their specific *electronic* properties, *e.g.* in semiconductor components, *optical* films, *e.g.* as anti-reflection coatings and *protective* coatings, shielding vulnerable parts from adverse conditions such as mechanical and thermal loads or detrimental chemical reactions. *Thermal* properties can be exploited in heat-barrier and transfer layers, while coatings with special *tribological* characteristics can serve in environments where friction is critical. Thin films are usually synthesised either by physical or chemical vapour deposition techniques, as outlined in Sec. 2.1 [1, 9].

This thesis is mostly concerned with hard protective thin films used as coatings to protect cutting tools, their cross-sectional characterisation and design. The terms *thin film* and *coating* are henceforth used synonymously to refer to a layer or architecture of layers with a typical thickness in the range of up to several micrometres, deposited onto a substrate.

The advanced economies and material wealth of our time could not possibly exist without the industrial and manufacturing processes and techniques, of which a significant number rely on the cutting and machining of metals and alloys of various kinds. Today's ceramic thin film coatings employed on state-of-the-art cemented carbide cutting tools allow for high performance cutting and milling operations in a number of roles, owing to their specific physical, chemical and operational characteristics [7, 10]. The coatings have to withstand severe mechanical and thermal loads with temperatures reaching up to 1000 °C [11]. Their required set of properties combines high hardness, high Young's modulus and fracture toughness, as well as superior resistance to oxidation and wear [12]. Modern hard protective coatings come in a range of designs and microstructural architectures,

which serves as key for their outstanding performance [7, 8, 10]. Since their commercial beginnings in the 1970s, these coatings for tools have undergone a steady evolution from simple mono-layer structures to complex, multilayered architectures with tailored microstructures, stress states, property gradients and functional characteristics [13, 14].

1.2 Motivation and research contributions

The overarching theme of this thesis is the combined application of established and relatively novel, advanced characterisation techniques in the measurement of micro- and nano-scale gradients of protective thin film microstructure, physical and functional properties, as used for establishing structure-property relationships. This characterisation step, in particular of sub-micrometre and nanoscale properties and property gradients is crucial in the coating design process, closing the feedback loop between coating synthesis, post-deposition treatment and knowledge-based enhancement of coating performance. In particular, the key focus was put on employing state-of-the-art cross-sectional characterisation methods and in-situ based techniques. Three independent pieces of research are presented, which have been published in peer reviewed specialist journals. Two of the studies represent cross-sectional thin film investigations where nano-focussed synchrotron X-ray diffraction (CSnanoXRD) played a pivotal role in revealing various depth gradients of phase, microstructure and residual stress state. The third study employed a complex synchrotron X-ray diffraction (XRD) set-up coupled with in-situ laser pulsing, which was used to reveal plastification phenomena in coated cemented carbide substrates.

In detail, the three presented case studies (appended as publications A, B and C) are concerned with

- A the oxidation behaviour, *i.e.* oxidation resistance, of a CVD TiN/TiB₂ protective coating that was deposited onto cemented carbide cutting inserts. Samples were oxidised in ambient air at temperatures of up to 700 °C, which lead to the formation of a rutile TiO₂ oxide film on top of the nanocrystalline TiB₂ coating top layer. Investigations of the coating in as-deposited and oxidised state using CSnanoXRD, scanning transmission electron microscopy, in-situ micro-cantilever bending and various other experimental methods provided a detailed cross-sectional insight into the coating/oxide phase composition and residual stress states as well as into oxidation-induced coating degradation and change of mechanical coating properties.
- B The nano-analytics based cross-sectional study of a CVD diamond thin film which consisted of a nanocrystalline diamond (NCD) bottom layer and a coarse-grained polycrystalline dia-

mond (PCD) top layer deposited onto substrates of Si. To the authors' knowledge, this was the first contribution using csnanoXRD with a nano-focussed beam to investigate a CVD diamond thin film. Complex cross-sectional correlations between thin film microstructure, residual stress state, mechanical properties and deposition conditions could be revealed.

- C The use of a sophisticated synchrotron XRD set-up employing in-situ laser pulsing to characterise the time-dependent evolution of stresses and microstructure in locally irradiated WC-Co cutting inserts coated by CVD with TiCN/ α -Al₂O₃. The experiment was able to measure the temperature and time-dependent evolution of strain and stress levels within the coating-near cemented carbide substrate at millisecond time resolution. This provided detailed insight into the WC-Co composite plastification mechanism which governs the build-up and relaxation of stresses in locally thermo-shocked WC-Co.

2 Thin film synthesis

Thin film synthesis on substrates based on vapour deposition can generally be divided into three sequential phases: (i) vaporising of source material, (ii) transfer of vapourised material to the substrate, potentially including collisions and/or chemical reactions as well as (iii) the actual film growth phase involving condensation, nucleation, coalescence and crystal growth [1, 15, 16].

Historically, the development of vapour deposition is closely related to technological progress in the field of vacuum technology. Today, a multitude of specialised vapour deposition processes exist, differing significantly in terms of involved auxiliary techniques, applied deposition pressure environment, substrate temperature, vapour phase particle energy and film growth rate. In a very general sense, a distinction is drawn between two main groups:

Physical vapour deposition (PVD) relies on vaporising source materials based on physical processes such as thermal heating, irradiation by electron or laser beams, the use of cathodic arcs or bombardment of source material targets by plasma particles, so-called *sputtering*. In contrast the defining characteristic of *chemical vapour deposition* (CVD), which uses gaseous (or vaporised liquid or solid) precursors, are chemical gas phase and adsorbant reactions, which occur during the transport phase, directly on, or in the ultimate vicinity of the substrate. These reactions are activated thermally and may be laser-assisted or assisted kinetically by the use of plasmas [1, 17].

2.1 Physical vapour deposition

PVD processes are performed in low-pressure environments (10^{-5} to 10^{-2} mbar) at substrate temperatures from room temperature up to approximately 600 °C, resulting in relatively small film growth rates when compared to their CVD counterparts. The processes can be subdivided into (i) evaporation-based techniques, such as molecular beam epitaxy and cathodic arc evaporation (CAE), (ii) sputtering and (iii) ion-plating [1]. For the growth of hard protective coatings by means of PVD, mostly CAE and various sputter deposition techniques are of relevance.

In CAE, an electric arc is magnetically steered across a cathode target, vaporising source material from a localised, heated-up cathode spot. The vapour phase material is subsequently transported to the substrate, where film growth proceeds. The process can be operated either in an inert gas environment or using reactive gases [1, 18]. CAE can achieve high ionisation rates, exceeding 90%, but suffers from incorporation of defect-forming droplets into the growing film, which deteriorate film quality and increase surface roughness [18]. In sputter deposition, mostly noble process gases such as Ar are ionised, accelerated and made to collide with a solid source material

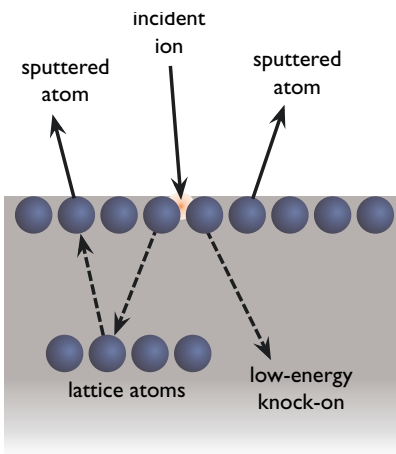


FIGURE 1: Schematic drawing, illustrating momentum transfer processes in sputtering (adapted from [15]).

target, effecting the release of atoms or small clusters. The underlying physical principle is the transfer of momentum between impinging Ar^+ ions and the target material, and the subsequent triggering of collision cascades within the target. Target atoms/compounds are sputtered if their kinetic energy surpasses the binding energy of the respective target material. Fig. 1 shows a schematic drawing of the fundamental momentum transfer processes occurring at the sputter target. *Sputter yield*, which serves as a measure of the efficiency of sputtering, is defined as the quotient of the number of sputtered atoms and the number of incident particles [1]. The primary ionisation (with typical ionisation rates below 1%) is maintained by a glow discharge plasma inside the process chamber. Upon ejection from the target, sputtered vapour-phase source material is transported to the substrate on ballistic trajectories and consequently incorporated into the growing thin film. [10, 19]

Variations of the relatively simple direct current sputtering, where a constant electric field between the cathode target and anode chamber walls is applied, are radio frequency sputtering and magnetron sputtering. As in CAE, reactive process gases like N or O may be employed in order to facilitate the deposition of nitride or oxide films [20].

In contrast to CVD, PVD deposition can be operated at considerably lower temperatures, ranging from room temperature up to $\sim 700^\circ\text{C}$. This comes as a major advantage when working with temperature sensitive substrate materials. By its very nature, PVD is a so-called *line-of-sight process*, meaning that vapour-phase material travels on ballistic trajectories from target to substrate. As a consequence, deposition on substrates which are stepped, contain trenches, cavities and/or other topographical features can be problematic [1, 16].

2.2 Chemical vapour deposition

The thin films and coatings investigated within the scope of this thesis were all deposited by CVD processes. Industrial scale hot-wall CVD plants were used in the deposition of the TiN/TiB₂ (appended publication A) and TiCN/ α -Al₂O₃ coatings (publication C). The bi-layer diamond thin film (publication B) and was grown by microwave plasma-enhanced CVD.

The basic underlying principle in CVD is the use of precursors, which, in the beginning, may be present in either gaseous, liquid or solid form, followed by their volatilisation and subsequent activation of chemical reactions to form a solid film [1, 17]. Volatilisation of solid precursors such as Al, Zr or Hf is usually based on chlorination. In a general sense, CVD processes can be classified by the method used to supply the activation energy required for the CVD reactions to occur [17]. CVD techniques are applied in higher pressure environments ($\sim 100\text{mbar}$ to atmospheric pressure) compared to PVD and rely on elevated substrate temperatures ($\sim 600\text{--}1100^\circ\text{C}$). In order

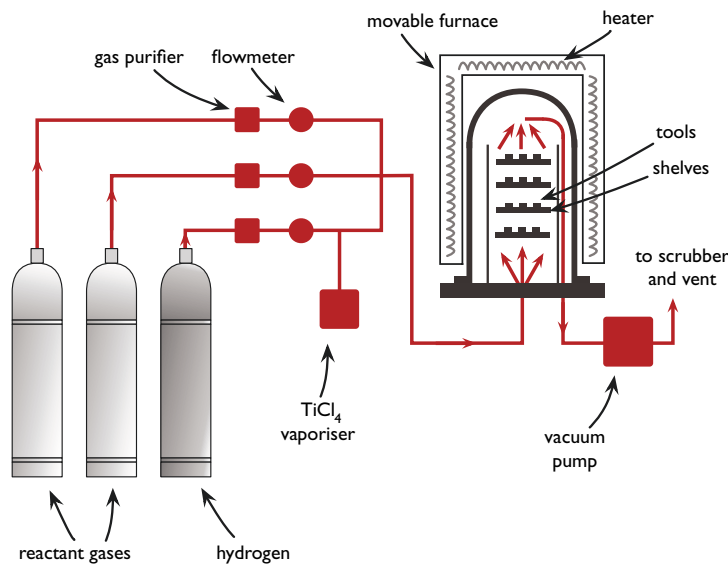


FIGURE 2: Schematic drawing of a hot-wall type CVD plant, as used in the industrial production of cutting tools (adapted from [17]).

to achieve lower operational deposition temperatures, assistive sources of energy, such as plasmas, laser irradiation or microwaves can be integrated into the process to foster chemical reactions. CVD processes have been tailored to meet a broad spectrum of application specific requirements and are therefore employed in a range of different industries. In particular, this is due to the great variety of existing suitable precursor substances. Additional favourable characteristics of CVD include its ability to deposit material on out-of-sight surfaces, *e.g.* on shadowed surfaces or in cavities or trenches, which is referred to as *throwing power*, and the ability to use large deposition reactors, which render the process economical for industrial production.

Hard protective coatings used on cutting tools are primarily deposited by thermally activated PVD in hot-wall type reactors, which allow for close temperature control. Typical associated deposition temperatures are in the range of 700–1100 °C [15, 16, 21, 22]. Fig. 2 shows a highly simplified schematic drawing of a hot wall CVD reactor, as used in the industrial-scale coating of cutting tools.

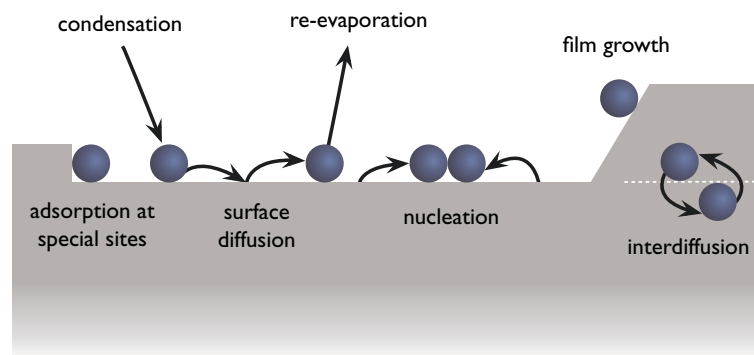
2.3 Film growth and post-deposition treatment

A simplified schematical drawing of different atomic processes involved in thin film growth is shown in Fig. 3. After condensation of an arriving particle onto the substrate, it may diffuse along its surface or gain enough energy to re-evaporate. Edges, impurities or other topographical surface features are preferential low energy sites for adsorption of particles diffusing along the surface. Surface diffusion can furthermore result in the formation of particle clusters, which are referred to as nuclei once they reach a critical size. In addition, interdiffusion of particles between film and substrate can occur. Film growth is the result of continuous film thickening by additional deposition of atoms. [1, 9, 22, 23].

Three basic modes of thin film growth can be distinguished and are related to different binding characteristics of deposited particles and atoms of the substrate. The modes are schematically shown in Fig. 4. Island growth (*Völmer-Weber* type) occurs when bonds between deposition atoms or molecules are stronger than bonds between deposition particles and the substrate. It is characterised by three-dimensional growth of nuclei and the formation of islands. In contrast, layer-by-layer growth (*Frank-van der Merwe* type) can be observed when bonds between atoms of deposited material and the substrate dominate, promoting the closing of individual layers of atoms. A combined growth mode (*Stranski-Krastanov* type) can occur when island growth is favoured after the initial formation of one or several closed mono-layers [1].

In general, the nucleation and growth kinetics, which are closely connected to resulting thin film microstructures, properties and gradients thereof, are strongly influenced by deposition parameters [1, 22]. The relationship between deposition parameters and observed thin film structure can be described in so-called *structure-zone models*. The first such model was presented for films deposited by thermal evaporation by B.A. Movchan and A.V. Demchishin in 1969 [24]. This model has since been revised, modified and extended [25–27]. Post-deposition treatments may be applied to alter thin film characteristics. In the case of hard coatings this serves to enhance per-

FIGURE 3: Schematic drawing of different atomic processes involved in the initial stages and during thin film growth (adapted from [23] and [9]).



formance-critical functional characteristics, in particular concerning tribological properties and residual stress states. This can be achieved by mechanical means, such as blasting with hard media (in wet or dry configuration), polishing or brushing, as well as annealing [22, 28].

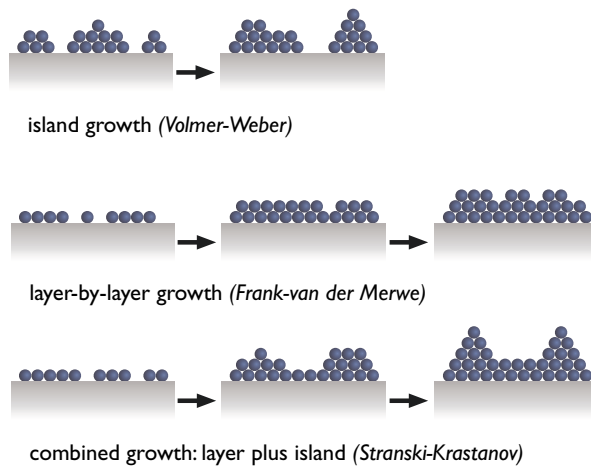


FIGURE 4: Schematic sketch of distinct modes of film growth (adapted from [1]).

3 Thin film characterisation

3.1 X-ray diffraction

Since its beginnings in the first half of the 20th century, X-ray diffraction has fast developed into a versatile and powerful tool for characterising the crystalline structure of materials and substances, and is now being used in fields ranging from chemistry, biochemistry and mineralogy to materials science and physics [1, 29].

The simple, yet fascinatingly elegant phenomenon of X-ray radiation interacting with the regular arrangement of atoms and molecules within crystalline materials to form patterns of diffraction was first experimentally observed by M. von Laue in 1912, proving the wave-like qualities of those rays, which had been of a mysterious nature ever since their discovery by K.W. Röntgen in 1895 [30]. The theoretical framework for relating observed diffraction patterns with scattering crystal structures was established soon thereafter by W.L. and W.H. Bragg, who laid the foundations of modern X-ray crystallography [30, 31].

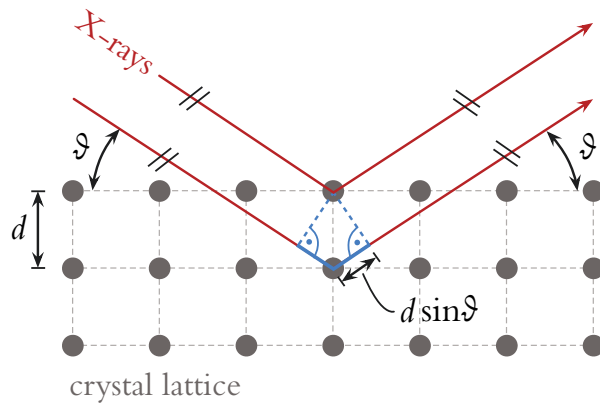
The applicability of XRD rests on the assumption of a material possessing a crystalline nature, which holds true for the large majority of metallic and ceramic materials, including most thin films. This versatility when it comes to the type of material, together with the wealth of information which can be acquired by it, render XRD an indispensable tool in materials research. In particular, a material's XRD pattern can give insight into its (i) crystal structure, *i.e.* phase composition, (ii) distribution of orientation of crystallites, *i.e.* crystalline texture, (iii) the orientation-dependent morphology and size of coherently scattering domains, as well as (iv) residual strains of 1st, 2nd and 3rd order [32].

Individual crystal structures and corresponding crystalline phases can be identified by their characteristic set of lattice planes and inter-atomic spacings. It is the long-range order of the atomic/molecular arrangement within crystalline materials that gives rise to the phenomenon of diffraction as a consequence of constructive/destructive interference of scattered waves. The condition for the constructive interference of X-rays when elastically scattered at the lattice planes of a crystalline solid was first formulated by W.H. Bragg in 1913 and is referred to as *Bragg's equation*,

$$2d \sin \vartheta = n \lambda \quad , \quad (3.1)$$

d being the lattice parameter, ϑ the angle of the incident and scattered ray with respect to the lattice plane (*Bragg's angle*), while λ represents the wavelength of the incident ray and n denotes the order of diffraction. A schematic drawing of Bragg's equation, depicting the scattering of X-ray beams by adjacent lattice planes of a two-dimensional primitive square lattice is presented in Fig. 5.

FIGURE 5: Graphical depiction of Bragg's equation in two dimensions, showing parallel incident X-ray beams being scattered at lattice atoms of a primitive square lattice (adapted from [29] and [32]). Assuming a non-zero structure factor, diffraction of X-rays results if the difference in path lengths between waves scattered at different lattice planes is an integer multiple of the used monochromatic X-ray radiation.



In the case of polycrystalline materials consisting of a large number of small, randomly oriented crystallites (grains), diffraction of monochromatic X-rays results in characteristic cone-shaped patterns of diffracted intensity, so-called *powder diffraction cones*.

3.1.1 Synchrotron XRD and nano-diffraction

Modern laboratory-size X-ray sources used in materials characterisation work at photon energies of $\sim 5\text{--}20\text{ keV}$, resulting in effective sample penetration depths of several micrometres (depending also on the probed material). Thus, information about the crystallographic make-up of most materials can only be acquired from surfaces and surface-near regions, which limits their use to the investigation of surfaces and homogeneous materials [22, 33, 34]. While in reflective experimental geometries, different depth levels of a sample can be discerned and analysed, this complex task is usually constrained by the problem of deconvoluting diffraction signals originating from those distinct depth regions. This renders this option rather impractical for the investigation of most encountered thin film gradients [33, 35–37]. For the study of thin films, having complex architectures, showing film thickness-dependent property gradients and/or sub-micron and nano-scale defects, also the effective X-ray beam diameter has to be in the order of magnitude of those features of interest. Both the deconvolution problem, as well as the limitations in achieving tightly focussed X-ray beams in the sub-micron and/or nanometre regime at reasonable beam intensities, constrain the use of laboratory XRD sources in investigating thin films and coatings.

The inherent problem of beam size versus photon flux can only be overcome by moving to advanced X-ray sources available at dedicated research facilities. Synchrotron light sources provide X-ray radiation at levels of *brilliance* way beyond those attainable with

laboratory devices, making it possible not only to achieve high-flux nanometre-sized beams, but also to penetrate samples of a reasonable thickness, which allows experiments to be performed in transmission geometry [38, 39].

The brilliance of a radiation source is a quantity reflecting the photon flux, beam divergence, source size, as well as the beam's degree of monochromaticity. Synchrotron sources offer tuneable beam energy in combination with a high X-ray radiation flux and small angular divergence at small source size [29]. High brilliance is also key in keeping diffraction pattern acquisition times and thus measurement times low, since beam size and acquisition time can only be reduced at each other's cost. Acquisition time can be especially critical in in-situ experiments, *e.g.* when samples are being subjected to temperature-varying environments, mechanical loads or undergo phase transitions and subsequently high enough frame rates are required to monitor the response in diffraction patterns in real time [40, 41, 42]. Fig. 6 shows the schematic drawing of the experimental set-up used in appended publication C [42] to perform synchrotron XRD measurements on samples subjected to cyclic thermal loads induced by in-situ laser pulsing. For this experiment, high time resolution of the XRD measurement was thus essential.

The approach of probing samples with nano-focussed synchrotron X-ray beams in transmissive geometry proved to be a highly successful method for studying thin films by scanning their depth profiles, *i.e.* cross-sections on carefully prepared lamellae. This technique was introduced with a beam diameter below 100 nm by Keckes *et al.* in 2012 [43, 44] and is referred to as *cross-sectional X-ray nano-diffraction* (CSnanoXRD). It has since been applied to a variety of different thin film samples and undergone continuous refinements and im-

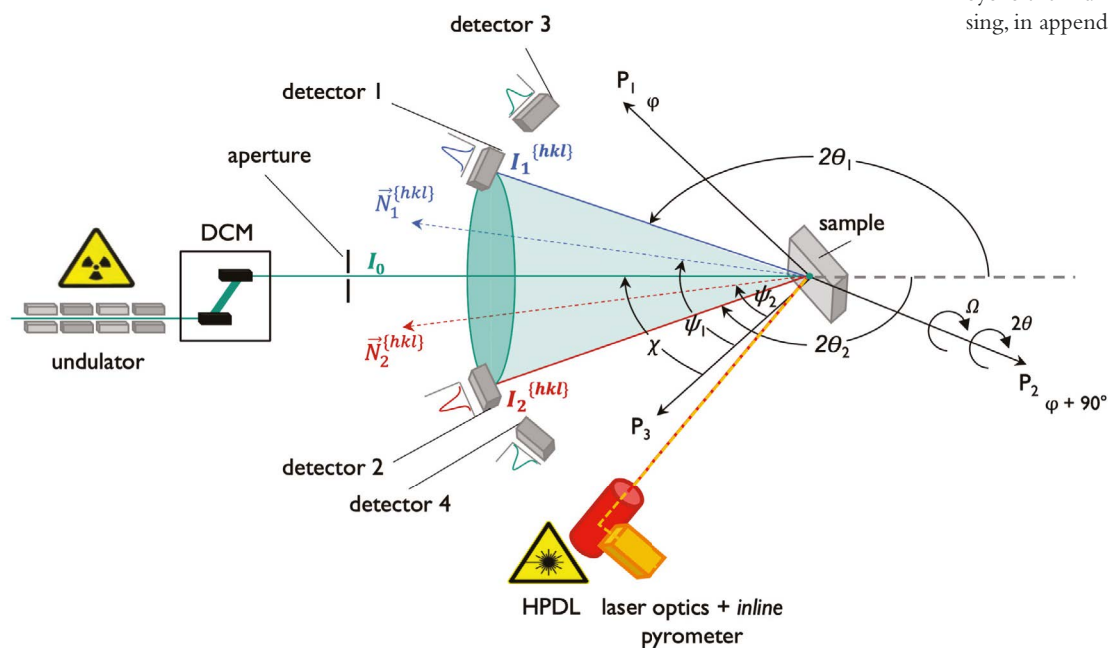
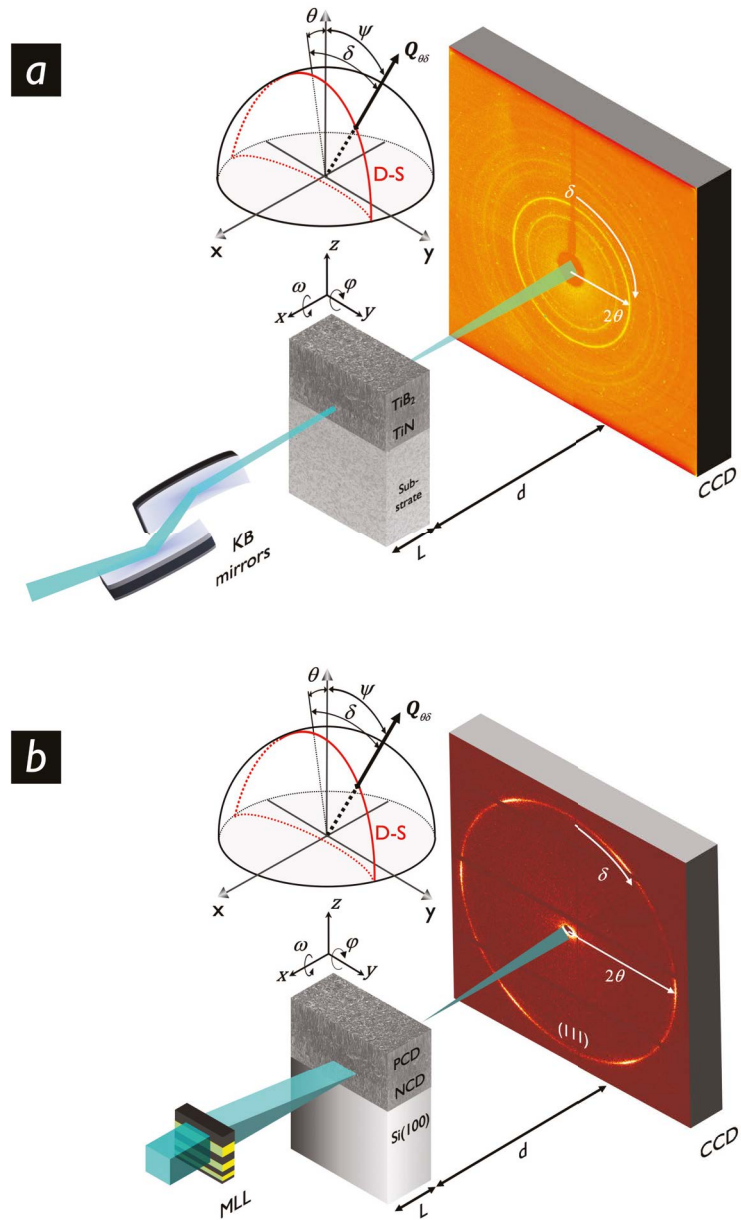


FIGURE 6: Schematic sketch of the experimental in-situ set-up, as used for studying strains, stresses and associated plastification phenomena in near-coating cemented carbide substrate regions subjected to rapid cyclic thermal loads by laser pulsing, in appended publication C.

FIGURE 7: Schematic drawing of csnanoXRD set-ups as used for synchrotron experiments in this work. The set-up shown in (a) was used at beamline ID13 of ESRF to investigate a TiN/TiB₂ hard coating (appended publication A [56]), while the set-up depicted in (b) was employed at beamline ID16B, ESRF for the investigation of a NCD/PCD diamond thin film (appended publication B [57]). Both experiments were performed in transmission geometry, using specialised X-ray focussing optics to achieve nano-focussed beam spots. The set-up presented in (a) used KB mirrors to focus the X-ray beam to a cross-section of $\sim(70 \times 70)$ nm, while the set-up shown in (b) employed a multilayer Laue lens for beam focussing, resulting in a pencil-shaped beam of dimensions $\sim 70 \mu\text{m} \times 30$ nm. For both experimental configurations, piezo-actuated stages were used to stepwise move the sample lamellae in z -direction, resulting in a scanning of the investigated thin films on the cross-section. The resulting diffraction cones were recorded as Debye-Scherrer rings at every z -position on a CCD detector and subsequently processed and analysed by specialist software.



improvements, owing to developments in X-ray optics and sources, experiment design and data treatment [45, 46, 47]. Since its introduction csnanoXRD was used in experiments on thin films in as-deposited as well as in modified (annealed, oxidised, post-indentation) state, including curved film geometries, revealing complex gradients of phase composition, stress state, texture and crystallite size [12, 48–55]. csnanoXRD features as a key experiment in appended publications A and B [56, 57].

Fig. 7a&b depicts two schematic drawings of csnanoXRD experimental set-ups used for experiments presented in this work. The principal configuration consists of (i) X-ray optical components to

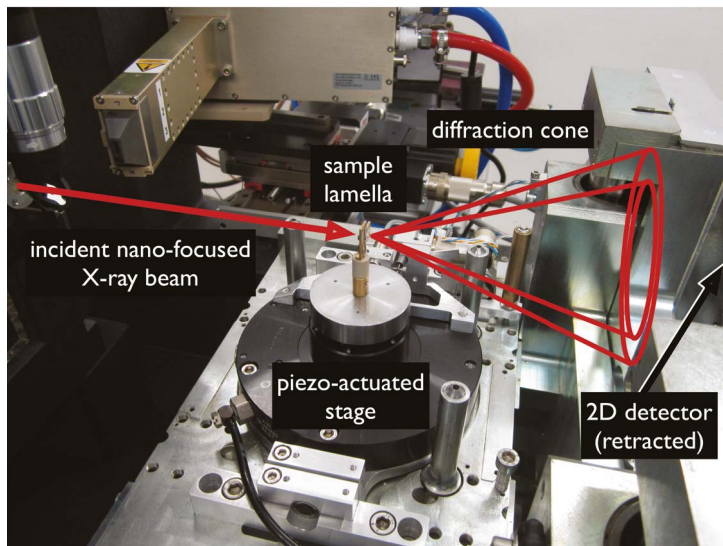


FIGURE 8: csnanoXRD measurement configuration at beamline ID16B, ESRF, as used in the experiments for appended publication A. The 2D CCD detector is in a retracted position and not visible on the image.

focus the incident synchrotron beam to required nano- or micro size dimensions, (ii) a sample lamella, mounted on a piezo-actuated stage and (iii) a two-dimensional (2D) charge-coupled device (CCD) detector at positioned perpendicular to the incoming beam at distance d to the sample, to record emerging 2D powder diffraction patterns. The resulting intensity distribution within the diffraction cone emanating from the centre of diffraction can be recorded as so-called *Debye-Scherrer* (DS) rings on the detector (*cf.* Fig. 7a & b). Sample lamellae are prepared by mechanical methods and polished to a thickness $L \sim 50\text{--}100\mu\text{m}$, being thick enough to allow simple manual manipulation while being transparent for the high-energy X-ray beam. Beam focussing optics is based on *Kirkpatrick-Baez* (KB) mirrors, compound refractive lenses or *multilayer-Laue lenses* (MLL). Rectangular, *i.e.* pencil-shaped beam dimensions, as depicted in Fig. 7b, allow high resolution scanning along the z -axis, while at the same time illuminating a many times larger number of individual crystallites due to their extended width along the y -axis. This can significantly benefit diffraction statistics and thus the quality of evaluated data. Scanning of samples can either be performed along one single axis (so-called *line scanning*, usually in z -direction) or using combined y and z motor movements to scan meshes of cross-sectional lamella regions. A 2D detector image is recorded for every single scan step, representing the specific diffractive characteristics of this cross-sectional lamella spot. Fig. 8 shows an annotated photograph of the csnanoXRD set-up used at beamline ID16B, ESRF, as used in the experiment carried out in appended publication A.

3.1.2 Phase analysis

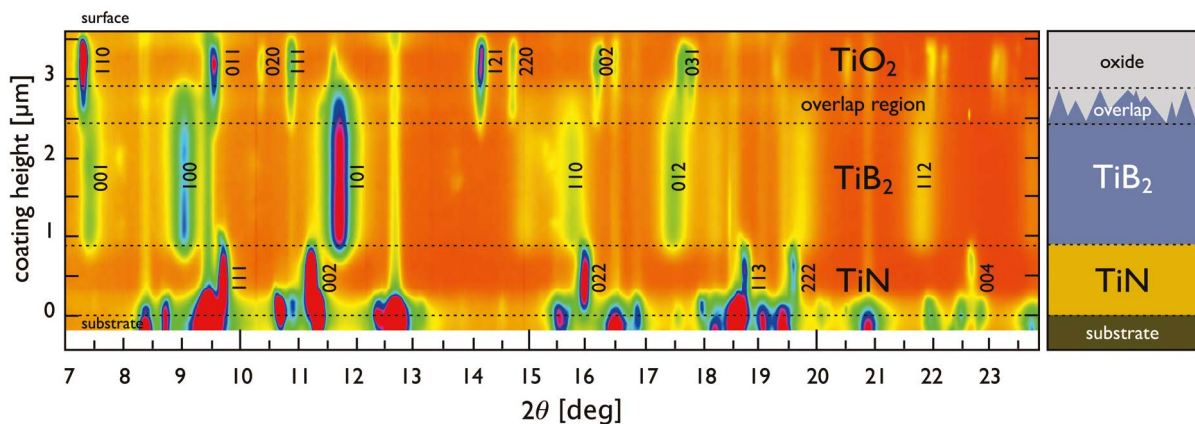
The sequential order of Debye-Scherrer rings as recorded in csnanoxrd experiments on a 2D detector can directly be related to the sequence of intensity peaks as measured by laboratory XRD in Bragg-Brentano (reflective) geometry. Profiles $I(\vartheta)$, equivalent to laboratory $(\vartheta-2\vartheta)$ -measurements, can be retrieved from 2D detector images by integrating recorded intensity along DS rings, so-called *azimuthal integration*. This integration step requires precise information about the powder diffraction experimental geometry, *i.e.* exact distances and angles of the detector with respect to the centre of diffraction [58–60], which can be found by measuring a sample of a material with precisely known powder diffraction characteristics. This usually involves recording the diffraction pattern of a ready-made calibration standard consisting *e.g.* of LaB_6 .

Azimuthal integration is usually performed by specialised software, optimised for this specific task. The csnanoxrd data acquired for experiments presented in publications A and B were processed with a software package named *pyFAI* featuring dedicated, highly efficient integration algorithms [61]. An accompanying user interface developed at the chair of materials physics of Montanuniversität Leoben facilitated data handling and processing.

Integrated diffraction intensity profiles $I(\vartheta)$ relate to individual detector images, and thus to specific thin film depth positions in case of a line scan in z -direction. They can be condensed into a contour plot of intensity as a function of diffraction angle and film depth, $I(\vartheta, z)$. This is referred to as *phase plot*, as it reflects the cross-sectional crystallographic phase composition of the scanned sample lamella. Fig. 9 shows the phase plot generated for a TiN/TiB₂ hard coating on a cemented carbide substrate, that was exposed to prolonged surface oxidation prior to the csnanoxrd measurement, as presented in appended publication A.

Vertical line patterns in a phase plot represent diffraction patterns related to the same crystallographic phase, *i.e.* related to thin film depth regions of the same phase composition. Phase analysis by csnanoxrd can also map depth gradients in phase composition, co-existence of phases at a specific thin film depth, and qualitative mi-

FIGURE 9: Phase plot of a CVD TiN/TiB₂ hard coating exposed to prolonged surface oxidation, obtained by csnanoxrd, as presented in appended publication A [56]. Four distinct phases can be discerned in the presented plot of integrated intensity distribution $I(\vartheta, z)$. They coincide with individual cross-sectional substrate and coating regions, as indicated by the schematic drawing on the right-hand side. Peaks for the TiN and TiB₂ sub-layers, as well as the overlying rutile TiO₂ film, are indexed, whereas WC peaks from the cemented carbide substrate are not denoted for simplicity.



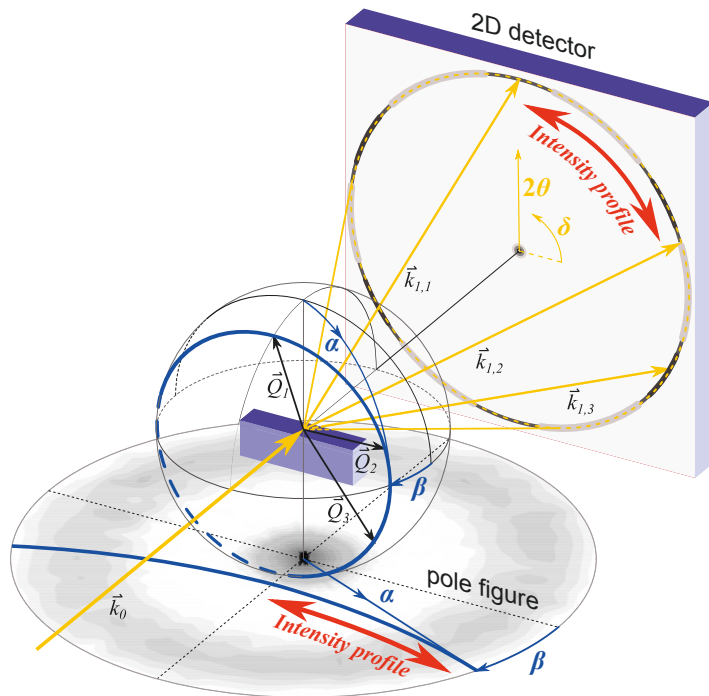


FIGURE 10: Schematic illustration depicting the relationship between the pole figure of a sample (as measured by laboratory XRD) and the Debye-Scherrer ring (as recorded on a 2D detector by CSnanoXRD). The azimuthal intensity distribution along a recorded DS ring corresponds to a section in the orientation space (indicated by the blue circular section of the depicted orientational sphere around the gauge volume), which can be stereographically projected onto a pole figure (curved blue line); courtesy of J. Todt [62].

crostructural characteristics, rendering it a comparably simple yet powerful tool to gain insight into a sample's cross-sectional make-up, given the investigated material is of polycrystalline nature and yields sufficient diffraction statistics [43, 62].

3.1.3 Crystallographic texture analysis

Crystallographic texture is defined as the statistical orientation distribution of grains within a polycrystalline material [29, 32, 63], which can be assessed by means of XRD. In laboratory XRD experiments texture measurement is based on the recording of pole figures, *i.e.* orientation dependent intensity stemming from diffraction on a specific lattice plane family. Measurements are performed by selecting the diffraction angle of a particular lattice plane and subsequently tilting and rotating the sample stage which results to an orientational scan of diffracted intensity [32, 64].

Such orientation scanning is not required in CSnanoXRD experimental configurations, because the recorded 2D diffractograms containing Debye-Scherrer rings already hold orientational information on diffracted intensity [58]. This allows for qualitatively assessing crystallographic texture, especially in thin films, where usually texture distributions exhibit fibres oriented parallel to the thin film normal. The orientational relationship between pole figures and intensity distributions recorded along Debye-Scherrer rings in CSnanoXRD is graphically illustrated in Fig. 10 [62].

3.1.4 Morphology analysis

The width of an X-ray diffraction peak, represented as full width at half maximum (FWHM) can be related to the probed material's average size of coherent diffracting domains D by *Scherrer's equation*,

$$D = \frac{K\lambda}{\text{FWHM} \cos\vartheta} , \quad (3.2)$$

where λ is the wavelength of the monochromatic X-ray radiation and parameter K is a dimensionless factor, accounting for the chosen formulation of peak breadth (FWHM or integral breadth) and crystallite shape (elongated versus globular grains) [32, 65, 66]. In the case of CSnanoXRD, peak width refers to the width of individual Debye-Scherrer rings at specific azimuthal orientations.

Peak width is furthermore influenced (widened) by the non-ideal lattice structure of real crystallites. This includes dislocations, point defects and any other local variation of lattice parameters, such as micro-strains [32]. In contrast to laboratory XRD in Bragg-Brentano geometry, where $(\vartheta-2\vartheta)$ -measurements carry information about peak widths only in the direction normal to the investigated sample surface, CSnanoXRD experiments performed in transmission geometry, and acquiring 2D diffraction patterns, allow for the evaluation of Debye-Scherrer ring FWHM at any chosen azimuthal orientation. As a consequence, in CSnanoXRD the dimensions of coherently scattering domains in the measured material can be evaluated in arbitrary sample directions, with the exception of the direction parallel to the beam, which makes it possible to discriminate morphological features of grains. Distinction of grain shape, *e.g.* needle-like, columnar, spherical can thus be achieved [43, 62, 67].

In CSnanoXRD, this involves azimuthal integration of Debye-Scherrer ring intensity within equi-spaced azimuthal regions, *i.e.* on cake-like segments of the rings. A typical approach is to perform integration on 36 individual azimuthal ring segments, extending over 10° each, resulting in a separate intensity profile $I_\vartheta(2\vartheta)$ for each segment. The integration process itself is performed in an analogous fashion as in phase analysis, using specialised algorithms. Diffraction peak width, expressed as FWHM, is usually quantified by peak fitting during the evaluation process. Practically, *pseudo-Voigt functions*, constituting linear combinations of Gauss and Lorentz functions, are used for fitting segmental intensity profiles $I_\vartheta(2\vartheta)$ to obtain direction specific FWHM [32, 62, 68].

Fig. 11a shows the evolution of FWHM of the 111 peak of a tri-layer CrN thin film studied by CSnanoXRD as a function of film thickness and azimuthal angle ϑ (a) [67]. The plot reflects (i) the gradient layered microstructure of the thin film exhibiting three zones of nucleation at distinct levels of film thickness as well as (ii) the elongated shape of coherently diffracting domains, *e.g.* grains, extending along the direction of film growth. Fig. 11b presents a plot of averaged grain size determined by Scherrer's relation as a function of thin

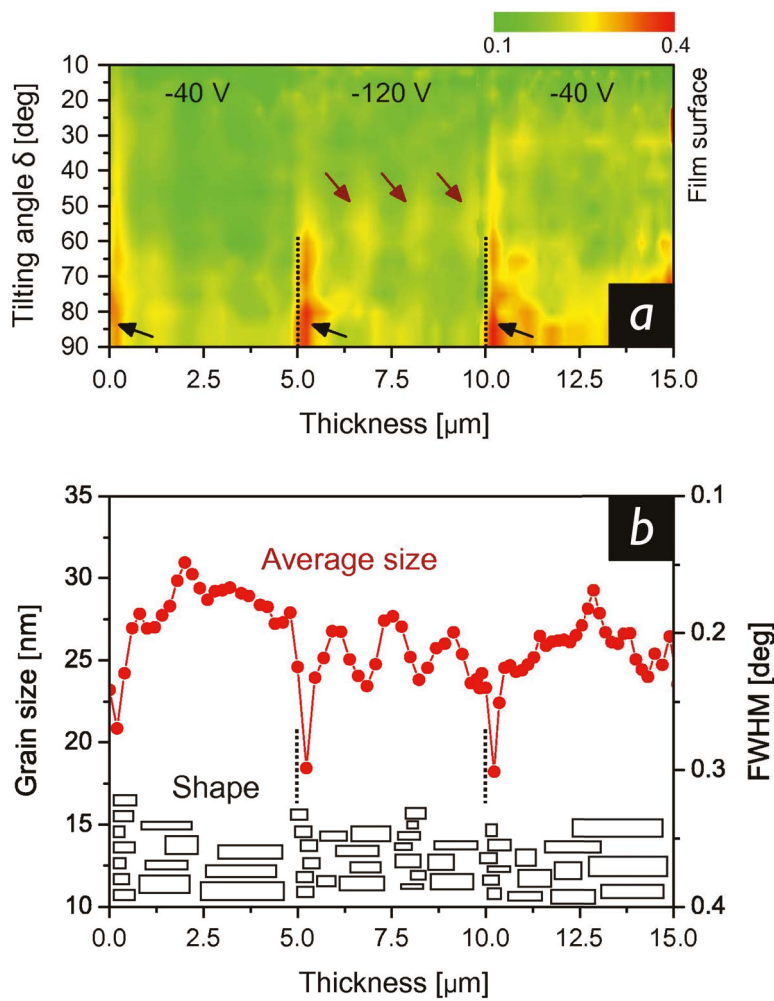


FIGURE 11: Plot of FWHM of the 111 peak of a tri-layer CrN thin film studied by csnanoxrd as a function of film thickness and azimuthal angle δ (a), and corresponding plot of averaged grain size determined by Scherrer's relation as a function of thin film thickness, also indicating grain morphology (b). (reproduced from [67])

film thickness together with a schematic depiction of film thickness dependent grain morphology.

3.1.5 Stress analysis

XRD stress analysis can retrieve internal strains and stresses prevalent in crystalline materials. Theoretical frameworks exist to analyse stress related to strains of 1st, 2nd and 3rd order [32, 69]. While 1st order strains are by far the most critical for the performance and lifetime of functional thin films, *e.g.* for tool protection or electronic applications, strains of 2nd and 3rd order play a less relevant role. For the thin film studies presented in this work only 1st order residual strains were considered and evaluated. The most basic underlying principle therefore is, that these 1st order strains extend over length scales considerably larger than individual crystallites and thus represent local and direction-dependent variations in the lattice plane spacing of

the investigated material [32].

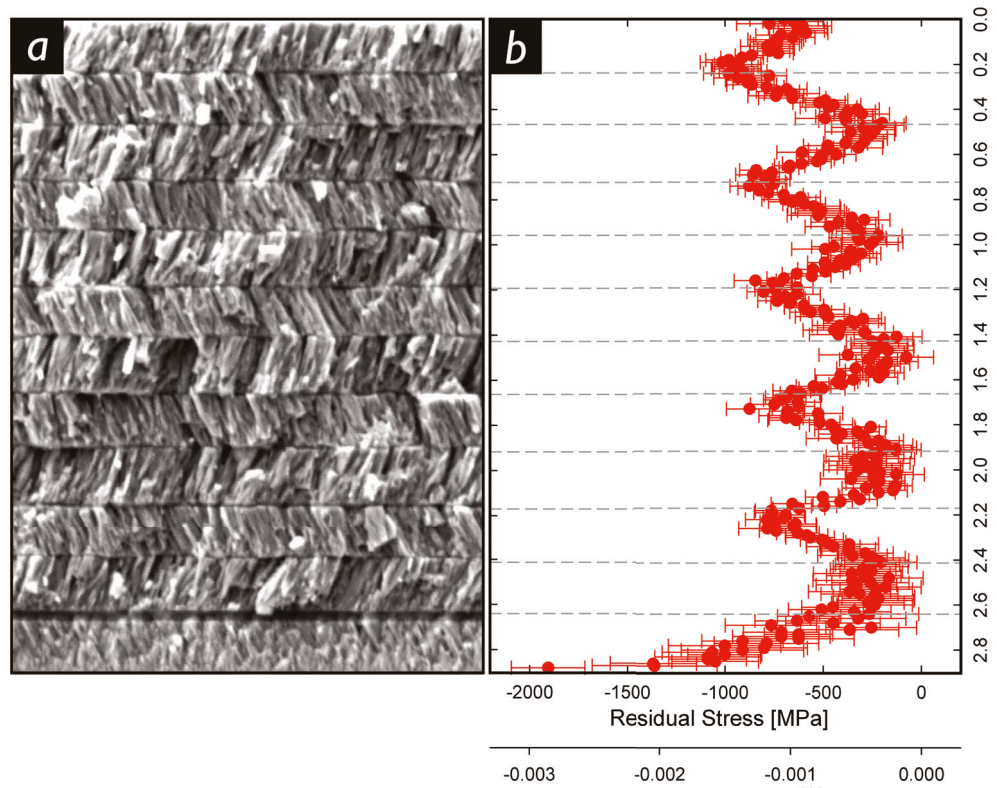
In a number of practical application cases, as in the study of thin films, where no out-of-plane stress components ($\sigma_{33} = 0$) and no shear stresses ($\sigma_{ij} = 0$) are assumed to be present, the relation between strains ε and stresses σ in an elastically isotropic material can be expressed as a simplified formulation of *Hooke's law* as formulated in terms of the relevant experimental co-ordinates ϑ and δ ,

$$\varepsilon_{hkl}(\vartheta, \delta) = \frac{d(\vartheta, \delta) - d_0}{d_0} = s_{1,hkl} 2\sigma_{22} + \frac{1}{2} s_{2,hkl} (\sigma_{22} \sin^2 \vartheta + \sigma_{22} \cos^2 \vartheta \sin^2 \delta). \quad (3.3)$$

The linear relationship between $d(\vartheta, \delta)$ and $\sin^2 \delta$ present in this equation allows for evaluation of stresses employing simple linear regression, in a very similar fashion as in the $\sin^2 \psi$ -approach extensively used in laboratory XRD [62, 69, 70]. Stress analysis from csnanoXRD 2D data is performed by segmental azimuthal integration (*cake-ing*) in order to generate segmental profiles of $I(2\vartheta)$ for a number of azimuthal orientations, and subsequent peak fitting in an analogous manner as in csnanoXRD morphology analysis.

Fig. 8a & b shows the in-plane residual stress depth gradient $\sigma(z)$ of a multilayer TiN-SiO_x coating of $\sim 2.9 \mu\text{m}$ thickness, together with a corresponding cross-sectional SEM micrograph [44]. The recorded profile exhibits distinct oscillatory variations of residual stress, related to varying characteristics of the TiN sub-layers, which were deposited to feature zig-zag like columnar grain morphology. The measured profile exemplifies the strength of csnanoXRD in retrieving complex cross-sectional stress and strain gradients in thin films.

FIGURE 12: Cross-sectional SEM micrograph (a) and corresponding residual stress depth profile (b) of a multilayer TiN-SiO_x (adapted from [44]). The oscillatory stress profile shows decreasing and increasing compressive residual stress values between individual TiN sub-layers, reflecting their different zig-zag like, right- and left-leaning, columnar grain structure which is apparent as a herringbone pattern in (b).



More detailed information on CSnanoXRD stress analysis can be found in Refs. [33, 51]

3.2 Micromechanical testing

Despite the fact that thin films are usually employed for their specific functional properties, structural integrity is as crucial as in bulk materials. A large number of application cases requires distinct mechanical characteristics for achieving optimal operational performance and lifetimes. This is particularly apparent in the case of hard protective coatings which have to sustain severe cyclic mechanical and thermal loads *e.g.* during milling operations. Hence, assessing mechanical properties such as hardness, Young's modulus or fracture toughness is of vital importance for coating development. Specialised experimental methods based on micro-mechanics have been devised for measuring various mechanical properties of thin films, all of them accounting for the small physical dimensions of the investigated structures. The high spatial resolution required for measuring these quantities within a thin film is based on miniaturisation of test specimens and/or probe interaction with highly localised regions. Experimental approaches include micro or nanoindentation, micro-cantilever bending experiments and a variety of miniaturised testing configurations based on uni-axial tension and compression [71–73]. The historical development of these techniques is closely linked to improvements made in instrumented measurement and the availability of electron microscopy and focussed ion beam (FIB) systems. Subsections 3.2.1 and 3.2.2 provide a short overview of nanoindentation and micro-cantilever bending experiments, respectively.

3.2.1 Nanoindentation

Nanoindentation is based on creating imprints by inducing plastification in highly localised material regions of the investigated sample. This is achieved by loading and subsequent unloading of the sample with a sharp pointed indenter tip while continuously recording applied force (load) and penetration depth (displacement). This renders nanoindentation an instrumented measurement method.

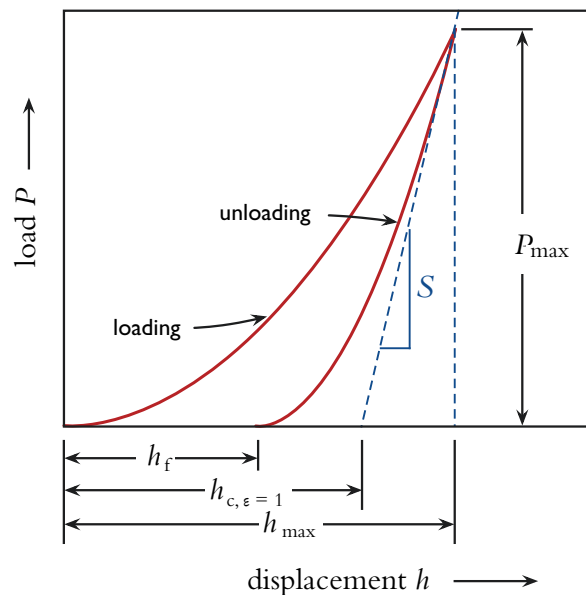
Indenter tips require very high stiffness and are in most cases made of diamond. Several commonly used geometrical indenter shapes co-exist, with three-sided so-called *Berkovich* (with a half angle of 65.03°) [74] and *cube-corner* tips featuring among the practically most relevant.

Nanoindentation measurements may be performed on thin film surfaces or specially prepared (*e.g.* by FIB milling) thin film cross-sections [49, 75] or inclined wedge-shaped sections [76–78], in order to obtain depth gradients of mechanical properties. Cross-sectional na-

noindentation based hardness measurements of NCD and PCD CVD diamond are presented in appended publication B, where a *Hysitron TI950 Triboindenter* system was used. Depending on the hardness of the investigated sample and the employed experimental configurations, applied indentation loads fall within the range of micro- to milli-Newtons, translating into effective penetration depths of ~ 50 – 1000 nm. A widely used and accepted theoretical framework for the interpretation of nanoindentation load-displacement data was introduced by W.C. Oliver and G.M. Pharr in 1992 [79], allowing for the retrieval of hardness H , contact stiffness S and reduced elastic modulus E_r . In the main, nanoindentation puts fewer demands on sample preparation, when compared to micro-mechanical bending, tension or compression experiments, where elaborate sample specimen fabrication is required, usually requiring access to FIB workstations. Though the actual indentation process is to be considered profoundly complex, potentially involving (i) creep, (ii) material pile-ups, (iii) sink-ins, and other phenomena associated with plastic and visco-elastic deformation, as well as (iv) crack formation, nanoindentation has evolved into a much-used method in scientific and applied research in the last two decades [80–83]. The inherent dependence of measured quantities H and E_r on experiment-specific measurement conditions is in a large number of cases accepted in virtue of the simpler experimental procedure, when compared to testing of micro-size bending, tensile or compressive specimens. Nanoindenters can be used for in-situ experiments in the SEM or TEM or equipped with heating modules to perform high-temperature nanoindentation [81].

In the following, the evaluation of H and E_r based on [79] is outlined in brief. A corresponding schematic drawing of an indentation process is presented in Fig. 13, where red lines show load-penetration curves for loading and unloading, respectively.

FIGURE 13: Schematic drawing of the load-penetration curves of loading and unloading phases in instrumented nanoindentation (adapted from [79]). Loading is performed up to maximum load P_{\max} where the indenter tip reaches maximum penetration depth h_{\max} . The slope of the unloading curve is steeper than in loading, resulting in the formation of a permanent indent of depth h_f in the probed material.



Hardness H is defined as

$$H = \frac{P_{\max}}{A_c}, \quad (3.4)$$

with P_{\max} being the maximum load applied, and A_c representing the projected contact area of the created indent. While P_{\max} is directly accessible from the recorded load-penetration data, A_c is usually hard to obtain by direct observation, since imaging of nano-scale indent craters would be an intricate and time-consuming undertaking, and measurements be prone to error. In lieu, a so-called *area function*, dependent on the indenter tip geometry is formulated, relating contact depth h_c to projected contact area A_c . An analytic formulation exists for different tip geometries in the form of a power law,

$$A_c = \alpha h_c^m, \quad (3.5)$$

with shape-specific exponents m and dimensionless parameter α [84]. For practical considerations, however, A_c is in most cases adjusted to reflect the imperfect, *de facto* tip geometry by fitting coefficients C_n of a polynomial expansion,

$$A(h_c) = \sum_{n=1}^8 C_n h_c^{2(\frac{1}{2})^n}, \quad (3.6)$$

to multiple calibration indents on a standard material of known hardness and elastic modulus, *e.g.* fused silica [79].

Contact depth h_c can be determined by equation

$$h_c = h_{\max} - \varepsilon \frac{P_{\max}}{S}, \quad (3.7)$$

i.e. by linear extrapolation of the initial slope of the unloading phase load-penetration curve, so-called *contact stiffness* S (for the $\varepsilon = 1$), *cf.* Fig 13. Parameter ε models the elastic response of the loaded material outside the contact area at applied maximum load P_{\max} . It varies in the range of 0.72 (pyramid shaped and conical tip geometry) to 1. A value of $\varepsilon = 0.75$, corresponding to a paraboloidal tip cross-section may be chosen to account for the non-ideal shape of a real indenter tip. Contact stiffness S can be obtained by approximating a power law function to the recorded unloading phase load-penetration curve and subsequent calculation of its derivative at point P_{\max} .

Reduced elastic modulus E_r can then be expressed as

$$E_r = \frac{\pi^{\frac{1}{2}} S}{2 A_r^{\frac{1}{2}}}. \quad (3.8)$$

A tested material's elastic modulus E may only be calculated based

on prior knowledge about the indenter tip's elastic characteristics (elastic modulus E_t , Poisson ratio ν_t), as well as about the Poisson ratio ν of the material itself, according to

$$\frac{1}{E_r} = \frac{1-\nu}{E} + \frac{1-\nu_t}{E_t} , \quad (3.9)$$

In nanoindentation experiments the compliance of the indentation apparatus, C_f , can considerably influence measured penetration depths and thus distort results. Various procedures were devised for determining machine compliance C_f in conjunction with the area function A_c . In their contribution, Oliver and Pharr [79] propose performing a series of indents of varying depth while assuming independence of the indented material's elastic modulus of indentation depth. An iterative approach can then be taken to determine C_f and the coefficients C_n of the polynomial approximation to the area function $A(h_c)$. Practically, machine compliance calibration procedures based on standard materials possessing precisely known hardness, *e.g.* fused silica, have gained increasing importance [85, 86]. Various experimental guidelines exist for the minimal spacing between individual indents on a surface or cross-section, as well as the maximum indentation depth when indenting on thin films.

3.2.2 Micro-cantilever bending

Micro-cantilever bending is a micro-mechanical materials testing technique which allows to assess highly local mechanical properties of the investigated sample material. The method can be used to obtain Young's modulus, fracture stress as well as fracture toughness, parameters considered to be of critical importance in many thin film applications. In contrast to hardness and reduced elastic modulus determined by nanoindentation, which are complex and experiment-specific quantities, the aforementioned parameters reflect fundamental material properties in a physical sense. The basic experimental principle is to use a nanoindenter to load a free-standing cantilever beam, consisting of the material to be investigated, up to the load of failure, while continuously recording load F and displacement d . Experiments may be performed with self-contained nanoindenter systems or in in-situ configuration in an SEM. A growing number of research contributions have demonstrated the potential of micro-cantilever bending as a valuable method for directly characterising mechanical properties of thin films [76, 87–92].

Fig. 14a shows an SEM micrograph of a micro-cantilever fabricated from the PCD top layer of a CVD diamond thin film, as used in bending experiments presented in appended publication B. The specimen features dimensions of $(w \times B \times l) \sim (1.4 \times 1.4 \times 12) \mu\text{m}^3$.

In Fig. 14b a schematic drawing of a micro-cantilever is presented, indicating specimen geometry, where bending length l refers to the distance between the point of applied load and the resulting fracture

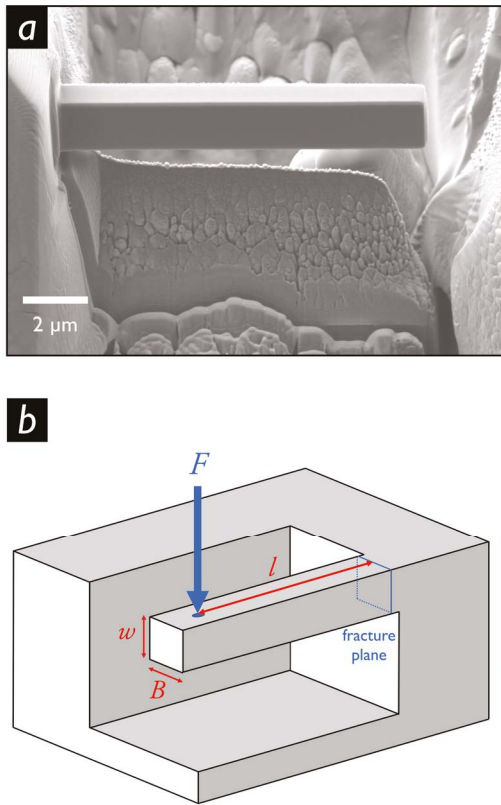


FIGURE 14: SEM micrograph of an un-notched micro-cantilever, which was used for in-situ bending experiments to determine values of Young's modulus and fracture stress for the cross-sectional study of a CVD diamond thin film (appended publication B). Cantilever length l , width B and thickness w are shown in a schematic drawing of a micro-cantilever in (b), where F denotes the point of loading. Failure occurs at the fracture plane, close to the root of the bending beam.

plane, while B and w represent the cantilever width and thickness, respectively.

In-situ micro-cantilever bending in an SEM was used to measure Young's modulus and fracture stress in the cross-sectional thin film studies appended in publications A and B, [56, 57].

The theoretical framework for the evaluation of micro-cantilever bending experiments presented henceforth, rests on Euler-Bernoulli beam theory and linear elastic mechanics of fracture. This approach is based on the assumption of negligible plastic deformation in the probed material, which is qualified in the case of hard and brittle thin films [93–95]. The evaluation methodology allows to measure Young's modulus E , fracture stress σ_s and fracture toughness K_{IC} . While evaluation of E and σ_s relies on experiments with unaltered, as-prepared cantilevers, determining K_{IC} requires testing of cantilevers with precisely defined notches placed close to their roots.

Euler-Bernoulli theory relates Young's modulus E of a free-standing beam to the dominant elastic response recorded in cantilever loading according to

$$E = \frac{\partial F}{\partial d} \frac{4}{B} \left(\frac{l}{w} \right)^3 = \frac{4F_{\max}}{\delta B} \left(\frac{l}{w} \right)^3, \quad (3.10)$$

where the slope of the load-displacement curve can be expressed as the quotient of maximum applied load F_{\max} and maximum displacement δ , assuming ideally elastic behaviour.

Fracture stress σ_s can be calculated as

$$\sigma_s = 6 \frac{F_{\max} l}{B w^2} \quad (3.11)$$

Based on experiments with notched micro-cantilevers, fracture toughness can be evaluated from the relation

$$K_{IC} = \sigma(\pi a)^{\frac{1}{2}} Y, \quad (3.12)$$

where σ denotes the applied stress on the notched cantilever specimen at the point of fracture, while a represents the depth of the introduced notch. Parameter Y is a factor representing the experimental geometry, dependent on a and w . Evaluation of experiments presented in appended publications A and B was based on a specific formulation of Y published in Ref. [96].

Fabrication of micro-cantilevers is carried out by means of FIB milling, which allows to produce beams with sub-micrometre dimensions. Typical cantilever geometries feature total specimen lengths of $\sim 10 \mu\text{m}$ and cross-sections ($w \times B$) of $\sim (2 \times 2) \mu\text{m}^2$. Used FIB milling currents range from $\sim 20 \text{nA}$ for coarse pre-cuts down to $\sim 50 \text{pA}$ for final polishing. Notches for the measurement of fracture toughness need to be precise and well defined. Hence, cantilever notching is performed at even lower ion beam currents. Prior to FIB milling, sample cross-sections may be treated by mechanical polishing or ion milling to avoid rounded thin film top edges. The use of high FIB milling currents can effect contamination of sample material with Ga^+ ions, and thus damage cantilever specimens and potentially distort measurement results. Consequently, final milling operations are carried out at low currents.

Owing to the fact that the governing fracture mechanism in hard and brittle thin films, usually a set containing several micro-cantilever specimens has to be tested in order to obtain reliable, averaged, values of mechanical properties.

In the actual bending experiments, the cantilevers are loaded by a nanoindenter in a controlled way with a sharp diamond tip close to their free-standing ends. Performing the experiments in displacement-controlled mode, at low, constant loading rates of $\sim 20 \text{nm/s}$ ensures quasi-static loading conditions [95]. For the experiments presented in publications A and B, a diamond tip featuring a sphero-conical shape with a radius of curvature of $\sim 700 \text{nm}$ was mounted to a *Hysitron Pi-85 PicoIndenter* system for cantilever loading. The indenter featured a piezo-actuated sample stage for precise sample positioning. Experiments were conducted in in-situ configuration in a *Zeiss LEO 982* type SEM, allowing for high resolution and real-time imaging as well as precise determination of bending lengths of un-notched cantilevers.

Post-mortem SEM imaging of fracture surfaces of tested micro-cantilevers can give valuable insight into the nature of the fracture events. Commonly, irregularities in recorded load-displacement curves can be correlated to atypical fracture surfaces which may be due to (i) unwanted material inhomogeneities, *e.g.* incorporation of macro-defects, delamination phenomena or pre-existing cracks or (ii) deliberately engineered thin film architectures designed to maximise crack-path lengths in order to increase fracture toughness [91, 92]. Data from micro-cantilevers failed by unwanted effects and thus constituting experimental outliers may subsequently be excluded from further evaluation.

4 Conclusions and outlook

The research contributions presented in this work (i) are concerned with applying relatively novel, advanced micro- and nano-scale experimental techniques for the characterisation of hard thin films, (ii) focus on resolving thin film structure and property depth gradients, *i.e.* cross-sectional thin film properties and (iii) make use of csnanoxrd as a key experimental method.

Two cross-sectional thin film characterisation studies are presented, revealing complex correlations between depth gradients of (i) deposition conditions, (ii) microstructure, (iii) residual stress state and (iv) mechanical properties. A third study was concerned with the strain and stress evolution and plastification phenomena in near-coating cemented carbide substrate regions. The three contributions are summarised below:

- A A cross-sectional study of a CVD TiN/TiB₂ protective hard coating, which was exposed to prolonged surface oxidation, provided detailed insight into the depth-dependent oxidation-induced changes within the nanocrystalline TiB₂ sublayer. The study was primarily based on nano-analytical techniques, in particular csnanoxrd, featuring a 30 nm synchrotron X-ray beam. It proved that the TiB₂ sublayer protected underlying coating regions and the WC/Co substrate from structural and mechanical degradation. The experimental approach revealed (i) a stratified grain morphology of the rutile TiO₂ oxide layer, (ii) the formation of a transition zone where intact TiB₂ and rutile phase TiO₂ co-existed, separated by a clear oxidation front from unaffected TiB₂ material. In addition, (iii) in-situ micro-cantilever bending found a reduction in elastic modulus of the TiB₂ region underneath the oxide film of ~25% relative to its untreated counterpart. csnanoxrd furthermore revealed (iv) pronounced relaxation of residual stress in the TiB₂ phase in the oxidised sample, coinciding with the discovered transition zone.

- B A nano-analytics based cross-sectional study of a CVD diamond thin film, which consisted of a NCD bottom layer and a coarse-grained PCD top layer, represented the first application of csnanoxrd for the investigation of diamond thin films. Cross-sectional mechanical properties were measured by in-situ micro-cantilever bending and nanoindentation. The cross-sectional experimental data (i) revealed complex correlations between thin film mechanical properties, texture, crystallite size, residual stress and deposition conditions. In particular, (ii) both the NCD and PCD sublayers indicated the presence of nucleation regions with distinct gradual microstructures, which were assessed by csnanoxrd.

- C A sophisticated synchrotron XRD set-up based on in-situ laser pulsing was used to study near-coating substrate regions of WC-Co inserts when subjected to local thermal shocks. These inserts were coated with CVD TiCN/ α -Al₂O₃ films. The experiment was able to measure the temperature and time-dependent evolution of strains and stresses in the W phase under rapid cyclic laser pulsing at millisecond time resolution. This provided detailed insight into (i) the complex stress build-up and relaxation during single and multiple thermal shocks, (ii) the associated WC-Co composite plastification mechanism as well as (iii) anisotropic microstructural processes accompanying reversible microstructural transition mechanisms.

In particular, the presented contributions (i) showcase the strength and efficacy of CSnanoXRD as a high-resolution nano-scale method for the cross-sectional investigation of crystalline thin films and hard coatings, (ii) underline the great potential of combined micro- and nano-analytic approaches in thin film characterisation, and (iii) demonstrate the capability of advanced in-situ synchrotron XRD set-ups for studying complex phenomena in crystalline materials at high time resolution.

In the case of CSnanoXRD, one aspect of future methodological and experimental development will be further improvement of the technique in terms of spatial and temporal resolution. Present and future upgrades of synchrotron light sources and associated enhancements in X-ray beam brilliance, together with expected improvements in X-ray focussing optics, will gradually minimise achievable beam dimensions and decrease experimental exposure times. Great potential also lies in the further development of advanced in-situ set-ups for synchrotron XRD and CSnanoXRD.

References

- [1] M. Ohring, *Materials science of thin films: deposition and structure*, 2nd ed., Academic Press, New York, 2001.
- [2] J.E. Greene, Review Article: *Tracing the recorded history of thin-film sputter deposition: From the 1800s to 2017*, *J. Vac. Sci. Technol. A*. 35 (2017) 05C204.
- [3] S. Zhang, *Handbook of nanostructured thin films and coatings*, CRC Press, 2010.
- [4] A. Cavaleiro, J.T. de Hosson, A. Cavaleiro, J.T.M. de Hosson, *Nanostructured Coatings*, Springer, New York, 2007.
- [5] O. Stenzel, *Optical Coatings*, Springer, Berlin, Heidelberg, 2014.
- [6] H.J. Griesser, *Thin Film Coatings for Biomaterials and Biomedical Applications*, Elsevier, 2016.
- [7] U. Schleinkofer, C. Czettel, C. Michotte, *Coating Applications for Cutting Tools*, *Comprehensive Hard Materials* (2014) 453–469.
- [8] K. Bobzin, *High-performance coatings for cutting tools*, *CIRP J. Manuf. Sci. Technol.* 18 (2017) 1–9.
- [9] J.A. Venables, *Introduction to Surface and Thin Film Processes*, Cambridge University Press, 2000.
- [10] C. Mitterer, *PVD and CVD Hard Coatings*, *Comprehensive Hard Materials* (2014) 449–467
- [11] G. List, G. Sutter, A. Bouthiche, *Cutting temperature prediction in high speed machining by numerical modelling of chip formation and its dependence with crater wear*, *Int. J. Mach. Tools. Manuf.* 54–55 (2012) 1–9
- [12] J. Todt, R. Pitonak, A. Köpf, R. Weißenbacher, B. Sartory, M. Burghammer, R. Daniel, T. Schöberl, J. Keckes, *Superior oxidation resistance, mechanical properties and residual stresses of an Al-rich nanolamellar $Ti_{0.05}Al_{0.95}N$ coating prepared by CVD*, *Surf. Coat. Tech.* 258 (2014) 1119–1127.
- [13] M. Meindlhumer, J. Zalesak, R. Pitonak, J. Todt, B. Sartory, M. Burghammer, A. Stark, N. Schell, R. Daniel, J.F. Keckes, M. Lessiak, A. Köpf, R. Weißenbacher, J. Keckes, *Biomimetic hard and tough nanoceramic Ti-Al-N film with self-assembled six-level hierarchy*, *Nanoscale* 11 (2019) 7986–7995.

- [14] C. Czettel, J. Thurner, U. Schleinkofer, *Knowledge based coating design of CVD TiN-TiBN-TiB₂ architecture*, Int. J. Refract. Metals Hard Mater. 71 (2018) 330–334.
- [15] R.F. Bunshah, *Deposition Technologies for Films and Coatings*, Noyes Publications, Ney Jersey, 1982.
- [16] F.-W. Bach, K. Möhwald, A. Laarmann, T. Wenz, *Moderne Beschichtungsverfahren*, Wiley & Sons, 2006.
- [17] H.O. Pierson, *Handbook of Chemical Vapor Deposition*, William Andrew, 2012.
- [18] A. Anders, *Cathodic Arcs: From Fractal Spots to Energetic Condensation*, Springer, Dordrecht, 2009.
- [19] R. A. Powell, S. M. Rossnagel, *PVD for microelectronics: sputter deposition applied to semiconductor manufacturing*, Thin Films 26 (1999).
- [20] I. Safi, *Recent aspects concerning DC reactive magnetron sputtering of thin films: A review*, Surf. Coat. Tech. 127 (2000) 203–218.
- [21] C. Czettel, *Design of CVD Coatings for Cutting Tools*, doctoral thesis, Montanuniversität Leoben, 2013.
- [22] M. Tkadletz, *Advanced characterization techniques for the knowledge-based design of hard coatings*, doctoral thesis, Montanuniversität Leoben, 2015.
- [23] H. Lüth, *Solid Surfaces, Interfaces and Thin Films*, Springer, 2014.
- [24] B.A. Movchan, A.V. Demchishin, *Structure and Properties of Thick Condensates of Nickel, Titanium, Tungsten, Aluminum Oxides, and Zirconium Dioxide in Vacuum*, Fiz. Metal. Metalloved. 28 (1969) 653–600.
- [25] J.A. Thornton, *Influence of apparatus geometry and deposition conditions on the structure and topography of thick sputtered coatings*, J. Vac. Sci. Technol. A. 11 (1974) 666–670.
- [26] R. Messier, A.P. Giri, R.A. Roy, *Revised Structure Zone Model for Thin Film Physical Structure*, J. Vac. Sci. Technol. A. 2 (1984) 500.
- [27] A. Anders, *A structure zone diagram including plasma-based deposition and ion etching*, Thin Solid Films 518 (2010) 4087–4090.

- [28] M. Tkadletz, J. Keckes, N. Schalk, I. Krajinovic, M. Burghammer, C. Czettel, C. Mitterer, *Residual stress gradients in α -Al₂O₃ hard coatings determined by pencil-beam X-ray nanodiffraction: The influence of blasting media*, SURF. COAT. TECH. 262 (2015) 134–140.
- [29] M. de Graef, M. E. McHenry, *Structure of Materials*, Cambridge University Press, 2012.
- [30] A. Authier, *Early days of X-ray crystallography*, Oxford University Press, Oxford, UK, 2013.
- [31] J. M. Thomas, *The birth of X-ray crystallography*, Nature 491 (2012) 186–187.
- [32] L. Spiess, G. Teichert, R. Schwarzer, H. Behnken, C. Genzel, *Moderne Röntgenbeugung*, 3. überarbeitete Auflage, Springer, Wiesbaden, 2019.
- [33] M. Stefenelli, J. Todt, A. Riedl, W. Ecker, T. Müller, R. Daniel, M. Burghammer, J. Keckes, *X-ray analysis of residual stress gradients in TiN coatings by a Laplace space approach and cross-sectional nanodiffraction: a critical comparison*, J. Appl. Crystallogr. 46 (2013) 1378–1385.
- [34] G. Abadias, E. Chason, J. Keckes, M. Sebastiani, G.B. Thompson, E. Barthel, G.L. Doll, C.E. Murray, C.H. Stoessel, L. Martinu, *Stress in thin films and coatings: Current status, challenges, and prospects*, J. Vac. Sci. Technol. A. 36 (2018) 020801.
- [35] C. Genzel, *X-ray stress gradient analysis in thin layers - Problems and attempts at their solution*, Physica Status Solidi A Appl. Res. 159 (1997) 283–296.
- [36] C. Genzel, *Formalism for the evaluation of strongly non-linear surface stress fields by X-ray diffraction performed in the scattering vector mode*, Physica Status Solidi A Appl. Res. 146 (1994) 629–637.
- [37] M. Klaus, C. Genzel, H. Holzschuh, *Residual stress depth profiling in complex hard coating systems by X-ray diffraction*, Thin Solid Films 517 (2008) 1172–1176.
- [38] S. J. Leake, G.A. Chahine, H. Djazouli, T. Zhou, C. Richter, J. Hilhorst, L. Petit, M.I. Richard, C. Morawe, R. Barrett, L. Zhang, R.A. Homs-Regajo, V. Favre-Nicolin, P. Boesecke, T.U. Schüllli, *The nanodiffraction beamline ID01/ESRF: A microscope for imaging strain and structure*, J. Synchrotron Radiat. 26 (2019) 571–584.

- [39] C. Riekel, M. Burghammer, R. Davies, R. Gebhardt, D. Popov, *Fundamentals of soft condensed matter scattering and diffraction with microfocus techniques*, Lect. Notes Phys. 776 (2009) 91–104.
- [40] P. Staron, A. Schreyer, H. Clemens, S. Mayer, *Neutrons and Synchrotron Radiation in Engineering Materials Science*, John Wiley & Sons, Weinheim, 2017.
- [41] J. Liu, P. Staron, S. Riekehr, A. Stark, N. Schell, N. Huber, A. Schreyer, M. Müller, N. Kashaev, *In situ study of phase transformations during laser-beam welding of a TiAl alloy for grain refinement and mechanical property optimization*, Intermetallics. 62 (2015) 27–35.
- [42] D. P. Gruber, D. Kiefer, R. Rössler, F. Beckmann, M. Tkadletz, T. Klünsner, C. Czettel, J. Keckes, J. Gibmeier, *20 Hz synchrotron X-ray diffraction analysis in laser-pulsed WC-Co hard metal reveals oscillatory stresses and reversible composite plastification*, Int. J. Refract. Metals Hard Mater. 82 (2019) 121–128.
- [43] J. Keckes, M. Bartosik, R. Daniel, C. Mitterer, G. Maier, W. Ecker, J. Vila-Comamala, C. David, S. Schoeder, M. Burghammer, *X-ray nanodiffraction reveals strain and microstructure evolution in nanocrystalline thin films*, Scr. Mater. 67 (2012) 748–751.
- [44] J. Keckes, R. Daniel, J. Todt, J. Zalesak, B. Sartory, S. Braun, J. Gluch, M. Rosenthal, M. Burghammer, C. Mitterer, S. Niese, A. Kubec, *30 nm X-ray focusing correlates oscillatory stress, texture and structural defect gradients across multilayered TiN-SiO_x thin film*, Acta Mater. 144 (2018) 862–873.
- [45] A. Kubec, K. Melzer, J. Gluch, S. Niese, S. Braun, J. Patommel, M. Burghammer, A. Leson, *Point focusing with flat and wedged crossed multilayer Laue lenses*, J. Synchrotron Radiat. 24 (2017) 413–421.
- [46] S. Niese, P. Krüger, A. Kubec, R. Laas, P. Gawlitza, K. Melzer, S. Braun, E. Zschech, *Fabrication of customizable wedged multilayer Laue lenses by adding a stress layer*, Thin Solid Films, 571 (2) (2014) 321–324.
- [47] A. Culiuc, C. Dielmann, G. Fayad, H. Hesse, E. Hife, C. Kolerus, A. Kyobe, V. Lledo, A. Luca, M. Mansilla, F. Ricka, C. Saborowski, Y. Sun-wang, K. Svirydzenka, *ESRF Upgrade programme phase II*, 2015.

- [48] M. Bartosik, R. Daniel, C. Mitterer, I. Matko, M. Burghammer, P.H. Mayrhofer, J. Keckes, *Cross-sectional X-ray nanobeam diffraction analysis of a compositionally graded CrN_x thin film*, Thin Solid Films 542 (2013) 1–4.
- [49] J. Zalesak, M. Bartosik, R. Daniel, C. Mitterer, C. Krywka, D. Kiener, P. H. Mayrhofer, J. Keckes, *Cross-sectional structure-property relationship in a graded nanocrystalline Ti_{1-x}Al_xN thin film*, Acta Mater. 102 (2016) 212–219.
- [50] N. Jäger, S. Klima, H. Hruby, J. Julin, M. Burghammer, J. F. Keckes, C. Mitterer, R. Daniel, *Evolution of structure and residual stress of a fcc/hex-AlCrN multi-layered system upon thermal loading revealed by cross-sectional X-ray nano-diffraction*, Acta Mater. 162 (2019) 55–66.
- [51] M. Stefenelli, R. Daniel, W. Ecker, D. Kiener, J. Todt, A. Zeilinger, C. Mitterer, M. Burghammer, J. Keckes, *X-ray nanodiffraction reveals stress distribution across an indented multilayered CrN–Cr thin film*, Acta Mater. 85 (2015) 24–31.
- [52] J. Todt, C. Krywka, Z.L. Zhang, P.H. Mayrhofer, J. Keckes, M. Bartosik, *Indentation response of a superlattice thin film revealed by in-situ scanning X-ray nanodiffraction*, Acta Mater. 195 (2020) 425–432.
- [53] A. Zeilinger, J. Todt, C. Krywka, M. Müller, W. Ecker, B. Sartory, M. Meindlhumer, M. Stefenelli, R. Daniel, C. Mitterer, J. Keckes, *In-situ Observation of Cross-Sectional Microstructural Changes and Stress Distributions in Fracturing TiN Thin Film during Nanoindentation*, Sci. Rep. 6 (2016) 1–14.
- [54] M. Meindlhumer, L.R. Brandt, J. Zalesak, M. Rosenthal, H. Hruby, J. Kopecek, E. Salvati, C. Mitterer, R. Daniel, J. Todt, J. Keckes, A.M. Korsunsky, *Evolution of stress fields during crack growth and arrest in a brittle-ductile CrN-Cr clamped-cantilever analysed by X-ray nanodiffraction and modelling*, Mater. Des. 198 (2020) 109365.
- [55] M. Meindlhumer, N. Jäger, S. Spor, M. Rosenthal, J.F. Keckes, H. Hruby, C. Mitterer, R. Daniel, J. Keckes, J. Todt, *Nanoscale residual stress and microstructure gradients across the cutting edge area of a TiN coating on WC-Co*, Scripta Mater. 182 (2020) 11–15.

- [56] D. P. Gruber, J. Zalesak, J. Todt, M. Tkadletz, B. Sartory, J.P. Suuronen, T. Ziegelwanger, C. Czettel, C. Mitterer, J. Keckes, *Surface oxidation of nanocrystalline CVD TiB₂ hard coatings revealed by cross-sectional nano-analytics and in-situ micro-cantilever testing*, Surf. Coat. Tech. 399 (2020) 126181.
- [57] D. P. Gruber, J. Todt, N. Wöhr, J. Zalesak, M. Tkadletz, A. Kubec, S. Niese, M. Burghammer, M. Rosenthal, H. Sternschulte, M.J. Pfeifenberger, B. Sartory, J. Keckes, *Gradients of microstructure, stresses and mechanical properties in a multi-layered diamond thin film revealed by correlative cross-sectional nano-analytics*, Carbon 144 (2019) 666–674.
- [58] B. B. He, *Introduction to two-dimensional X-ray diffraction*, Powder Diffr. 18 (2003) 71–85.
- [59] A. P. Hammersley, S. O. Svensson, A. Thompson, *Calibration and correction of spatial distortions in 2D detector systems*, Nucl. Instrum. Methods. Phys. Res. A 346 (1994) 312–321.
- [60] A. P. Hammersley, S. O. Svensson, A. Thompson, H. Graafsma, Å. Kvik, J.P. Moy, *Calibration and correction of distortions in two-dimensional detector systems*, Rev. Sci. Instrum. 66 (1995) 2729–2733.
- [61] J. Kieffer, D. Karkoulis, *PyFAI, a versatile library for azimuthal regrouping*, J. Phys. Conf. Ser. 425 (2013) 202012.
- [62] J. Todt, *Nanoscale Investigations of Performance-critical Regions in Non-homogeneous Metallic and Ceramic Thin Films*, doctoral thesis, Montanuniversität Leoben, 2016.
- [63] M. M. Woolfson, *An Introduction to X-ray Crystallography*, Cambridge University Press, 1997.
- [64] Y. Waseda, E. Matsubara, K. Shinoda, *X-Ray Diffraction Crystallography*, Springer, Berlin, Heidelberg, 2011.
- [65] L.H. Schwartz, J.B. Cohen, *Diffraction from Materials*, Springer, Berlin, Heidelberg 2013.
- [66] Warren, *X-ray diffraction*, Dover Publications, Inc., New York, 1990.
- [67] R. Daniel, J. Keckes, I. Matko, M. Burghammer, C. Mitterer, *Origins of microstructure and stress gradients in nanocrystalline thin films: The role of growth parameters and self-organization*, Acta Mater. 61 (2013) 6255–6266.

- [68] M. Birkholz, *Thin Film Analysis by X-Ray Scattering*, 1st ed., Wiley & Sons, 2006.
- [69] I. C. Noyan, J. B. Cohen, *Residual Stress*, Springer, 2013.
- [70] V. Hauk, H. Behnken, *Structural and residual stress analysis by nondestructive methods: evaluation, application, assessment*, Elsevier, 1997.
- [71] D. Kiener, C. Motz, G. Dehm, *Micro-compression testing: A critical discussion of experimental constraints*, *Mat. Sci. Eng. A* 505 (2009) 79–87.
- [72] G. Dehm, B.N. Jaya, R. Raghavan, C. Kirchlechner, *Overview on micro- and nanomechanical testing: New insights in interface plasticity and fracture at small length scales*, *Acta Mater.* 142 (2018) 248–282.
- [73] R. Fritz, D. Kiener, *Development and application of a heated in-situ SEM micro-testing device*, *Measurement*, *Measurement* (Lond) 110 (2017) 356–366.
- [74] E.S. Berkovich, *Three faceted diamond pyramid for micro-hardness testing*, *Ind. Diamond Rev.* 11 (1951) 129–132.
- [75] J. Zalesak, J. Todt, R. Pitonak, A. Köpf, R. Weißenbacher, B. Sartory, M. Burghammer, R. Daniel, J. Keckes, *Combinatorial refinement of thin-film microstructure, properties and process conditions: iterative nanoscale search for self-assembled TiAlN nanolamellae*, *J. Appl. Crystallogr.* 49 (2016) 2217–2225.
- [76] A. Zeilinger, R. Daniel, T. Schöberl, M. Stefenelli, B. Sartory, J. Keckes, C. Mitterer, *Resolving depth evolution of microstructure and hardness in sputtered CrN film*, *Thin Solid Films* 581 (2015) 75–79.
- [77] C. Ziebert, C. Bauer, M. Stüber, S. Ulrich, H. Holleck, *Characterisation of the interface region in stepwise bias-graded layers of DLC films by a high-resolution depth profiling method*, *Thin Solid Films* 482 (2005) 63–68.
- [78] C. Ziebert, S. Ulrich, *Hard multilayer coatings containing TiN and/or ZrN: A review and recent progress in their nanoscale characterization*, *J. Vac. Sci. Technol. A* 24 (2006) 554–583.
- [79] W. C. Oliver, G. M. Pharr, *An improved technique for determining hardness and elastic modulus using load and displacement sensing indentation experiments*, *J. Mater. Res.* 7 (1992) 1564–1583.

- [80] A.C. Fischer-Cripps, *Nanoindentation*, Springer, 2004.
- [81] M. Tkadletz, N. Schalk, R. Daniel, J. Keckes, C. Czettel, C. Mitterer, *Advanced characterization methods for wear resistant hard coatings: A review on recent progress*, Surf. Coat. Tech. 285 (2016) 31–46.
- [82] W. C. Oliver, G. M. Pharr, *Measurement of hardness and elastic modulus by instrumented indentation: Advances in understanding and refinements to methodology*, J. Mat. Res. 19 (2004) 3–20.
- [83] D. A. Lucca, K. Herrmann, M. J. Klopstein, *Nanoindentation: Measuring methods and applications*, CIRP Ann. Manuf. Technol. 59 (2010) 803–819.
- [84] I.N. Sneddon, *The relation between load and penetration in the axisymmetric boussinesq problem for a punch of arbitrary profile*, Int. J. Eng. Sci. 3 (1965) 47–57.
- [85] W. D. Nix, H. Gao, *Indentation size effects in crystalline materials: A law for strain gradient plasticity*, J. Mech. Phys. Solids 46 (1998) 411–425.
- [86] K. I. Schiffmann, *Area function calibration in nanoindentation using the hardness instead of Young's modulus of fused silica as a reference value*, Int. J. Mater. Res 98 (2007) 424–429.
- [87] K. Matoy, T. Detzel, M. Müller, C. Motz, G. Dehm, *Interface fracture properties of thin films studied by using the micro-cantilever deflection technique*, Surf. Coat. Tech. 204 (2009) 878–881.
- [88] K. Matoy, H. Schönherr, T. Detzel, T. Schöberl, R. Pippan, C. Motz, G. Dehm, *A comparative micro-cantilever study of the mechanical behavior of silicon based passivation films*, Thin Solid Films 518 (2009) 247–256.
- [89] A. Riedl, R. Daniel, M. Stefenelli, T. Schöberl, O. Kolednik, C. Mitterer, J. Keckes, *A novel approach for determining fracture toughness of hard coatings on the micrometer scale*, Scripta Mater. 67 (2012) 708–711.
- [90] R. Daniel, M. Meindlhumer, W. Baumegger, J. Zalesak, B. Sartory, M. Burghammer, C. Mitterer, J. Keckes, *Grain boundary design of thin films: Using tilted brittle interfaces for multiple crack deflection toughening*, Acta Mater. 122 (2017) 130–137.

- [91] R. Daniel, M. Meindlhumer, J. Zalesak, B. Sartory, A. Zeilinger, C. Mitterer, J. Keckes, *Fracture toughness enhancement of brittle nanostructured materials by spatial heterogeneity: A micro-mechanical proof for CrN/Cr and TiN/SiO_x multilayers*, *Materials & Design*. 104 (2016) 227–234.
- [92] R. Daniel, M. Meindlhumer, W. Baumegger, J. Todt, J. Zalesak, T. Ziegelwanger, C. Mitterer, J. Keckes, *Anisotropy of fracture toughness in nanostructured ceramics controlled by grain boundary design*, *Mater. Des.* 161 (2019) 80–85.
- [93] T.L. Anderson, *Fracture Mechanics: Fundamental and Applications*, CRC Press, 2017.
- [94] D. Gross, T. Seelig, *Fracture Mechanics*, Springer, 2017.
- [95] M. Meindlhumer, *Cross-sectional and High-Temperature Structure-Property Relationships in Nanocrystalline Thin Films*, 2020.
- [96] [96]H. Tada, P.C. Paris, G.R. Irwin, *The Stress Analysis of Cracks Handbook*, 3rd ed., ASME Press, 2010

List of appended publications

Publication A

Surface oxidation of nanocrystalline CVD TiB₂ hard coatings revealed by cross-sectional nano-analytics and in-situ micro-cantilever testing

D. P. Gruber, J. Zalesak, J. Todt, M. Tkadletz, B. Sartory, J.-P. Suuronen, T. Ziegelwanger, C. Czettel, C. Mitterer, J. Keckes

Published in *Surface and Coatings Technology* vol. 399 (October 2020) 126181,

DOI: 10.1016/j.surfcoat.2020.126181

Publication B

Gradients of microstructure, stresses and mechanical properties in a multi-layered diamond thin film revealed by correlative cross-sectional nano-analytics

D. P. Gruber, J. Todt, N. Wöhr, J. Zalesak, M. Tkadletz, A. Kubec, S. Niese, M. Burghammer, M. Rosenthal, H. Sternschulte, M. J. Pfeifenberger, B. Sartory, J. Keckes

Published in *Carbon* vol. 144 (April 2019) pp. 666–674,

DOI: 10.1016/j.carbon.2018.12.093.

Publication C

20 Hz synchrotron X-ray diffraction analysis in laser-pulsed WC–Co hard metal reveals oscillatory stresses and reversible composite plastification

D. P. Gruber, D. Kiefer, R. Rössler, F. Beckmann, M. Tkadletz, T. Klünsner, C. Czettel, J. Keckes and J. Gibmeier

Published in *International Journal of Refractory Metals and Hard Materials* vol. 82 (August 2019) pp. 121–128,

DOI: 10.1016/j.ijrmhm.2019.04.004.

*Surface oxidation of nanocrystalline CVD TiB₂ hard coatings revealed by cross-sectional nano-analytics and in-situ micro-cantilever testing**

David P. GRUBER ^a, Jakub ZALESK ^{a,b}, Juraj TODT ^{a,b}, Michael TKADLETZ ^b, Bernhard SARTORY ^c, Jussi-Petteri SUURONEN ^d, Tobias ZIEGELWANGER ^b, Christoph CZETTL ^e, Christian MITTERER ^b and Jozef KECKES ^{a,b}

Abstract

NANOCRYSTALLINE COATINGS OF TiB₂ grown by chemical vapour deposition (CVD) are employed *e.g.* as hard protective coatings on cemented carbide cutting tools, owing to their high wear resistance, hardness and melting point, as well as superior thermal stability. This work applied novel cross-sectional nano-analytical techniques to investigate the effects of prolonged surface oxidation of a CVD bi-layer coating of $\sim 3.4 \mu\text{m}$ thickness, consisting of a nanocrystalline TiB₂ protective top layer and a TiN diffusion-barrier bottom layer. Synchrotron X-ray diffraction with a nano-focussed 70 nm beam revealed cross-sectional phase compositions and residual stress gradients in the coating in as-deposited and oxidised states. Transmission electron microscopy showed a clear oxidation front, the existence of a $\sim 400 \text{ nm}$ thick zone of coexistence of TiB₂ and rutile TiO₂, which coincided with a marked decrease in compressive residual stress, as well as an overlying morphologically stratified TiO₂ layer. In-situ micro-cantilever experiments confirmed the structural integrity of the TiB₂ phase below the coexistence zone, where no significant oxidation-induced change in fracture stress was detected, while Young's modulus decreased by $\sim 25\%$. In conclusion, the pursued nano-analytics approach revealed detailed cross-sectional correlations between oxidation-related coating disintegration, microstructure, residual stresses and mechanical properties.

* This piece of research was first published in *Surface and Coatings Technology* vol. 399 (October 2020) 126181, DOI: 10.1016/j.surfcoat.2020.126181.

The version presented here features marginal stylistic and typographical corrections.

a Erich Schmid Institute of Materials Science, Austrian Academy of Sciences, 8700 Leoben, Austria

b Department of Materials Science, Montanuniversität Leoben, 8700 Leoben, Austria

c Materials Center Leoben Forschung GmbH, 8700 Leoben, Austria

d ESRF – The European Synchrotron, 38000 Grenoble, France

e Ceratizit Austria GmbH, 6600 Breitenwang, Austria

Introduction

HARD COATINGS OF TiB_2 combine favourable properties such as high wear resistance, high hardness and melting point, as well as good thermal stability and tribological characteristics [1–4], which render them suited for a variety of industrial applications. The outstanding physical qualities of TiB_2 can be attributed to its hexagonal crystallographic structure and specific nature of atomic bonding, in which B atoms are located in interstices between hexagonally arranged Ti atoms. The resulting lattice structure of alternating B and Ti planes that develops along the *c*-axis, with B atoms forming strong covalent B–B bonds, represents a two-dimensional B network [2, 5, 6]. TiB_2 coatings have been synthesised by both physical (PVD) and chemical vapour deposition (CVD) [7–9], with, in the main, both approaches resulting in coatings exhibiting significant compressive residual stresses [4, 10–12].

In cutting and milling operations, TiB_2 protective coatings are predominantly employed on cemented carbide inserts in the machining of Al, Ti and related alloys [6, 13, 14]. While in recent years, TiB_2 has attracted an increasing interest as a material for protective coatings, relatively few studies have been devoted to its sole role as a protective layer against oxidation [15].

In milling operations, the oxidation of hard protective coatings and associated processes can seriously affect their integrity and functionality [16, 17]. Oxide formation, related changes in phase composition, microstructure, as well as compromising of mechanical integrity, such as the formation of cracks, pores, and diffusion pathways can impair a coating in parts or result in full-scale break-down of its functional performance. While the optimisation of coating architectures based on the design of coating microstructures, interfaces, residual stress states, diffusion characteristics, and of a range of related properties can significantly enhance functional performance and thus tool lifetime [18–20], these optimisation steps, however, rely to no small extent on state-of-the-art characterisation techniques, including high-resolution cross-sectional methods [21–25]. The same applies for the assessment of detrimental effects on coatings, as *e.g.* exposure to surface oxidation. This contribution applied recently introduced, advanced characterisation techniques such as synchrotron-based cross-sectional nanobeam X-ray diffraction (CSNANOXRD) and in-situ micro-cantilever testing in concert with more traditional methods, such as transmission electron microscopy (TEM), laboratory X-ray diffraction (XRD) and differential scanning calorimetry (DSC), to study the cross-sectional oxidation behaviour of a bi-layered CVD TiN/ TiB_2 hard coating. Mechanical properties, phase composition, residual stress states, and the cross-sectional microstructure of the coating were analysed in both as-deposited and oxidised state, with the focus lying on the hexagonal TiB_2 phase and the overall structure of the oxide layer. DSC and XRD served to cross-link oxidation characteristics with oxidation-related effects in the coating, while syn-

chrotron csnanoXRD served to study gradients of phases and residual stress as a function of coating depth, in order to assess oxidation-related changes. TEM investigations allowed to image oxidation-induced coating disintegration in real space. In-situ micromechanical experiments based on micro-cantilever bending were performed in the scanning electron microscope (SEM) with the aim of comparing values of Young's modulus and fracture stress in the TiB₂ phase prior to and after the oxidation treatment.

Experimental

Coating synthesis and oxidation treatment

The coating, which was synthesised in an industrial-scale CVD plant, featured a bi-layer architecture with a face-centred cubic TiN base layer of $\sim 0.8 \mu\text{m}$ thickness, serving primarily as a barrier against B diffusion into the substrate, which would otherwise compromise coating adhesion [21, 26], and a functional top layer of hexagonal TiB₂, possessing a thickness of $\sim 2.6 \mu\text{m}$. Deposition onto mechanically polished cemented carbide substrates (11 wt% Co, 12 wt% mixed carbides, 77 wt% WC), which came in SNUN 120412 geometry (according to ISO 1842), was achieved by CVD synthesis. The TiN layer was deposited from TiCl₄-N₂-H₂ precursors at a temperature of $\sim 920^\circ\text{C}$, while the TiB₂ layer was grown from precursors of TiCl₄-BCl₃-H₂ at a temperature of $\sim 900^\circ\text{C}$. One of the coated inserts was subsequently subjected to an oxidation treatment in a furnace in ambient air for a total duration of 40 min, consisting of two isothermal stages (20 min at $T_{\text{ox}1} = 600^\circ\text{C}$ plus another 20 min at $T_{\text{ox}2} = 700^\circ\text{C}$), where the temperature accuracy in this and all further performed oxidations treatments was $\pm 5^\circ\text{C}$. The sample was placed into the preheated furnace, whereby quasi-instantaneous thermal equilibrium was assumed, given the low sample mass and high thermal conductivity of the cemented carbide material. After removal from the furnace, the sample cooled down in ambient air (without temperature control). The result was the formation of a visible oxide layer at the surface of the coating, while the overall coating structure was left intact. This oxidised sample was afterwards investigated by csnanoXRD, TEM, and micro-cantilever bending.

In addition, three further SNUN type cemented carbide cutting inserts coated with the CVD TiN/TiB₂ bi-layer architecture were subjected to isothermal oxidation in ambient air at temperatures of (a) 550°C and (b) 800°C for 10 min each, and (c) for 20 min at 600°C plus for 20 min at 700°C , and subsequently studied by grazing-incidence XRD. This served to identify oxide phases at different stages of the oxidation process.

Furthermore, in a separate deposition run, TiB₂ was deposited directly onto polycrystalline Al₂O₃ substrates, using the same CVD plant and applying identical process parameters as described above. The

deposited TiB₂ coating was then mechanically removed from its substrates and ground, resulting in a fine-grained TiB₂ powder which was subsequently investigated by DSC.

Differential scanning calorimetry and XRD

A *Setaram Setsys Evo 2400* type differential scanning calorimeter was employed to perform a DSC measurement in conjunction with a thermogravimetric analysis (TGA) on TiB₂ powder of 20.06 mg initial mass in the temperature range from room temperature up to 1200 °C. The experiment was carried out in synthetic air, using a constant heating rate of 10 K/min.

XRD measurements were carried out on oxidised coated cutting inserts as described in the section about coating synthesis, using a *Rigaku SmartLab* diffractometer. These samples were measured in grazing-incidence geometry with Cu-K α radiation at an angle of incidence of 1.25°. The measurements were performed in the range of 2 θ –75° at an angular resolution of 0.05°. The aim was to identify individual phases of oxidation products, which could potentially be cross-linked to phases revealed in the oxidised coating studied by CSnanoXRD.

Synchrotron nanobeam XRD characterisation

The TiN/TiB₂ coating was studied using a CSnanoXRD measurement set-up with a high-energy nano-focussed synchrotron X-ray beam at the ID16B beamline of the European Synchrotron Radiation Facility (ESRF) in Grenoble, France, to investigate depth gradients of the residual stress state and reveal oxidation-induced phase changes. Samples were prepared from the TiN/TiB₂ bi-layer coating on cemented carbide cutting inserts in as-deposited as well as in oxidised state in the shape of thin transmission lamellae. This involved precision cutting using a *Struers Accutom 50* cut-off machine and a final manual mechanical thinning step, resulting in lamella dimensions of $\sim 6.5 \times \sim 4 \text{ mm}^2$ and a final thickness of $L \sim 50 \mu\text{m}$ in the X-ray beam direction (*cf.* Fig. 1).

The CSnanoXRD experiment was performed in transmission geometry with an X-ray beam (photon energy 29.6 keV) focussed by a pair of Kirkpatrick-Baez (KB) mirrors to dimensions of $\sim (70 \times 70) \text{ nm}^2$ (Fig. 1). The sample lamellae were moved with respect to the X-ray beam by a piezo-actuated stage along the coating normal direction z with a constant step size of 100 nm. For each z -step, the diffracted intensity was recorded on a two-dimensional (2D) charged-coupled device (CCD) detector, resulting in a scanning of the coatings in out-of-plane direction. The CCD detector (*FReLoN 4M*) featured a resolution of 2048 by 2048 pixels at a pixel size of $(51.3 \times 51.7) \mu\text{m}^2$. A NIST LaB₆ standard measured at the same

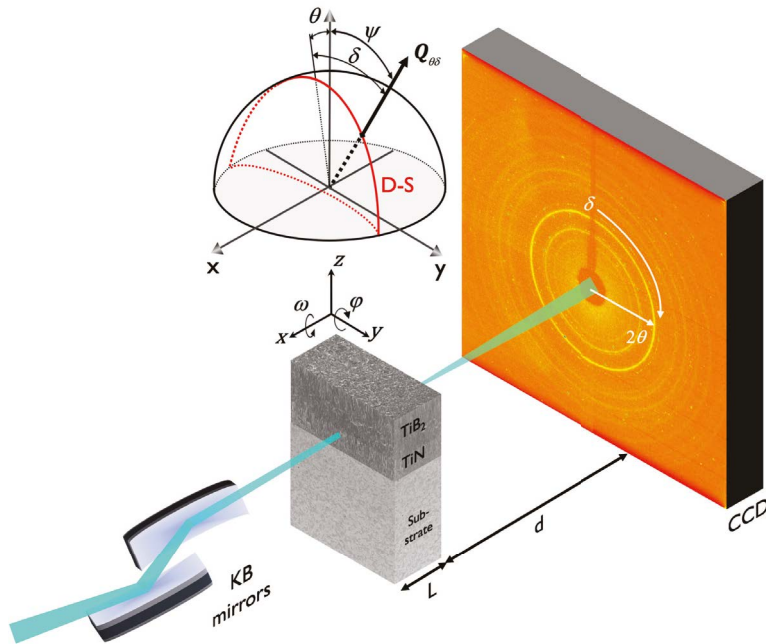


FIGURE 1: Schematic drawing of the CSnanoXRD set-up at beamline ID16B of ESRF, Grenoble. The experiment was performed in transmission geometry using KB mirrors to focus the synchrotron X-ray beam ($E = 29.6$ keV) to a cross-section of $\sim (70 \times 70)$ nm. Lamellae of the samples ($L \sim 50 \mu\text{m}$) comprising the TiN/ TiB_2 coating on the cemented carbide substrate in as-deposited as well as in oxidised state were scanned along the z -direction in equidistant steps of 100 nm, while the diffraction signal was recorded at every sample position by the 2D detector (*FReLoN 4M*) at a sample-to-detector distance of ~ 115 mm. The azimuthal angle δ was counted from the 12 o'clock detector position and defined in clockwise direction as indicated on the detector plane in the schematic.

sample-to-detector distance as the sample lamellae served to calibrate the powder diffraction experimental geometry of the set-up. Based on the Debye-Scherrer (DS) rings acquired from the NIST standard, the sample-to-detector distance d was calibrated to 115 mm, together with the tilt angle of the detector plane of 0.409° , the rotation angle of the tilt plane of 171.19° and the beam centre of the detector at 998.2 and 934.6 pixels (in horizontal and vertical directions). The Python package *pyFAI* [27] was used to process the recorded DS rings from both sample lamellae, whereby a contour plot of integrated intensity distribution $I(\vartheta, z)$ (henceforth denoted as *phase plot*) was generated from the recorded diffraction patterns. In addition, depth gradients of in-plane X-ray elastic strains $\varepsilon_{011}(z)$ for the TiB_2 011 reflection were retrieved. Residual stress gradients $\sigma_r(z)$ were subsequently calculated from the measured strains $\varepsilon_{011}(z)$, applying an assumed X-ray elastic constant $1/2 S_2$ of $0.1841 \times 10^{-11} \text{ Pa}^{-1}$, which was itself calculated by the Hill grain interaction model from TiB_2 monocrystal elastic constants [28]. A dedicated correction resting on a finite element model was applied to the evaluated strain and stress values for the stress relaxation caused by the lamella preparation [29]. For an in-depth description of the experimental approach and related evaluation procedure, we refer to previous reports [29–31].

Transmission electron microscopy analysis

A cross-sectional TEM lamella was prepared by focussed ion beam (FIB) milling, using the standard lift-out technique in a *Zeiss Auriga* workstation from the oxidised coating at accelerating voltages of 5–30 kV and beam currents of 50 pA to 20 nA. This involved depositing a thin protective Pt film of $\sim 2 \mu\text{m}$ thickness onto the surface of the coating in order to minimise Ga contamination from the ion beam. Special care was taken not to damage the oxide film.

A bright field scanning transmission electron microscopy (BF STEM) investigation of the sample lamella was performed in a *JEOL 2200FE* microscope at an accelerating voltage of 200 kV and an effective spot size of $\sim 0.5 \text{ nm}$, using a BF detector to image the structural and morphological cross-sectional composition of the oxidised coating.

The same cross-sectional lamella was subsequently investigated in a *FEI Titan Themis* TEM, where energy-dispersive X-ray spectroscopy (EDS) elemental maps of the coating cross-section and high angular annular dark-field (HAADF) images were collected in STEM mode at an accelerating voltage of 300 kV, using a beam current of 1.5 nA. The recorded EDS spectra were processed using built-in standards in *FEI Velox* software to gain information of elemental cross-sectional distributions within the oxidised coating.

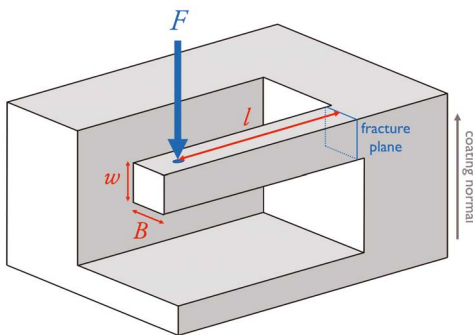


FIGURE 2: Schematic drawing of a micro-cantilever specimen, where bending length l is the distance between the point of applied load and the resulting fracture plane, while w and B are dimensions in out-of-plane and in-plane direction, respectively. Testing was performed with the applied force F (blue arrow) acting parallel to the coating normal, in out-of-plane direction, as indicated by the grey arrow.

Micro-cantilever experiments

Mechanical properties of the TiB_2 layers from the sample in as-deposited state as well as from the oxidised sample were investigated by in-situ micro-cantilever experiments in the SEM, followed by an evaluation procedure based on classical linear-elastic theory of fracture mechanics [32]. The micro-cantilever specimens were milled in a FIB workstation (*Zeiss Auriga*), using an acceleration voltage of 30 kV and beam currents ranging from 20 nA for coarse pre-cuts to 50 pA for final polishing. Fig. 2 shows a schematic drawing of a micro-cantilever specimen, while an SEM image of a bending beam from the coating in as-deposited state is presented in in-plane view in Fig. 3. A total of nine cantilevers were fabricated, five specimens from the as-deposited sample having dimensions of ($B \sim 1.8 \times w \sim 1.5$) μm^2 , and four specimens from the oxidised samples, cut to dimensions of ($B \sim 1.9 \times w \sim 1.6$) μm^2 . Effective bending lengths in testing were between ~ 6.0 to $\sim 6.9 \mu\text{m}$. Special care was taken and low milling currents employed during final stages of the milling operations in order to minimise the adverse effects of impinging Ga ions on the specimens. The cantilevers themselves were placed and dimensioned within the TiB_2 layer as to not extend into the overlying oxide film of the oxidised sample, *i.e.* the w dimension of the beams extended from coating height $\sim 0.9 \mu\text{m}$ to $\sim 2.5 \mu\text{m}$ (Fig. 8). Cantilever dimensions were subject to small variations due

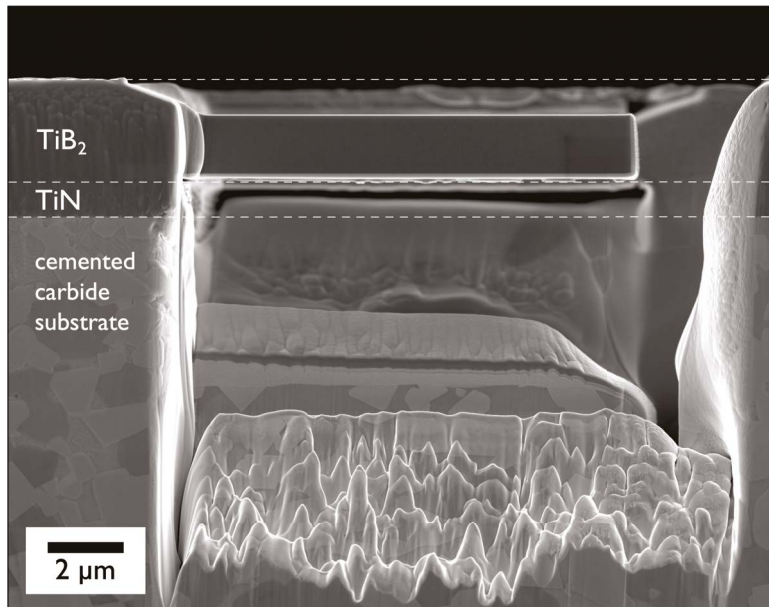


FIGURE 3: Cross-sectional secondary electron SEM image a micro-cantilever fabricated from the TiB₂ layer of the TiN/TiB₂ bi-layer coating in as-deposited state. The bi-layer architecture of the coating is visible on the left due to a slight difference in cross-sectional surface roughness, stemming from different grain morphologies between the nanocrystalline TiB₂ and the relatively coarser grained TiN layers.

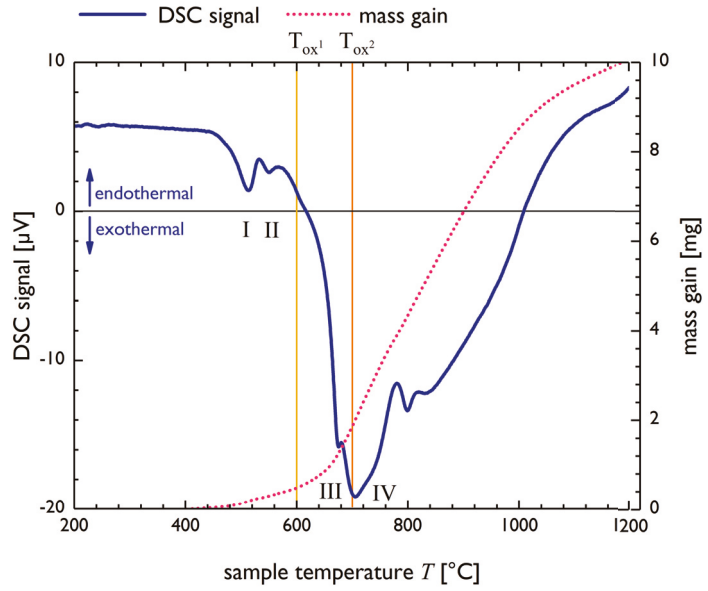
to the FIB fabrication process. Precise cross-sections for all tested micro-cantilevers were determined in the SEM prior to testing, as well as in post-mortem examinations of the fracture planes of the broken cantilevers. All specimens were tested in un-notched state to examine values of Young's modulus and fracture stress. The experiments were carried out in in-situ SEM (*Zeiss LEO 982*) configuration, using a dedicated depth-sensing nanoindenter system (*Hysitron Pi-85 PicoIndenter*), featuring a piezo-actuated sample stage. Each individual micro-cantilever specimen was loaded with a sphero-conical diamond indenter tip (radius of curvature ~ 700 nm) in out-of-plane direction up to its load of fracture. Special attention was paid to sample alignment and to load the bending beams along their centre lines in order to avoid unwanted torque. A constant displacement rate of 20 nm/s in the experiments ensured quasi-static loading conditions. The slopes of the recorded load-deflection curves were subsequently used to calculate values of Young's modulus, reflecting the intrinsic elastic properties of a stress-free and free-standing coating.

Based on the recorded load-deflection data, fracture stress σ_s was evaluated as

$$\sigma_s = 6 \frac{Fl}{Bw^2},$$

with F being the maximum applied load at fracture of the bending beam, l the bending length, representing the distance between the point of applied force and the root of the specimen, and B and w being the cantilever width and thickness, respectively. The evaluation of Young's modulus E rested on the assumption of an ideally brittle material, where plastic deformation effects of the tested material in contact with the indenter tip were excluded. The recorded dominant elastic response from cantilever loading was thus used to calculate E

FIGURE 4: DSC profile and TG measurement performed on ground TiB_2 powder, shown in the temperature range from 200–1200°C. The dsc profile indicates exothermic events in the vicinity of $T \sim 520^\circ\text{C}$ and $\sim 545^\circ\text{C}$ (I, II) as well as at $T \sim 675^\circ\text{C}$ and $\sim 700^\circ\text{C}$ (III, IV). Markers $T_{\text{ox}1}$ and $T_{\text{ox}2}$ indicate the isothermal oxidation temperatures applied to the coating on cutting inserts, which were studied by CSnanoXRD, TEM, and micro-cantilever experiments.



according to

$$E = \frac{4F}{\delta B} \times \left(\frac{l}{w}\right)^3,$$

with δ being the displacement at the maximum applied load F .

Results and discussion

DSC and XRD measurements

The DSC profile for the ground TiB_2 powder is shown together with the recorded TGA signal in Fig. 4, where temperatures $T_{\text{ox}1}$ and $T_{\text{ox}2}$ indicate the isothermal holding temperatures in the oxidation treatment of the coated cutting inserts. The measured DSC profile shows two distinct exothermic peaks at $\sim 520^\circ\text{C}$ (I) and $\sim 545^\circ\text{C}$ (II). Further peaks can be identified at $\sim 675^\circ\text{C}$ (III) and $\sim 700^\circ\text{C}$ (IV). A similar pattern was reported by Andrievskii *et al.* [33], when studying the oxidation of TiB_2 micro and nanoparticles, where peak I was linked to the exothermic reaction $2\text{TiB}_2 + 5\text{O}_2 \rightarrow 2\text{TiO}_2 + 2\text{B}_2\text{O}_3$ (1), while peaks III and IV were connected to reaction $3\text{TiB}_2 + 7\text{O}_2 \rightarrow 2\text{B}_2\text{O}_3 + 2\text{TiBO}_3$ (2). The recorded TG profile shows a small but continuous TG weight gain above $\sim 420^\circ\text{C}$, as a consequence of reaction (1), which is, most likely suppressed by the emergence of a surface film of B_2O_3 , acting as an O barrier; *cf.* [15]. However, contrary to the report from Huang *et al.* [15], where between $\sim 400^\circ\text{C}$ and $\sim 450^\circ\text{C}$, a TG weight loss was found and explained with partial volatilisation of the B_2O_3 film, such a trend is not apparent in the TG signal in Fig. 4. Liquification and subsequent volatilisation of the B_2O_3 film beyond $\sim 450\text{--}500^\circ\text{C}$ increasingly exposed the underlying coating to exothermic reaction (1), resulting

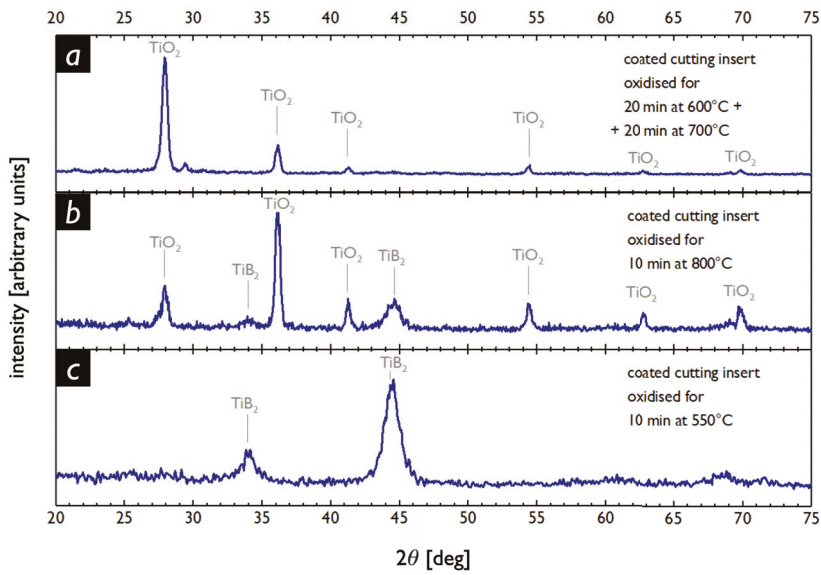


FIGURE 5: Laboratory XRD diffractograms measured in grazing-incidence geometry on coated cutting inserts subjected to different oxidation treatments, showing pronounced diffraction peaks for the rutile TiO₂ and TiB₂ phases, while suspected B₂O₃ and TiBO₃ phases could not be detected.

in a marked TG weight gain at $\sim 650^\circ\text{C}$.

The measured grazing-incidence XRD patterns presented in Fig. 5 confirm the dominant presence of the rutile TiO₂ phase for all samples except the coating oxidised at 550°C for 10 min (Fig. 5c), where apparently no oxidation at a significant level occurred. In contrast, neither of the measured profiles indicated the presence of the B₂O₃ and TiBO₃ phases. This fact is attributed to (i) the low melting point of B₂O₃ ($\sim 450^\circ\text{C}$) and its volatility at elevated temperatures, as well as (ii) the potentially relatively small volume fraction of the phase in the investigated surface oxide film. Similar findings were reported by [15], where neither B₂O₃ nor TiBO₃ could be identified by XRD at temperatures up to 900°C , as well as by [34] for the oxidation of monolithic TiB₂ at 850°C , where also only the TiO₂ phase could be unambiguously indexed and (iii) the possible existence of the suspected oxides in non-crystalline form.

Synchrotron CSnanoXRD

Phase analysis

Scanning of the samples in z -direction in the CSnanoXRD set-up provided insight into the depth-dependent phase composition of the coating system prior to and after the oxidation treatment. The phase plots presented in Fig. 6a,b show the integrated intensity as a function of the diffraction angle 2ϑ and coating height z , resulting in an integrated intensity distribution $I(\vartheta, z)$, as obtained by 0 – 360° integration of individual coating height-specific CSnanoXRD diffraction patterns along the azimuthal angle ϑ . The coating height was defined to be $z = 0$ at the substrate/TiN interface. The patterns clearly showed the formation of the oxide film in the near-surface re-

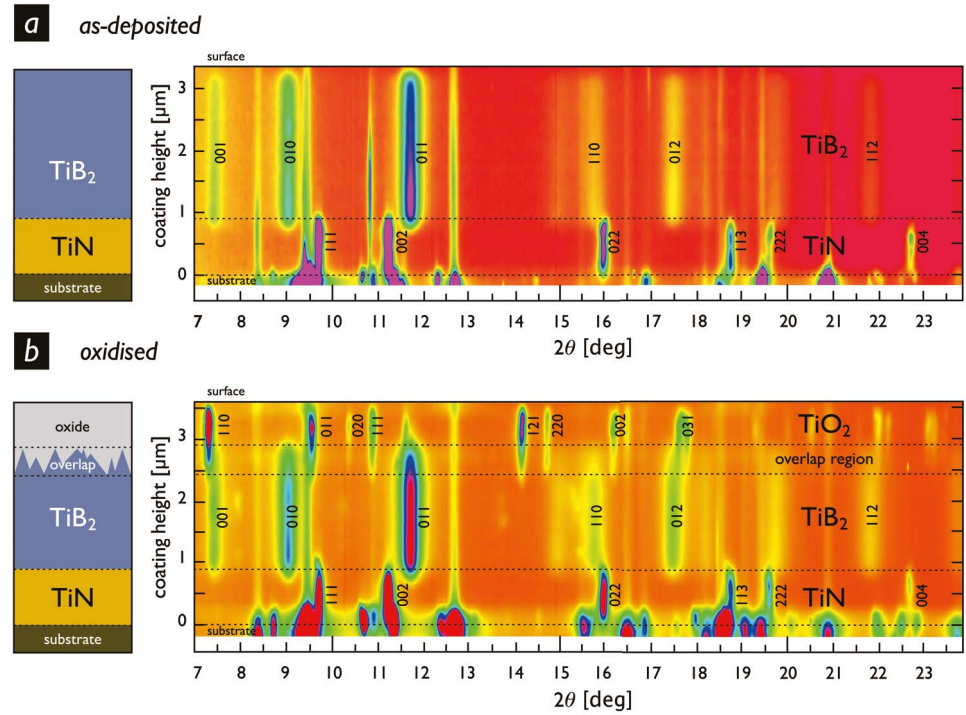


FIGURE 6: The cross-sectional phase composition of the TiN/TiB₂ bi-layer coating was revealed in as-deposited (a), and oxidised state (b) in contour plots of integrated intensity distribution $I(\theta, z)$ (with $z = 0$ set to be at the substrate/TiN interface). Intensity information is presented in arbitrary units and not normalised between sub-graphs a and b for reasons of improved peak visibility. TiN, TiB₂ and TiO₂ reflections are indicated, whereas WC peaks (in some cases extending across the coating due to their high intensity coupled with pronounced X-ray beam tails) are not denoted for simplicity. Schematic drawings on the left-hand side aid to identify the cross-sectional layers of individual phases.

region of the TiB₂ layer, while also indicating that lower regions of the coating did not undergo such an oxidation process. In Fig. 6a & b, overlapping of peaks between individual phases in z -direction reflected in-plane interface roughness, *i.e.* in beam direction. In Fig. 6b, the pronounced overlapping of peaks between the TiB₂ and TiO₂ phases hinted at the local co-existence of these phases in the oxidised sample. This region is henceforth denoted as *overlap region*. Neither B₂O₃ nor other oxide phases could be detected or indexed on top or within the rutile TiO₂ film. This, as in the case of laboratory XRD measurements, was related to the volatility of the B₂O₃ and TiBO₃ phases, which were assumedly lost during the oxidation process, the relatively small volume fraction of remaining oxide phases and/or their possible existence in non-crystalline form. The dominant occurrence of the rutile phase and its corresponding diffraction peaks in Fig. 6b is in agreement with laboratory XRD data from similar oxidation experiments, *cf.* [33, 35], as well as with the results from grazing incidence XRD presented in Fig. 5, which however unlike the CSNANOXRD phase plot do not give insight into the depth evolution of the phase peaks.

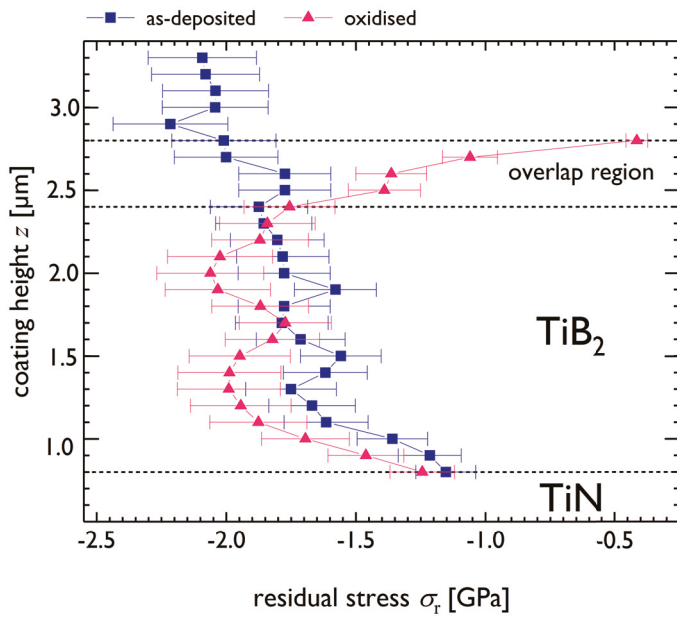


FIGURE 7: TiB₂ residual stress state as a function of coating height (with $z = 0$ set to be at the substrate/TiN interface) determined by synchrotron cSnanoXRD for the coating in as-deposited and oxidised state, respectively. Error bars indicate the estimated 10% error in measured stress due to limitations inherent to the experimental set-up and data evaluation.

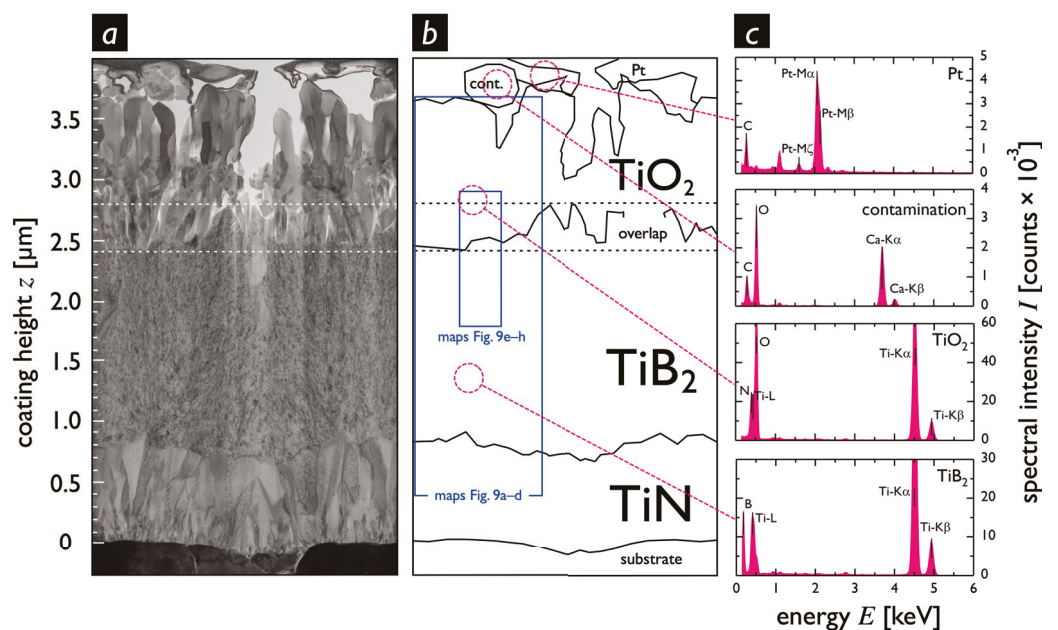
Residual stress evaluation

Cross-sectional residual stress profiles acquired by synchrotron cSnanoXRD in the TiB₂ layer are presented in Fig. 7 for the coating in as-deposited and oxidised state, respectively. Stress levels in the TiB₂ phase were found to be in the compressive domain, ranging from $\sigma_r \sim -1.2$ GPa at the TiN/TiB₂ interface, up to ~ -2 GPa close to the as-deposited sample's surface. The as-deposited sample profile showed a gradual increase in compressive stress with increasing coating height. An equivalent pattern, albeit with higher absolute compressive stress values was also reported in [4], where the origin of the compressive stresses was identified to be a combination of (i) the distinctly nanocrystalline nature of the TiB₂ phase as a consequence of strong covalent B-B bonds and the prevalent sub-stoichiometry (B deficiency), (ii) potential early growth stage local epitaxy, (iii) low thermal coefficients of expansion compared to TiN and cemented carbide as well as (iv) the elastic anisotropy of the TiB₂ phase. Furthermore, the gradual stress increase with coating height is reported to be caused by a gradient in TiB₂ domain size related to a rising B content with increasing coating height [4]. In the case of the oxidised sample, the stress profile follows the trend of gradually increasing compressive stress up to a coating height of ~ 2.1 μm . Slightly higher values were measured in case of the oxidised sample, while both profiles matched within their estimated 10% margins of error. Starting at the onset of the overlap region at $z \sim 2.4$ μm , a sharp but continuous decrease in stress in the oxidised sample was found. This rapid relaxation of σ_r throughout the TiB₂/oxide overlap zone can clearly be linked with oxidation-related coating disintegration, including the potential formation of nanoscale crack networks and/or the generally porous nature of the material.

FIGURE 8: Cross-sectional BF STEM image (a), corresponding conceptual sketch, indicating the position and roughness of interfaces between individual phases and regions (b), and EDS spectra for selected areas of the lamella (c). Fig. 8b furthermore indicates the positions of HAADF STEM images and corresponding EDS elemental maps presented in Fig. 9. The relatively rough interface region between the TiB_2 and TiO_2 layers, where both phases coexist (overlap region), coincided with the marked but continuous decrease in compressive residual stress, measured by CSnanoXRD. The coating surface was covered by a thin layer of Pt remaining after FIB lamella preparation, and also showed slight contamination with carbon compounds originating from the FIB gas injection system. Coating height was defined to be $z = 0$ at the substrate/ TiN interface.

STEM cross-sectional analysis and EDS elemental mapping

Direct insight into the microstructural composition of the coating system following the oxidation treatment is provided by cross-sectional BF STEM imaging. In Fig. 8a & b, individual coating sublayers can clearly be distinguished by their varying characteristic morphological features. The TiN layer is composed of distinct elongated columnar crystallites, with grain size rapidly evolving along the growth direction. In the nucleation region bordering on the cemented carbide interface, crystallites are found to be smaller than 100 nm in length, while on top of this zone, individual columnar grains extend over more than 500 nm in the direction of coating growth. This results in increased roughness of the TiN/TiB_2 interface at a coating height of $z \sim 0.8 \mu\text{m}$. The overlying TiB_2 layer is of nanocrystalline nature with individual crystallite sizes too small to be discerned in the image. No apparent changes in the TiB_2 phase could be detected below a coating height of $z \sim 2.4 \mu\text{m}$, where the integrity of the material remained intact and neither cracks nor diffusion channels are present. Above $z \sim 2.4 \mu\text{m}$ the image revealed in detail the zone of $\sim 400 \text{ nm}$ thickness, which was identified in the CSnanoXRD phase plot as overlap region. In addition, the BF STEM image shows the inhomogeneous nature of this zone, which is characterised by the local co-existence of the TiB_2 and rutile TiO_2 phases, with sections of nanocrystalline uncompromised TiB_2 and comparably coarse and needle-like oxide grains. Voids and diffusion pathways between the two phases are present but relatively small scale. At a coating height of $z \sim 3 \mu\text{m}$, where, according to the CSnanoXRD data, no TiB_2 is present anymore, oxide grains appear smaller and comparably globular in shape, before again developing into large and needle-like TiO_2



crystallites between $z \sim 3.2 \mu\text{m}$ and $z \sim 3.7 \mu\text{m}$. This threefold morphological stratification in oxide microstructure can be related to the oxidation treatment with two distinct isothermal holding temperatures, but could potentially also be related to intrinsic characteristics of crystal growth of the TiO₂ phase. The topmost, discontinuous layer discernible just below the protective Pt film in Fig. 8a & b was identified as surface contamination with unspecified carbon compounds, which most probably resulted from sample handling after the oxidation treatment. Cross-sectional EDS elemental composition maps of two selected regions of the sample lamella, which are indicated by blue rectangles in Fig. 8b, are presented in Fig. 9. In combination with the associated integrated EDS spectra shown in Fig. 8c, these elemental maps supported the previous findings by correlating individual z regions of the oxidised coating with associated chemical elements and furthermore revealed, that no B₂O₃ oxide phase was present in the investigated oxide film. Detailed elemental mapping of the TiB₂/oxide boundary region Fig. 9e–h additionally confirmed the relatively sharp nature of this interface, with no apparent oxygen diffusion into or disintegration of the underlying monolithic TiB₂ coating.

Micro-cantilever testing

Load-deflection data recorded in micro-cantilever testing were used to evaluate Young's modulus E and fracture stress σ_s in the TiB₂ layer of the coating system in as-deposited as well as oxidised state. Corresponding stress-displacement data are presented in Fig. 10, while mean values and associated standard errors for E and σ_s are collected in Tab. 1. The data revealed a decrease of $\sim 25\%$ in Young's modulus from $E = 467 \pm 22 \text{ GPa}$ (as-deposited coating) to $E = 348 \pm 15 \text{ GPa}$ (TiB₂ below the oxide layer in the oxidised coating). A comparable if somewhat larger decrease in E from $\sim 290 \text{ GPa}$ to $\sim 190 \text{ GPa}$ measured by nano-indentation was reported by Mao *et al.* for TiB₂ monolayers deposited by magnetron sputtering after oxidation in air at 600°C [36]. While there are only few reports on the Young's moduli of TiB₂ deposited by CVD, with values ranging from $\sim 352 \text{ GPa}$ [37] to $\sim 540 \text{ GPa}$ [14], more data are available for E values of sputter deposited TiB₂ films. They range from $\sim 120\text{--}200 \text{ GPa}$ [38] to $\sim 550 \text{ GPa}$ [39]. Given this spread, which is a consequence of differences in coating microstructures, mass densities, stoichiometries and defect densities as well as limitations to the employed experimental approaches, the determined as-deposited value of $E \sim 467 \text{ GPa}$ is in good agreement with other reports. Previous results reported by Schalk *et al.* [4], where a TiB₂ coating grown with the same deposition parameters was studied by glow discharge optical emission spectroscopy to quantify its elemental composition, showed a slight sub-stoichiometry, where the B-to-Ti ratio was found to increase from ~ 1.8 at the TiN/TiB₂ interface to ~ 1.9 close to the TiB₂ layer surface. The de-

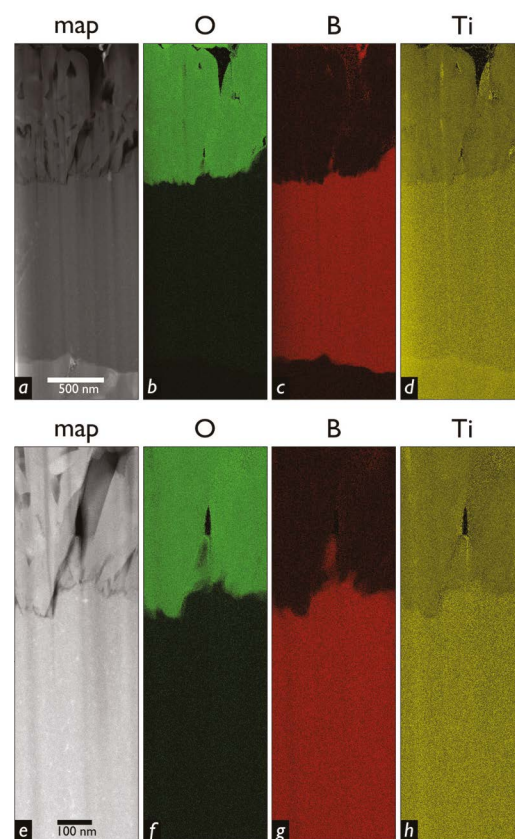
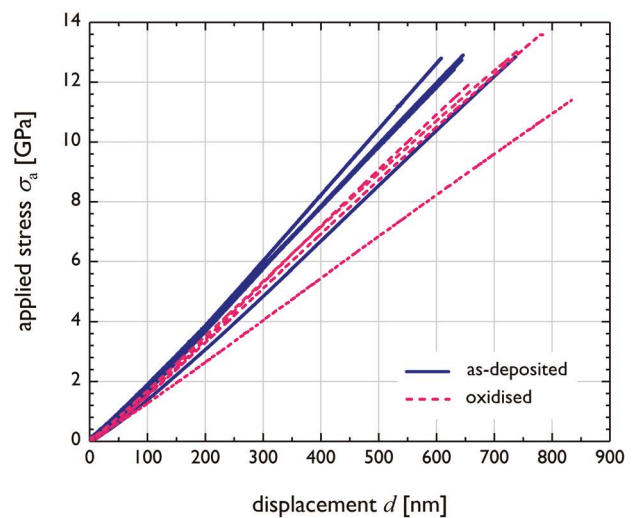


FIGURE 9: Cross-sectional HAADF STEM images (a,e) and corresponding EDS elemental maps (b–d, f–h), showing the same lamella region in two different magnifications. Map positions on the TEM lamella are indicated in Fig. 8b. The entire TiB₂ layer is mapped in panels a–d, displaying both the TiN/TiB₂, as well as the TiB₂/oxide interfaces. Detailed imaging of the TiB₂/oxide boundary region in panels e–h confirms the relatively sharp nature of this interface, with no apparent cracks or porosity visible in the underlying TiB₂ coating.

terminated value of Young's modulus for the as-deposited TiB_2 layer is thus assumed to be affected by its prevalent sub-stoichiometric nature. The oxidation-induced effect on fracture stress was negligible and found to be within the associated margins of standard errors, changing from $\sigma_s = 12.1 \pm 1.0$ GPa (as-deposited coating) to $\sigma_s = 12.5 \pm 0.9$ GPa (TiB_2 below the oxide layer in the oxidised coating). Fracture stress values for other CVD hard coatings based on micro-cantilever bending are reported as ~ 3.9 GPa (TiN), ~ 7.3 GPa (TiBN) and ~ 8.1 GPa (TiBCN) [40, 41], underlining the relatively high strength of ~ 12.1 GPa of the TiB_2 coating studied in this contribution. This is thought to be linked to (i) the intrinsically strong bonding in TiB_2 as well as (ii) the particularly dense microstructure and nanocrystalline nature present in the investigated coating, which are both connected to the CVD process. The result of comparable values of σ_s of TiB_2 for both investigated samples can furthermore be correlated with findings from BF STEM and CSNANOXRD and points at the absence of micro cracks, pores, or diffusion channels which would have significantly reduced fracture stress. Full microstructural integrity of the TiB_2 phase below the overlap region can thus be assumed. Together with the clear oxidation front visible below the overlap region at $z \sim 2.4 \mu\text{m}$ in Fig. 8a this proved the good stability of the TiB_2 coating when subjected to prolonged surface oxidation. Given the fact that no microstructural change was observed in the depth region of the coating from which the cantilever specimens were fabricated, it is reasonable to assume that the measured significant decrease in Young's modulus was, in contrast to the results from [36], not directly related to the oxidation of overlying material or

FIGURE 10: Representative curves of applied stress σ_a versus beam displacement d for TiB_2 micro-cantilever specimens from the as-deposited (blue, continuous) and oxidised (magenta, dashed) sample, as recorded in SEM in-situ experiments.



intrinsic structural changes, but to a greater degree a consequence of prolonged elevated temperature impact during the oxidation treatment. At an exposure of the samples to a maximum temperature of 700 °C for 20 min, annihilation of crystallographic defects and atomic rearrangement can be assumed as a potential reason for the reduction in E [4, 42].

Summary and Conclusions

A combined correlative nano-analytics study including synchrotron CSnanoxrd, laboratory XRD, BF and HAADF STEM imaging, EDS elemental mapping and micro-cantilever bending experiments was performed on an oxidised bi-layer coating that consisted of a TiN diffusion barrier base layer and a hexagonal TiB₂ protection layer, grown by CVD onto cemented carbide cutting inserts. Additional data was gathered by laboratory XRD performed on coated inserts and a DSC measurement on oxidised TiB₂ powder. The results provide detailed insights into the cross-sectional oxidation-induced changes within the TiB₂ coating and allowed to correlate cross-sectional profiles of phases, residual stress and microstructural constitution. The study revealed (i) favourable resistance to prolonged surface oxidation (20 min at 600 °C plus 20 min at 700 °C) of the investigated CVD TiN/TiB₂ coating, which protected the underlying TiB₂ layer region, the TiN layer and WC/Co substrate from degradation, (ii) the formation of a transition zone labelled overlap region formed by oxidation, where intact TiB₂ and rutile phase TiO₂ co-existed, (iii) a clear oxidation front separating this overlap region from unaffected TiB₂, as well as (iv) a ~25% reduction in Young's modulus of the TiB₂ underneath the oxide film in the oxidised sample relative to its untreated counterpart, while (v) no significant difference in TiB₂ fracture stress levels was detected between the samples. Furthermore, (vi) pronounced relaxation of residual stress in the TiB₂ phase was measured in the case of the oxidised sample, coinciding with the discovered overlap region. This is thought to be connected with the introduction of cracks and pores in the TiB₂ phase as well as the generally porous nature of this zone. Cross-sectional BF STEM imaging revealed (vii) a stratified grain morphology of the TiO₂ layer. Supplementary experiments on TiB₂ powder using DSC and coated cutting inserts using XRD, in order to clarify the specific oxidation characteristics were in agreement with findings of the cross-sectional study, confirming (viii) the absence of the volatile B₂O₃ phase or other oxidation products in crystalline form.

Acknowledgements

The authors gratefully acknowledge the financial support under the scope of the COMET program within the K2 Centre *Integrated Computational Material, Process and Product Engineering* (IC-MPPE) (Project No. 859480).

This program is supported by the Austrian Federal Ministries for Transport, Innovation and Technology (BMVIT) and for Digital and Economic Affairs (BMDW), represented by the Austrian research funding association (FFG), and the federal states of Styria, Upper Austria and Tyrol.

CzechNanoLab project LM2018110 funded by MEYS CR is gratefully acknowledged for the financial support of the measurements at CEITEC Nano Research Infrastructure.

The authors acknowledge the ESRF for provision of synchrotron radiation facilities on beamline ID16B.

References

- [1] F. J. G. Silva, R. C. B. Casais, R. P. Martinho, A. P. M. Baptista, *Mechanical and tribological characterization of TiB₂ thin films*, J. Nanosci. Nanotechnol. 12 (12) (2012) 9187–9194.
- [2] R. G. Munro, *Material properties of titanium diboride*, J. Res. Natl. Inst. Stand. Technol. 105 (5) (2000) 709–720.
- [3] S. Shimada, M. Takahashi, H. Kiyono, J. Tsujino, *Coatings and microstructures of monolithic TiB₂ films and double layer and composite TiCN/TiB₂ films from alkoxide solutions by thermal plasma CVD*, Thin Solid Films 516 (19) (2008) 6616–6621.
- [4] N. Schalk, J. Keckes, C. Czettl, M. Burghammer, M. Penoy, C. Michotte, C. Mitterer, *Investigation of the origin of compressive residual stress in CVD TiB₂ hard coatings using synchrotron X-ray nanodiffraction*, Surf. Coat. Technol. 258 (2014) 121–126.
- [5] J. Etourneau, P. Hagenmuller, *Structure and physical features of the rare-earth borides*, Philos. Mag. B 52 (3) (2006) 589–610.
- [6] H. O. Pierson, A. W. Mullendore, *Thick boride coatings by chemical vapor deposition*, Thin Solid Films 95 (2) (1982) 99–104.
- [7] H. O. Pierson, *Handbook of Chemical Vapor Deposition*, William Andrew, 2012.
- [8] U. Schleinkofer, C. Czettl, C. Michotte, *Coating applications for cutting tools*, Comprehensive Hard Materials, 2014, pp. 453–469.
- [9] E. Kelesoglu, C. Mitterer, M. K. Kazmanli, M. Ürgen, *Microstructure and Properties of Nitride and Diboride Hard Coatings Deposited Under Intense Mild-energy Ion Bombardment*, presented at the Surface and Coatings Technology, vol. 116, (1999), pp. 133–140.
- [10] M. Berger, M. Larsson, S. Hogmark, *Evaluation of magnetron-sputtered TiB₂ intended for tribological applications*, Surf. Coat. Technol. 124 (2) (2000) 253–261.
- [11] M. Berger, L. Karlsson, M. Larsson, S. Hogmark, *Low stress TiB₂ coatings with improved tribological properties*, Thin Solid Films 401 (1) (2001) 179–186.
- [12] H. Oettel, R. Wiedemann, *Residual stresses in PVD hard coatings*, Surf. Coat. Technol. 76 (1995) 265–273.

- [13] C. Mitterer, *PVD and CVD hard coatings*, Comprehensive Hard Materials, 2014, pp. 449–467.
- [14] R. Kullmer, C. Lugmair, A. Figueras, J. Bassas, M. Stoiber, C. Mitterer, *Microstructure, mechanical and tribological properties of PACVD Ti(B,N) and TiB₂ coatings*, Surf. Coat. Technol. 174 (2003) 1229–1233.
- [15] X. Huang, S. Sun, G. Tu, *Investigation of mechanical properties and oxidation resistance of CVD TiB₂ ceramic coating on molybdenum*, J. Mater. Res. Technol. (2019) 1–9.
- [16] K. Bobzin, *High-performance coatings for cutting tools*, CIRP J. Manuf. Sci. Technol. 18 (2017) 1–9.
- [17] X. Chen, H. Liu, Q. Guo, S. Sun, *Oxidation behavior of WC–Co hard metal with designed multilayer coatings by CVD*, Int. J. Refract. Met. Hard Mater. 31 (2012) 171–178.
- [18] R. Daniel, M. Meindlhumer, W. Baumegger, J. Zalesak, B. Sartory, M. Burghammer, C. Mitterer, J. Keckes, *Grain boundary design of thin films: using tilted brittle interfaces for multiple crack deflection toughening*, Acta Mater. 122 (2017) 130–137.
- [19] R. Daniel, M. Meindlhumer, J. Zalesak, B. Sartory, A. Zeilinger, C. Mitterer, J. Keckes, *Fracture toughness enhancement of brittle nanostructured materials by spatial heterogeneity: a micro-mechanical proof for CrN/Cr and TiN/SiO_x multilayers*, Mater. Des. 104 (2016) 227–234.
- [20] J. Todt, R. Pitonak, A. Köpf, R. Weißenbacher, B. Sartory, M. Burghammer, R. Daniel, T. Schöberl, J. Keckes, *Superior oxidation resistance, mechanical properties and residual stresses of an Al-rich nanolamellar Ti_{0.05}Al_{0.95}N coating prepared by CVD*, Surf. Coat. Technol. 258 (2014) 1119–1127.
- [21] M. Tkadletz, N. Schalk, C. Mitterer, J. Keckes, M. Pohler, C. Czettel, *Cross-sectional characterization techniques as the basis for knowledge-based design of graded CVD TiN–TiB₂ coatings*, Int. J. Refract. Met. Hard Mater. 71 (2018) 280–284.
- [22] M. Bartosik, J. Keckes, P.O.Å. Persson, H. Riedl, P. H. Mayrhofer, *Interface controlled microstructure evolution in nanolayered thin films*, Scr. Mater. 123 (2016) 13–16.
- [23] J. Zalesak, M. Bartosik, R. Daniel, C. Mitterer, C. Krywka, D. Kiener, P. H. Mayrhofer, J. Keckes, *Cross-sectional structure-property relationship in a graded nanocrystalline Ti_{1-x}Al_xN thin film*, Acta Mater. 102 (2016) 212–219.

- [24] H. Li, T. Koyanagi, X. Hu, Y. Katoh, *Multiscale experimental characterization of coatings on ceramics: a case study of tungsten on SiC*, Surf. Coat. Technol. 367 (2019) 1–10.
- [25] N. Schalk, M. Tkadletz, V. L. Terziyska, M. Deluca, I. Letofsky-Papst, J. Keckes, C. Mitterer, *Evolution of microstructure and mechanical properties of a graded TiAlON thin film investigated by cross-sectional characterization techniques*, Surf. Coat. Technol. 359 (2019) 155–161.
- [26] H. Holzschuh, *Deposition of Ti–B–N (single and multilayer) and Zr–B–N coatings by chemical vapor deposition techniques on cutting tools*, Thin Solid Films 469 (2004) 92–98.
- [27] J. Kieffer, D. Karkoulis, *PyFAI, a versatile library for azimuthal regrouping*, J. Phys. Conf. Ser. 425 (20) (2013) 202012.
- [28] T. T. Hassel Ledbetter, *Elastic-stiffness coefficients of titanium diboride*, J. Res. Natl. Inst. Stand. Technol. 114 (6) (2009) 333–339.
- [29] M. Stefenelli, J. Todt, A. Riedl, W. Ecker, T. Müller, R. Daniel, M. Burghammer, J. Keckes, *X-ray analysis of residual stress gradients in TiN coatings by a Laplace space approach and cross-sectional nanodiffraction: a critical comparison*, J. Appl. Crystallogr. 46 (5) (2013) 1378–1385.
- [30] J. Keckes, M. Bartosik, R. Daniel, C. Mitterer, G. Maier, W. Ecker, J. Vila-Comamala, C. David, S. Schoeder, M. Burghammer, *X-ray nanodiffraction reveals strain and microstructure evolution in nanocrystalline thin films*, Scr. Mater. 67 (9) (2012) 748–751.
- [31] J. Keckes, R. Daniel, J. Todt, J. Zalesak, B. Sartory, S. Braun, J. Gluch, M. Rosenthal, M. Burghammer, C. Mitterer, S. Niese, A. Kubec, *30 nm X-ray focusing correlates oscillatory stress, texture and structural defect gradients across multilayered TiN–SiO_x thin film*, Acta Mater. 144 (2018) 862–873.
- [32] K. Matoy, H. Schönherr, T. Detzel, T. Schöberl, R. Pippan, C. Motz, G. Dehm, *A comparative micro-cantilever study of the mechanical behavior of silicon based passivation films*, Thin Solid Films 518 (1) (2009) 247–256.
- [33] R. A. Andrievskii, Y. M. Shul’ga, L. S. Volkova, I. I. Korobov, N. N. Dremova, E. N. Kabachkov, G. V. Kalinnikov, S. P. Shilkin, *Oxidation behavior of TiB₂ micro- and nanoparticles*, Inorg. Mater. 52 (7) (2016) 686–693.

- [34] T. S. R. C. Murthy, R. Balasubramaniam, B. Basu, A.K. Suri, M. N. Mungole, *Oxidation of monolithic TiB₂ and TiB₂-20 wt.% MoSi₂ composite at 850°C*, J. Eur. Ceram. Soc. 26 (1) (2006) 187–192.
- [35] A. Kulpa, T. Troczynski, *Oxidation of TiB₂ powders below 900°C*, J. Am. Ceram. Soc. 79 (2) (1996) 518–520.
- [36] D. Mao, Y. Xu, L. Dong, J. Wu, M. Zhao, D. Li, *Optimization of the oxidation behavior and mechanical properties by designing the TiB₂/ZrO₂ multilayers*, Coatings 9 (10) (2019) 600.
- [37] C. Pfohl, A. Bulak, K. T. Rie, *Development of titanium diboride coatings deposited by PACVD*, Surf. Coat. Technol. 131 (1) (2000) 141–146.
- [38] C. M. T. Sanchez, B. R. Plata, M. E. H. M. da Costa, F. L. Freire Jr., *Titanium diboride thin films produced by dc-magnetron sputtering: structural and mechanical properties*, Surf. Coat. Technol. 205 (12) (2011) 3698–3702.
- [39] M. Berger, M. Larsson, *Mechanical properties of multilayer pvd Ti/TiB₂ coatings*, Surf. Eng. 16 (2) (2013) 122–126.
- [40] C. Kainz, N. Schalk, M. Tkadletz, C. Mitterer, C. Czettel, *Microstructure and mechanical properties of CVD TiN/TiBN multilayer coatings*, Surf. Coat. Technol. 370 (2019) 311–319.
- [41] C. Kainz, N. Schalk, M. Tkadletz, C. Mitterer, C. Czettel, *The effect of B and C addition on microstructure and mechanical properties of TiN hard coatings grown by chemical vapor deposition*, Thin Solid Films 688 (2019) 137283.
- [42] C. Kainz, N. Schalk, M. Tkadletz, C. Saringer, M. Winkler, A. Stark, N. Schell, J. Julin, C. Czettel, *Thermo-physical properties of coatings in the Ti(B,N) system grown by chemical vapor deposition*, Surf. Coat. Technol. 384 (2020) 125318.

*Gradients of microstructure, stresses and mechanical properties in a multilayered diamond thin film revealed by correlative cross-sectional nano-analytics**

David P. GRUBER ^{a,b}, Juraj TODT ^b, Nicolas WÖHRL ^c, Jakub ZALESK ^b, Michael TKADLETZ ^d, Adam KUBEC ^e, Sven NIESE ^f, Manfred BURGHAMMER ^g, Martin ROSENTHAL ^g, Hadwig STERNSCHULTE ^h, Manuel J. PFEIFENBERGER ^b, Bernhard SARTORY ⁱ and Jozef KECKES ^{a,b}

Abstract

THIN DIAMOND FILMS deposited by chemical vapour deposition (CVD) usually feature cross-sectional gradients of microstructure, residual stress and mechanical properties, which decisively influence their functional properties. This work introduces a novel correlative cross-sectional nano-analytics approach, which is applied to a multi-layered CVD diamond film grown using microwave plasma-enhanced CVD and consisting of a $\sim 8 \mu\text{m}$ thick nanocrystalline (NCD) base and a $\sim 14.5 \mu\text{m}$ thick polycrystalline (PCD) top diamond sublayer. Complementary cross-sectional 30 nm beam synchrotron X-ray diffraction, depth-resolved micro-cantilever and hardness testing and electron microscopy analyses reveal correlations between microstructure, residual stress and mechanical properties. The NCD sublayer exhibits a $1.5 \mu\text{m}$ thick isotropic nucleation region with the highest stresses of $\sim 1.3 \text{ GPa}$ and defect-rich nanocrystallites. With increasing sublayer thickness, a (110) fibre texture evolves gradually, accompanied by an increase in crystallite size and a decrease in stress. At the NCD/PCD sublayer interface, texture, stresses and crystallite size change abruptly and the PCD sublayer exhibits the presence of Zone T competitive grain growth microstructure. NCD and PCD sublayers differ in fracture stresses of $\sim 14 \text{ GPa}$ and $\sim 31 \text{ GPa}$, respectively, as well as in elastic moduli and hardness, which are correlated with their particular microstructures. In summary, the introduced nano-analytics approach provides complex correlations between microstructure, stresses, functional properties and deposition conditions.

* This piece of research was first published in *Carbon* vol. 144 (April 2019) pp. 666–674, DOI: 10.1016/j.carbon.2018.12.093.

The version presented here features marginal stylistic and typographical corrections.

a Department of Materials Physics, Montanuniversität Leoben, Leoben, Austria

b Erich Schmid Institute for Materials Science, Austrian Academy of Sciences, Leoben, Austria

c Faculty of Physics and CENIDE, University of Duisburg-Essen, Germany

d Department of Physical Metallurgy and Materials Testing, Montanuniversität Leoben, Leoben, Austria

e Fraunhofer IWS, Dresden, Germany; now at Paul Scherrer Institute, Villigen-PSI, Switzerland

f AXO DRESDEN GmbH, Dresden, Germany

g European Synchrotron Radiation Facility, Grenoble, France

h Fakultät für Allgemeinwissenschaften, Hochschule Augsburg, Augsburg, Germany

i Materials Center Leoben Forschung GmbH, Leoben, Austria

Introduction

DUE TO THEIR outstanding electronic, chemical, thermal, mechanical and biocompatible properties, diamond thin films have attracted significant scientific and technological attention in the last decades [1, 2]. Polycrystalline diamond thin films produced by low-pressure chemical vapour deposition (CVD) nowadays represent one of the most common applications of synthetic diamond [3, 4]. During the CVD process, a complex cross-sectional microstructure is usually formed in a sequence of growth stages including nucleation, coalescence and a final growth stage [2, 5–10]. In addition, during both the growth process and the subsequent cooling down to room temperature, (intrinsic) growth and (extrinsic) thermal stresses accumulate in the films as a result of the gradual microstructural evolution and the mismatch of coefficients of thermal expansion (CTEs) between the film and substrate, respectively [11–20]. The gradients of intrinsic stress can be very pronounced as a result of the gradual microstructure evolution, which may include an evolutionary selection of distinct crystallographic orientations, the development of columnar grain morphology, incorporation of non-diamond phases at grain boundaries, porosity, coalescence of grains, and/or the formation of twins and stacking faults [8, 13, 15]. Mechanical properties of CVD diamond thin films are strongly dependent on grain size, where, with increasing grain size, Young's moduli \sim (400–1200 GPa) and hardness \sim (40–110 GPa) tend to increase to a certain extent, whereas fracture stress \sim (1–9 GPa) decreases [21–27]. The grain size also influences the surface roughness of the films and, in nanocrystalline diamond (NCD), smoother film surfaces occur due to the fact, that (i) surface roughness is decoupled from film thickness and (ii) better film homogeneity as well as isotropic material properties, compared to polycrystalline diamond (PCD), are present [4, 26], [28]. The characterisation of mechanical properties of CVD diamond thin films has, however, been performed mainly by using indentation techniques [26, 29, 30], and three and four-point bending tests [31, 32], which provide primarily surface and/or volume-average properties.

In contrast, the functional properties of CVD diamond films depend decisively on the cross-sectional gradients of microstructure and residual stress [15, 26]. For example, residual stress gradients in CVD diamond films may induce unwanted bending of the film, when removed from the underlying substrate, *e.g.* to be applied in microelectromechanical systems. Therefore, the understanding of the correlation between cross-sectional microstructure and residual stress gradients on one side, and overall as well as depth-dependent mechanical properties on the other side, is of significant importance for the successful application of CVD diamond thin films. The aim of this work is (i) to introduce a novel concept for the analysis of gradient CVD diamond thin films based on correlative cross-sectional nanoanalytics including 30 nm cross-sectional X-ray nano-diffraction (CSNANOXRD) in conjunction with depth-resolved micromechanical

testing and (ii) to discuss the correlation between gradients of microstructure, residual stress and mechanical properties in a model multi-layered CVD diamond film consisting of a NCD base and a PCD top sublayer. The novel nano-analytics approach opens new possibilities for the understanding of the correlation between (i) applied time-dependent process conditions, (ii) cross-sectional depth-dependent gradients of microstructure, residual stress and mechanical properties and (iii) overall functional properties of diamond thin films.

Experimental

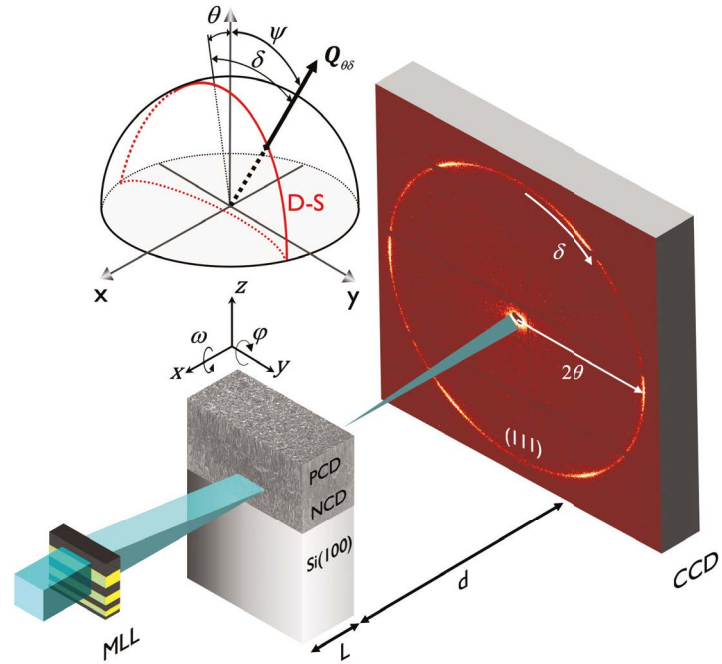
Deposition of NCD/PCD diamond thin film

The diamond film was deposited by a microwave plasma-enhanced chemical vapour deposition (MPECVD) method (using a 2.45 GHz *Iplas Cyrannus I* plasma source) on a Si(100) wafer with a thickness of 425 μm . Prior to the deposition, the substrate was ultrasonically treated for 30 min with an abrasive solution consisting of diamond powder (20 nm grain size), Ti powder (5 nm particle size), and ethanol in a weight percent ratio of 1:1:100 (wt%). In a next step, the substrate was first ultrasonically cleaned for 15 min in acetone to remove any residue of the abrasive solution from the surface before the plasma cleaning was performed. Finally, the multi-layered 22.5 μm thick film consisting of 8 and 14.5 μm thick NCD and PCD sublayers, respectively, was deposited. The main process parameters are summarised in Tab. 1.

Substrate cleaning prior to the deposition	30 min in an Ar/H ₂ plasma at 200 mbar with a microwave power of 1 kW (390 sccm Ar, 10 sccm H ₂) at ~800°C
Deposition temperature for NCD and PCD sublayers	800 and 900°C
Deposition pressure	200 mbar
Microwave power	1 kW
Precursors for NCD	H ₂ /CH ₄ (384 sccm H ₂ , 16 sccm CH ₄)
Precursors for PCD	Ar/H ₂ /CH ₄ plasma (386 sccm Ar, 10 sccm H ₂ , 4 sccm CH ₄)
Deposition time	5 h for each sublayer

TABLE 1: Summary of parameters used for the deposition of NCD and PCD sublayers on Si(100) substrate.

FIGURE 1: A schematic drawing of the CSnanoXRD set-up at the ID13 beam-line of ESRF in Grenoble. The experiment was performed in transmission diffraction geometry using one MLL to focus the synchrotron pencil X-ray beam (with $E = 13$ keV) to a cross-section of $15 \mu\text{m} \times 30$ nm. The sample lamella with a thickness L of $\sim 100 \mu\text{m}$ comprising the multi-layered NDC/PCD thin film on Si(100) was scanned along the z direction in equidistant steps of 25 nm while the diffraction signal was recorded at every sample position by the 2D detector (Eiger X 4M) at a sample-to-detector distance d of ~ 125 mm. The azimuthal angle d is counted from the 12 o'clock detector position and defined in clockwise direction as indicated on the detector plane schematically.



Synchrotron CSnanoXRD characterisation

A thin lamella with dimensions of $\sim (3 \times 0.5) \text{ mm}^2$ and a thickness L of $\sim 100 \mu\text{m}$ (in the X-ray beam direction, cf. Fig. 1) was prepared by mechanical thinning from the NDC/PCD film on Si(100). The sample was investigated by CSnanoXRD [33,34], at the ID13 nano-focus beam-line of the European Synchrotron Radiation Facility in Grenoble, France. The experiment was performed in transmission geometry, using a pencil X-ray beam focussed by a Multi-layer Laue lens (MLL) to cross-sectional dimensions of $\sim 15 \mu\text{m} \times 30$ nm [34] and a photon energy of 13 keV (Fig. 1). The sample was moved in the X-ray beam with a constant step size of ~ 25 nm along the film normal direction using a piezo-actuated stage while the diffraction signal was recorded using a two-dimensional (2D) charged-coupled device detector (CCD) Eiger X 4M featuring a pixel size of 75×75 μm^2 . To calibrate the powder diffraction experimental geometry, a NIST LaB₆ standard powder was measured at the same sample-to-detector distance as the diamond film sample. The collected Debye-Scherrer (DS) rings from the NIST sample were used to calibrate the sample-to-detector distance of 124.71 mm, the tilt angle of the detector plane of 0.85° and the rotation angle of the tilt plane of 152.42° , as well as the beam centre on the detector at 969.4 and 1182.8 pixels (in horizontal and vertical directions). The DS rings collected from the diamond sample were processed using the Python package *pyFAI* [35]. Due to the relation of sample-to-detector distance to photon energy, there was only one diamond 111 DS ring visible on the detector, but a high strain sensitivity was ensured by this chosen geometry (Fig. 1). The data were used to generate plots of (i) intensity distribution $I_{111}(q, z)$

as a function of Bragg's angle q and the sample depth z (denoted henceforth as *phase plot*), (ii) intensity distribution $I_{111}(d, z)$ as a function of the DS ring azimuthal angle d and the sample depth z (denoted further as *texture plot*) and (iii) to evaluate depth gradients of in-plane X-ray elastic strains $\varepsilon_{111}(z)$ for the diamond 111 reflection. In order to calculate residual stresses $\sigma(z)$ from the measured strains, the Hill grain interaction model was used for simplicity, with an X-ray elastic constant $0.5 S_2$ of $9.38 \times 10^{-9} \text{ Pa}^{-1}$. In order to correct the evaluated strain and stress values for the stress relaxation caused by the lamella preparation, a dedicated procedure based on a finite element model was applied [36]. Other details of the experimental approach and evaluation procedure can be found elsewhere [34,36].

Electron microscopy analysis

Scanning electron microscopy (SEM) analysis, electron backscatter diffraction (EBSD) and focused ion beam (FIB) machining/polishing on the NCD/PCD thin film cross-section was performed using a *Zeiss Auriga CrossBeam* workstation. To obtain information on the film cross-sectional morphology, the cross-section was first polished by Ga ions by FIB within a $20 \mu\text{m}$ wide region followed by a final polishing step at a beam current of $\sim 100 \text{ pA}$ and an accelerating voltage of $\sim 5 \text{ kV}$ and under an angle of $\sim 15^\circ$ in order to achieve maximum smoothness and to remove residual impurities from previous coarser FIB milling. The EBSD characterisation with a lateral step of 50 nm was carried out with an *Ametek-EDAX Hikari Super* camera at an accelerating voltage of 20 kV and using a beam current of 6 nA , directly after the fine polishing in order to prevent contamination of the cross-section.

Hardness characterisation

The hardness of the individual sublayers was evaluated by nanoindentation, using a *Hysitron TI950 Triboindenter* on the same cross-section of the film that was prepared by FIB for the EBSD analysis. Ten indentation measurements were performed on the PCD and NCD sublayer cross-sections, approximately in the middle of each sublayer, and (for reference purposes) also on the underlying substrate. The measurements were carried out using a diamond Berkovich tip under quasi-static loading conditions, applying a maximum load of $\sim 13 \text{ mN}$. They resulted in effective contact depths of $\sim 60 \text{ nm}$ for PCD and $\sim 70 \text{ nm}$ for NCD. The area function of the indenter tip was determined by reference measurements on fused silica. Recorded load-displacement data were evaluated according to the Oliver-Pharr method [37]. The hardness values (and corresponding standard errors) presented in Sec. 3 were calculated as the arithmetic mean of the results obtained from the ten individual measurements.

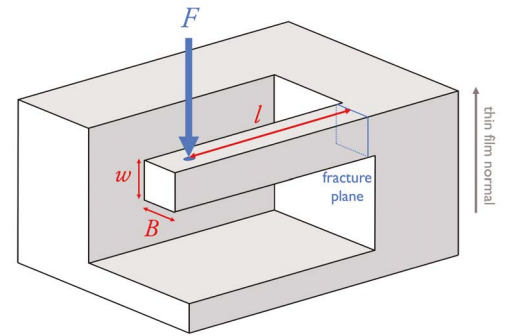


FIGURE 2: A schematic drawing of the employed micro-cantilever specimen geometry indicating width B and thickness w . The bending length l is the distance between the point of the applied load F and the resulting fracture plane.

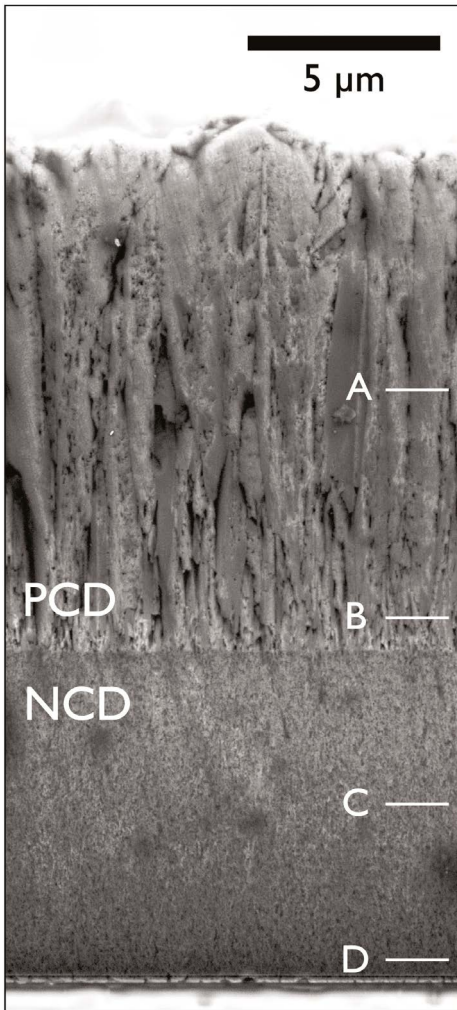


FIGURE 3: SEM micrograph showing the cross-sectional morphology of the fine- and coarse-grained NCD and PCD sublayers, respectively. The markers at the cross-sectional positions A–D correspond approximately to the cSnanoxRD measurement positions, at which the DS rings in Fig. 5a were collected.

Micromechanical tests

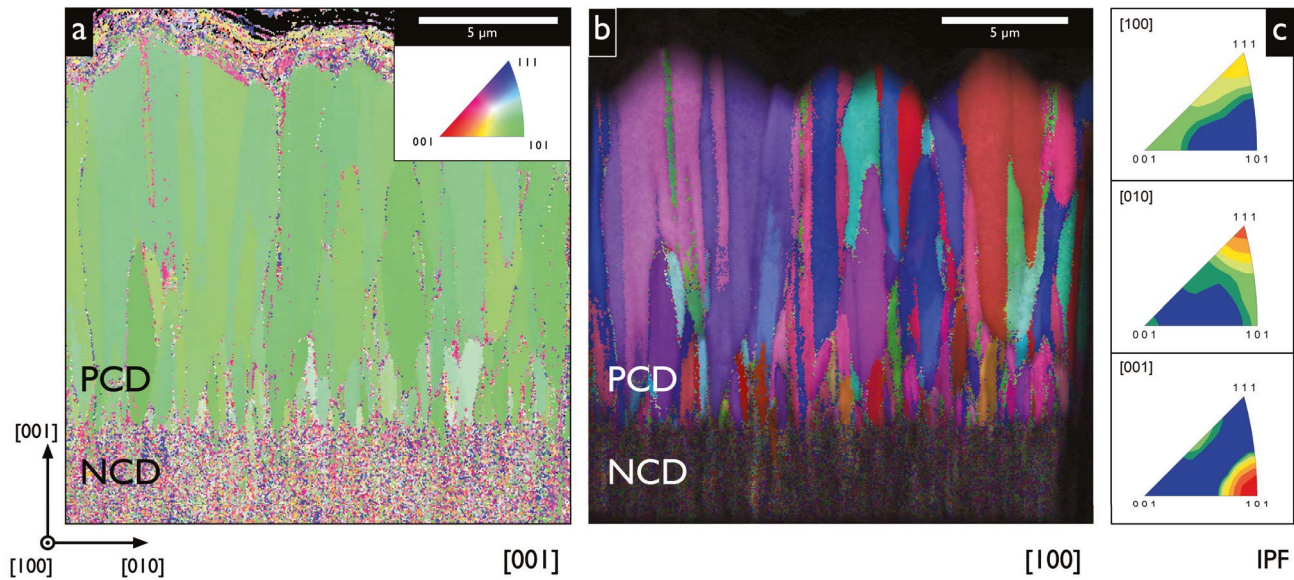
In order to determine elastic moduli and fracture stresses of the CVD diamond multi-layer film, in-situ testing of micro-cantilevers and an evaluation procedure based on the classical linear-elastic theory of fracture mechanics were employed [39]. Eight micro-cantilevers with dimensions of $\sim(1.4 \times 1.4 \times 12) \text{ mm}^3$ each were fabricated from the individual sublayers of the CVD diamond film using a FIB workstation (*Zeiss Auriga CrossBeam*) (Fig. 2). Four cantilevers made from the coarse-grained top PCD sublayer were positioned about $2 \mu\text{m}$ beneath the sublayer surface. In order to access the NCD layer and to avoid the long FIB milling times, a large portion of PCD sublayer with a volume of $\sim(200 \times 15 \times 30) \text{ mm}^3$ was removed using a femtosecond laser unit (*Origami 10 XP*) installed in the FIB workstation prior to the FIB machining. Four cantilevers were then milled approximately from the centre of the NCD sublayer. Details on the laser milling approach can be found in Ref. [38]. The FIB fabrication was performed using an acceleration voltage of $\sim 30 \text{ kV}$ and beam currents in the range from 20 nA to 50 pA . Special care was taken to avoid sample damage by Ga ions by using low FIB cutting currents at final cantilever machining steps. All un-notched cantilever specimens were loaded and load-deflection curves were acquired. Micromechanical testing was carried out in in-situ configuration in a SEM (*Zeiss LEO 982*) by means of a dedicated indenter system (*Hysitron Pi-85 PicoIndenter*), featuring a piezo-actuated sample stage. The cantilevers were loaded using a sphero-conical diamond indenter tip (with a radius of curvature of $\sim 700 \text{ nm}$) in out-of-plane direction up to the load of fracture (Fig. 2). Testing was carried out at a constant displacement rate of $\sim 20 \text{ nm s}^{-1}$ in order to ensure quasi-static loading conditions. Special care was taken to load the cantilevers in their central planes to avoid torque. The load-deflection curves as well as the applied force were recorded and subsequently used to calculate Young's moduli.

Based on the recorded load-deflection data, fracture stress σ_s was evaluated as follows

$$\sigma_s = 6 \frac{Fl}{Bw^2},$$

where F represents the maximum applied load at fracture, l is the bending length representing the distance between the point of the applied force and the resulting fracture plane, and B and w represent the cantilever width and thickness, respectively (Fig. 2). The evaluation of Young's modulus E rests on the assumption of an ideally brittle material, excluding plastic deformation effects of the tested material in contact with the indenter tip. The recorded dominant elastic response from cantilever loading is thus used to calculate E according to

$$E = \frac{4F}{\delta B} \times \left(\frac{l}{w}\right)^3,$$



δ being the displacement at maximum applied load F [39].

Results and discussion

Cross-sectional thin film morphology

The SEM micrograph from the NCD/PCD film fracture cross-section in Fig. 3 reveals a distinct two-layer architecture, with a very fine microstructure of the NCD base sublayer compared to the coarse-grained microstructure with prominent elongated columnar grains of the PCD sublayer. The interface between the sublayers is relatively sharp and flat, indicating small surface roughness of the NCD sublayer surface caused by its nanocrystalline nature. Measurements in the SEM on multiple fracture surfaces and cross-sections indicated an almost uniform film thickness of $\sim 8 \mu\text{m}$ for NCD and $\sim 14.5 \mu\text{m}$ for PCD sublayers. The cross-sectional microstructure, grain morphology and crystallographic orientation of the grains were mapped by EBSD using a lateral step size of 50 nm. Fig. 4a presents an orientation map of the thin film cross-section for the film normal direction [001], while Fig. 4b shows an orientation map for the film in-plane direction [100]. The results document that the EBSD characterisation succeeded in determining the preferred orientation of the crystallites within the PCD sublayer only, indicating a $\langle 110 \rangle$ fibre texture. Additionally, the EBSD data from the PCD sublayer were used to generate three inverse pole figures for three perpendicular sample axes [100], [010] and [001], which correlate with two thin film in-plane (perpendicular and parallel to the micrograph plane) and one out-of-plane directions, respectively. The inverse pole figures (Fig. 4c) document, once more, the 110 fibre texture as well as a relatively

FIGURE 4: EBSD [001] (a) and [100] (b) inverse pole figure (IPF) maps from a $20 \times 20 \text{ mm}^2$ cross-section of the NCD/PCD film indicating a columnar morphology of the microscopic diamond grains exhibiting a competitive grain growth mode in the PCD sublayer. The strip of noisy signal on top of the PCD films is artefacts stemming from the uneven sample surface. Crystallite size in NCD was below the resolution limit of the EBSD analysis. (c) EBSD [100], [010] and [001] inverse pole figures obtained from the data collected from the PCD sublayer, indicating the $\langle 110 \rangle$ fibre texture.

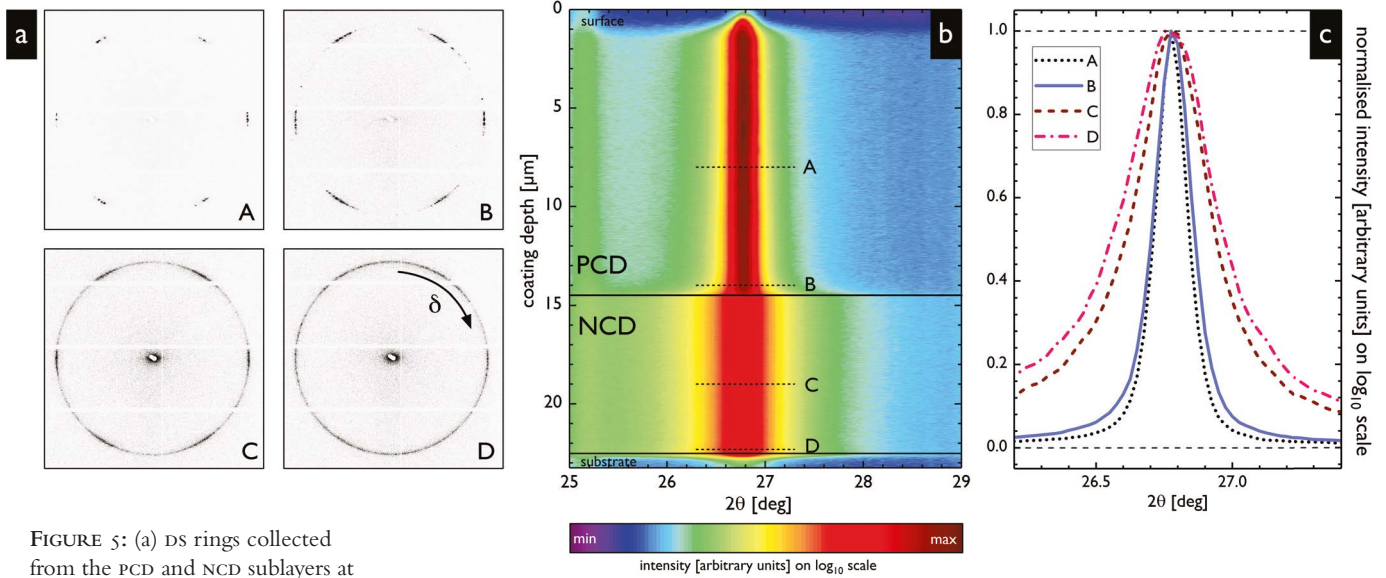


FIGURE 5: (a) DS rings collected from the PCD and NCD sublayers at the cross-sectional positions A–D (*cf.* Fig. 3) indicate a variation of texture across the film. (b) Phase plot $I_{111}(d, z)$ obtained by azimuthal integration of about 950 DS rings in the δ range of 80–100°.

(c) Normalised intensity distributions of exemplary diamond 111 reflections, representing diffraction on diamond {111} crystallographic planes oriented perpendicular to the substrate surface, collected at positions A–D.

regular in-plane orientation of crystallites with {111} planes oriented approximately perpendicular to the substrate surface. The EBSD data (Fig. 4) together with the SEM micrograph from Fig. 3 indicate the presence of a Zone T type mechanism of competitive grain growth within the PCD sublayer. One can observe the columnar grain growth with selected grains stretching from the nucleation zone at the NCD/PCD interface to the film surface, whereas some other, smaller, grains close to the nucleation zone of the PCD sublayer cease to grow further after ~ 1 to $5 \mu\text{m}$. In the case of the NCD sublayer, however, the EBSD approach failed to reveal the microstructure and preferred orientation of the nanocrystals, which is also apparent from Fig. 4b, where the NCD sublayer is entirely covered by the dark EBSD image quality. There, the low-quality EBSD signal can be explained by the small grain size of the crystallites of $\sim 20 \text{ nm}$ (*cf.* Sec. 3.2), which was close to, or somewhat below the resolution limit of the EBSD system.

Synchrotron CSnanoXRD analysis

In Fig. 5a, four representative diamond 111 DS rings from the centre, the nucleation region of the PCD sublayer, as well as from the centre of the NCD sublayer and the corresponding nucleation region are presented (*cf.* also Fig. 3). They indicate a variation in texture across the film's thickness. In the NCD sublayer, the DS ring collected at position D (Fig. 5a) exhibits a relatively homogeneous azimuthal intensity distribution (nearly random texture), whereas azimuthal maxima at $\delta = 30^\circ$ and 90° can be identified in the DS ring collected at position C. In the PCD sublayer, the azimuthal maxima of the DS rings taken at positions B and A become very pronounced. About 950 DS rings collected from the thin film cross-section were used to generate cross-sectional phase and texture plots $I_{111}(q, z)$ and

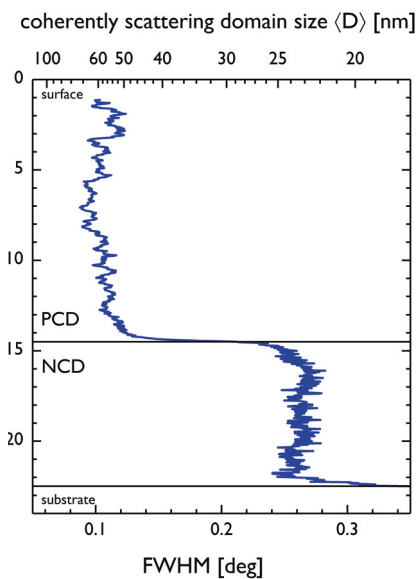


FIGURE 6: Cross-sectional evolution of FWHM of the diamond 111 reflection evaluated from DS rings for $\delta = 90^\circ$, corresponding to the in-plane orientation of the diffraction vectors, and the linked in-plane size of coherently scattering domains D obtained from Scherrer's equation.

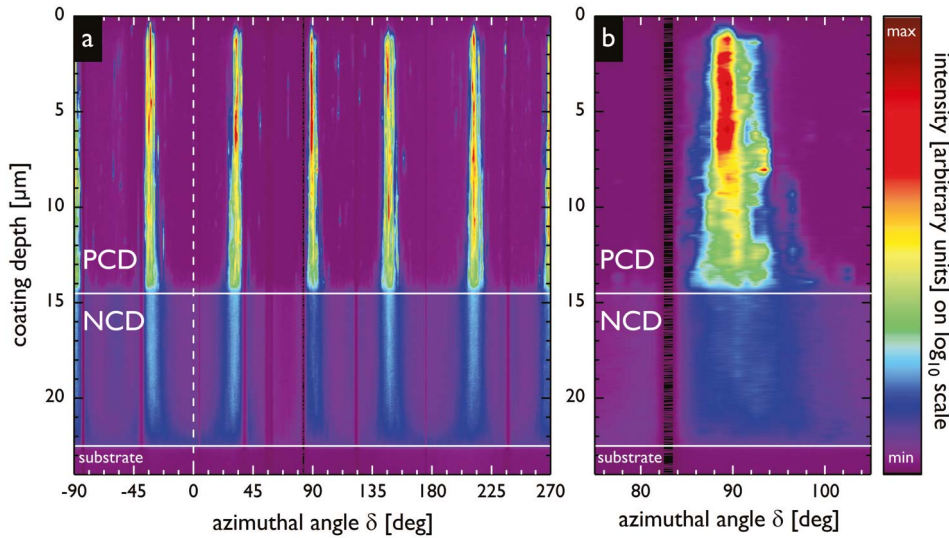


FIGURE 7: Texture plot $I_{111}(d, z)$ obtained by radial integration of approximately 950 DS rings showing the cross-sectional texture evolution for the entire azimuthal range (a), and for a selected azimuthal range around 90° (b)

$I_{111}(d, z)$, presented in Figs. 5b and 7, respectively. The phase plot in Fig. 5b obtained by the azimuthal integration in the δ range of 80 – 100° reveals an evolution of the diamond 111 reflection shape as a function of the film depth. In Fig. 5c, four representative diamond 111 reflections collected at the respective positions A–D (Figs. 3 and 5a) for the diffraction vector oriented approximately parallel to the substrate surface, are shown. In the NCD sublayer, the 111 reflections are broad and asymmetric with a shoulder at smaller diffraction angles, while in the PCD sublayer they become narrower. The phase plot (Fig. 5b) and the peak profiles corresponding to positions C and D from Fig. 5c with their asymmetric 111 reflection can be interpreted by the nanocrystalline and defect-rich nature of the NCD sublayer crystallites with a high stacking fault density. In contrast, the phase plot and the relatively narrow and symmetric line profiles corresponding to positions A and B from Fig. 5b and c indicate the presence of relatively large crystallites in the PCD sublayer. The evolution of the XRD peak broadening was evaluated for all ~ 950 diamond 111 reflections for the in-plane orientation of the diffraction vector and is presented as full width at half maximum (FWHM) in Fig. 6. FWHM is usually sensitive to the size of coherently diffracting domains D and to the presence of crystal defects, resulting in the formation of strains of II and III order. The FWHM data from Fig. 6 are shown together with the D obtained by Scherrer's equation $D \sim \lambda / (FWHM \cos \vartheta)$, using the beam wavelength $\lambda = 0.9537 \text{ \AA}$ and neglecting strain-induced broadening for the sake of simplicity. The results indicate that the in-plane crystallite size is smallest in the NCD sublayer at the interface to Si(100), reaching values below 20 nm , then increases to $\sim 24 \text{ nm}$ within the $1.5 \mu\text{m}$ thick nucleation layer before saturating and remaining relatively unchanged. Within the PCD sublayer, the average in-plane crystallite size increases from about 40 nm to 60 nm and remains constant across the entire sublayer. The texture plot $I_{111}(d, z)$ in Fig. 7 shows the gradual evolution

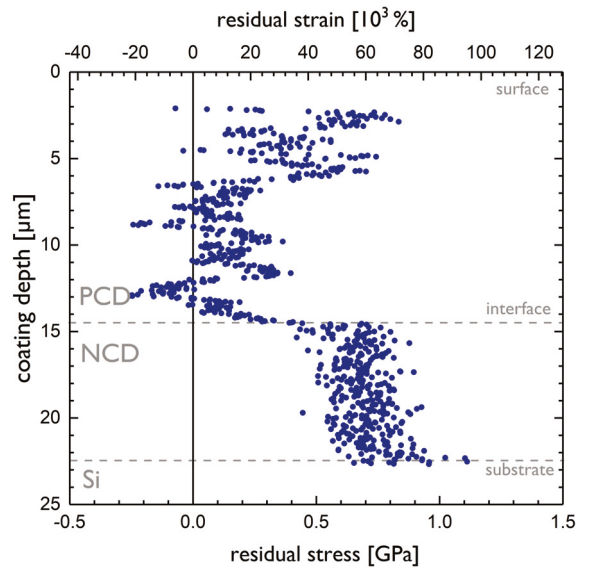
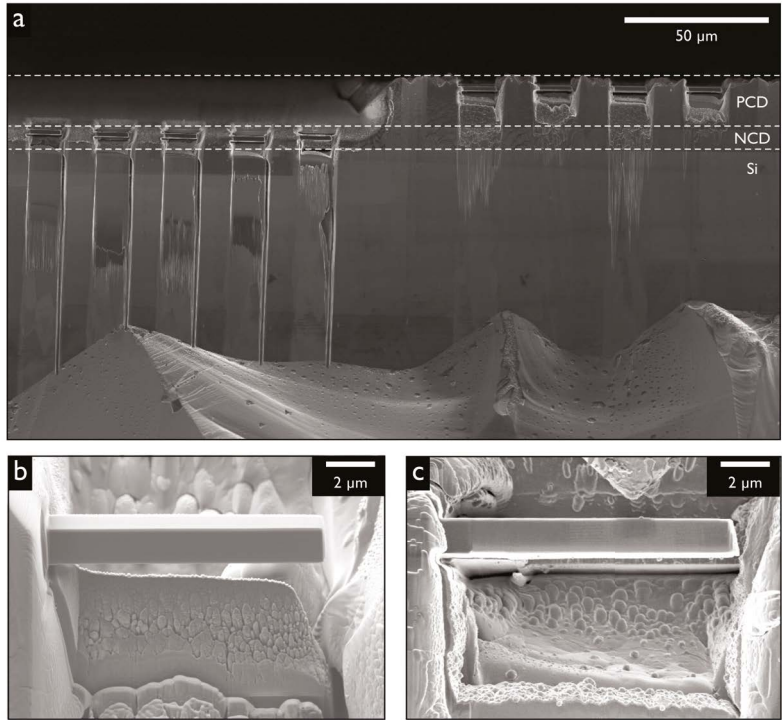


FIGURE 8: Gradient of residual stress and X-ray elastic strains $\varepsilon_{111}(z)$ across the film depth determined using csnanoxrd

FIGURE 9: SEM micrographs of five (four plus one specimen for pre-testing) and four micro-cantilevers machined from the NCD and PCD sublayers (a) together with the magnified micrographs of representative cantilevers from PCD (b) and NCD (c) sublayers. The approaching sphero-conical diamond indenter tip is visible in the upper part of micrograph (c).



of texture across the film's cross-section. At the interface to the Si(100) substrate, the crystallites are oriented randomly in the NCD sublayer (*cf.* also Fig. 5a). Starting at a thickness of $\sim 1.5 \mu\text{m}$, the $\langle 110 \rangle$ fibre texture starts to evolve within the NCD sublayer and becomes sharper towards the NCD/PCD interface. Across the PCD sublayer, the 110 texture is also becoming stronger towards the surface, due to the mechanism of competitive columnar grain growth discussed in Sec. 3.1. One important feature of the $\langle 110 \rangle$ fibre texture is the presence of distinct azimuthal maxima at $\delta = 90^\circ$ and 180° , which represent the diffraction on $\{111\}$ crystallographic planes oriented approximately perpendicular to the substrate surface, with diffraction vectors oriented parallel to the surface. The CSnanoxRD data are in agreement with the EBSD data (Fig. 4), confirming the texture type for the PCD sublayer and complementing the missing data for the NCD sublayer. CSnanoxRD was employed to evaluate gradients of X-ray elastic strain $\varepsilon_{111}(z)$ and in-plane biaxial residual stress across the film thickness. The acquired strains and stresses presented in Fig. 8 document the presence of complex gradients. The highest stress of $\sim 1.1 \text{ GPa}$ was observed in the NCD sublayer at the interface to the Si(100) substrate. Within the NCD sublayer nucleation region, these

TABLE 2: Mechanical properties of the NCD and PCD sublayers evaluated by bending experiments on micro-cantilevers and cross-sectional indentation tests.

	Fracture stress [GPa]	Young's modulus [GPa]	Hardness [GPa]
PCD	31.6 ± 6.6	1037 ± 25.3	60.8 ± 0.9
NCD	14.3 ± 0.6	903 ± 35.3	46.5 ± 1.7

tensile stresses were observed to drop rapidly to about 750 MPa, and then found to decrease linearly towards the NCD/PCD sublayer interface, where the stress state switches to compressive. Across the PCD sublayer, the stress state changes very locally and overall becomes tensile again towards the surface. These abrupt changes in stress within the PCD sublayer can be attributed to the coarse-grained nature of this sublayer as well as varying stress states within individual grains. It is obvious that the observed stress variation across the diamond thin film cross-section can be correlated with intrinsic stress changes caused by the complex microstructure evolution (*cf.* Sec. 4).

Cross-sectional mechanical properties of the sublayers

In Fig. 9a, SEM micrographs of micro-cantilevers machined using FIB from the NCD (four specimens plus one pre-test) and PCD (four specimens) sublayers are presented together with the micrographs of two representative cantilever specimens in Fig. 9b and c, respectively. The load-deflection curves recorded during the bending experiments on both types of cantilevers presented in Fig. 10 show linear elastic behaviour, *i.e.* the cantilevers behaved like an ideal bending beam and broke without detectable plastic and/or ductile response [39]. The data set of one micro-cantilever from the PCD sublayer showed unrealistic load-deflection characteristics. It was treated as an outlier, disregarded from further evaluation and is not shown in Fig. 10. The distinct differences in the slopes and in the (maximum) loads at fracture between the curves from the NCD and PCD type cantilevers (Fig. 10) qualitatively indicate the differences in the mechanical properties of the sublayers. The recorded micromechanical data from the cantilevers were used to evaluate fracture stresses and Young's moduli (*cf.* Sec. 2), of which the mean averages are presented in Tab. 2. The quantitative data document a difference of $\sim 10\%$ in the Young's moduli and a significant difference in the fracture stresses between the sublayers, which are both discussed in Sec. 4. In addition, the hardness of the NCD and PCD sublayers was determined by means of nanoindentation performed on the sublayers' cross-sections. In Fig. 11, thirty load-displacement responses are presented, ten from each of the NCD and PCD sublayers' as well as the underlying Si substrate's cross-sections. Again, the differences between the slopes and the maximal penetration depths (Fig. 11) indicate qualitative differences in the mechanical properties of both sublayers. The recorded indentation data were used to determine the hardness of the sublayers presented in Tab. 2.

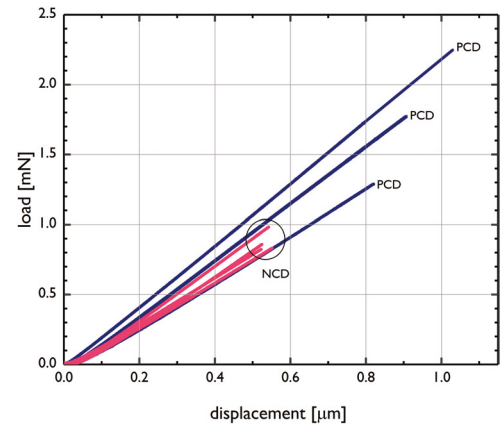


FIGURE 10: Load-deflection curves recorded during bending experiments on micro-cantilevers (Fig. 9) machined from the NCD and PCD sublayers, indicating the comparatively smaller Young's modulus and fracture stress of the NCD sublayer.

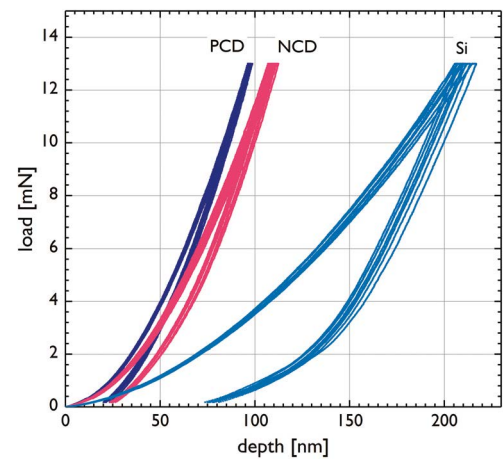


FIGURE 11: Load-displacement curves recorded during cross-sectional indentation experiments on the NCD and PCD sublayers, indicating the smaller Young's modulus and hardness of the NCD sublayer. The response of the Si substrate is shown for reference.

Discussion of cross-sectional correlations

As discussed in Sec. 1, the physical properties of CVD diamond thin films depend on cross-sectional microstructure and stress gradients, which evolve as a function of the deposition conditions, in particular as a result of the applied process parameters as well as of a variety of self-organisation phenomena taking place at distinct stages of the growth process. In this section, the correlations between (i) the observed phenomena and (ii) the methodological aspects of the applied correlative cross-sectional nano-analytics approach will be discussed. Electron microscopy and diffraction (SEM, EBSD) as well as CSnanoxRD (Figs. 3, 5–8) revealed the presence of a nanocrystalline nucleation region in the NCD sublayer with a thickness of $\sim 1.5 \mu\text{m}$, possessing the highest tensile stress of $\sim 1.1 \text{ GPa}$ at the interface to Si(100) and showing the smallest apparent in-plane crystallite size D of $\sim 18 \text{ nm}$ and random texture. This observation is in agreement with the model of Silva et al. [8], where it was proposed that the growth of ballas-like crystallites composed of nanometric sectors elongated along the $[110]$ axes results in the formation of a $\langle 110 \rangle$ fibre texture. At a thicknesses of $\sim 1.5\text{--}8 \mu\text{m}$, both microstructure and stress evolution become saturated within the NCD sublayer as a result of steady state grain growth conditions, resulting in a tensile stress level of 0.75 GPa and a crystallite size D of $\sim 24 \text{ nm}$, while the $\langle 110 \rangle$ texture sharpness changes only marginally. The presence of the near-substrate transition region with random nucleation texture lacking significant growth competition in the early growth stage correlates with the experimental results and texture models reported from other thin monolithic films [5, 7, 8]. It is, however, interesting to observe that the transition from the nucleation regime during the NCD sublayer formation occurs very abruptly. EM and CSnanoxRD (Figs. 3–8) also revealed the presence of a transition region with a thickness of $\sim 2 \mu\text{m}$ within the PCD sublayer. At a total film thickness of $\sim 8\text{--}10 \mu\text{m}$, one can observe a decrease in stress from 0.7 to 0.3 GPa , a further sharpening of $\langle 110 \rangle$ texture, as well as an increase in crystallite size D from ~ 25 to $\sim 50 \text{ nm}$. The presence of this transition region within the PCD sublayer can also be identified in the EBSD inverse pole figure orientation maps (Fig. 4a and b), indicating competitive columnar grain growth, which ceases after about 2 to $2.5 \mu\text{m}$. At a thickness of ~ 10 to $\sim 22.5 \mu\text{m}$, the microstructure evolution becomes saturated within the PCD sublayer as a result of stable grain growth conditions. The variation in tensile stress across the PCD sublayer can be interpreted by the large size of the diamond crystallites, of which the analysis using the X-ray nanoprobe provided just very local information on the stress state. If the sampling volume were significantly larger, encompassing a much higher number of grains, the local stress variations would average out and result in a smoother stress profile, akin to that found in the NCD sublayer. The significant differences between the sublayers' observed intrinsic microstructural characteristics can be attributed to different deposition conditions

applied during the syntheses of the NCD and PCD sublayers. Especially the lower deposition temperature of $\sim 800^\circ\text{C}$ and the application of the $\text{Ar}/\text{H}_2/\text{CH}_4$ plasma played an important role in the formation of the nanocrystalline bottom (NCD) sublayer. The temperature difference of $\sim 100^\circ\text{C}$ in conjunction with two different types of plasma environments resulted in the formation of sublayers with profoundly distinct microstructural attributes. Interestingly however, in both sublayers, the presence of nucleation transition regions was detected by EM and CSNANOXRD. Within the transition regions all microstructural parameters such as texture, crystallite size, stress, and grain boundaries change rapidly before they reach a saturation state. The NCD and PCD sublayers exhibit different levels of residual stress of ~ 0.75 and 0.25 GPa (Fig. 8), which after adding the thermal stress component of ~ -0.72 and 0.81 GPa [12, 13, 15], indicate tensile growth stresses of 1.4 and 1.0 GPa, respectively. The difference in the growth stresses can be interpreted by the sublayers' microstructure. In particular, the larger portion of grain boundaries in the nanocrystalline base sublayer could be responsible for generating larger tensile growth stress as a result of the coalescence of columnar grain boundaries during the initial stages of the sublayer growth [7, 8]. The cross-sectional microstructure can be correlated with the mechanical properties of the sublayers, which were characterised using cross-sectional indentation and micro-cantilever bending experiments (Tab. 2). In general, the mechanical characterisation indicated significantly smaller hardness, fracture stress and Young's modulus for the NCD sublayer, compared to the PCD sublayer, which can be attributed to the nanocrystalline nature of the bottom sublayer, with small crystallites and a comparatively large volume fraction of grain boundaries. The obtained quantitative results of hardness and Young's moduli presented in Tab. 2 are in agreement with the results obtained from monolithic nanocrystalline and polycrystalline diamond thin films [26]. In the case of fracture stress, however, significantly larger values of 14.3 ± 0.6 and 31.6 ± 6.6 GPa were determined using the micro-cantilever bending method. These values appear significantly larger than the data evaluated from other diamond samples (*cf.* Fig. 4 in Ref. [26]), especially compared to the tensile strength data of 5.2 GPa from Olson *et al.* [40]. Compared to the data from micromechanical compressive tests on diamond single crystals [27], however, the obtained fracture stress values appear very reasonable and document the discrepancy between tensile and compressive strengths in diamond. In addition, the present data also indicate the advantage of the micro-cantilever approach. Unfortunately, it was not possible to perform a mechanical characterisation of the nucleation regions of the NCD and PCD sublayers, which would require further downscaling of the micromechanic specimens. One important novelty of this work is the application of a correlative cross-sectional nanoanalytics approach to the investigated multi-layered NCD/PCD thin film. The combination of EM and CSNANOXRD allowed for obtaining quantitative experimental data on the cross-sectional

evolution of microstructure and stress. These approaches were found to be quite complementary: while it was not possible to determine texture gradients in the NCD sublayer by means of EBSD analysis, CSnanoXRD allowed for obtaining very local information on texture gradient across the nanocrystalline transition nucleation region. The first application of CSnanoXRD to a diamond thin film demonstrated the possibilities of the technique to study depth gradients of microstructure and stress in both nanocrystalline and coarse-grained thin films. In order to obtain cross-sectional structure-property correlations for diamond thin films, the combination of EM and CSnanoXRD techniques on one side, and of cross-sectional micromechanical characterisation on the other represents a great methodological advance. There remains, however, the need to improve the spatial resolution of the mechanical tests.

Conclusions

In this work, a novel correlative cross-sectional nano-analytics approach was used to characterise cross-sectional structure-property relationships in a multi-layered CVD diamond film grown using microwave plasma-enhanced CVD and consisting of a $\sim 8 \mu\text{m}$ thick nanocrystalline (NCD) bottom and a $\sim 14.5 \mu\text{m}$ thick polycrystalline (PCD) top diamond sublayer. For the characterisation, depth-resolved micro-cantilever and hardness testing, electron microscopy methods and novel CSnanoXRD were applied. CSnanoXRD was used for the first time to study properties of diamond thin film. The cross-sectional experimental data revealed complex correlations between thin film mechanical properties, texture, crystallite size, residual stresses and deposition conditions. The fine-grained NCD and coarse-grained columnar PCD sublayers indicated the presence of nucleation regions with distinct gradual microstructures, which were investigated primarily by CSnanoXRD. The values of hardness and Young's moduli from both sublayers correlate well with the results reported from other monolithic CVD diamond thin films, whereas relatively large fracture stresses were observed using the micro-cantilever method. The presence of the gradual microstructures and stress gradients, however, documents the importance of the cross-sectional analysis, which should be further developed and downscaled. In summary, the nano-analytics approach allows for understanding the correlation between deposition conditions, cross-sectional gradients of microstructure, residual stress and mechanical properties and overall functional properties of diamond thin films.

Acknowledgement

The authors gratefully acknowledge the financial support under the scope of the Comet program within the K2 centre *Integrated Computational Material, Process and Product Engineering (IC-MPPE)*, (Project No. 859480).

This program is supported by the Austrian Federal Ministries for Transport, Innovation and Technology (BMVIT) and for Digital and Economic Affairs (BMDW), represented by the Austrian research funding association (FFG), and the federal states of Styria, Upper Austria and Tyrol.

This work was carried out with the support of CEITEC Nano Research Infrastructure (ID LM201504I, MEYS CR, 2016–2019), Ceitec Brno University of Technology.

References

- [1] P.W. May, *Diamond thin films: a 21st-century material*, Philos. Trans. R. Soc. A Math. Phys. Eng. Sci. 358 (2000) 473–495.
- [2] O. A. Williams, *Nanocrystalline diamond*, Diam. Relat. Mater. 20 (2011) 621–640.
- [3] F. Celii, J. E. Butler, *Diamond Chemical Vapor Deposition*, Annu. Rev. Phys. Chem. 42 (1991) 643–684.
- [4] O. Auciello, A.V. Sumant, *Status review of the science and technology of ultrananocrystalline diamond (UNCDTM) films and application to multifunctional devices*, Diam. Relat. Mater. 19 (2010) 699–718.
- [5] A. Van Der Drift, *Evolutionary selection, a principle governing growth orientation in vapour-deposited layers*, Philips Res. Repts. 22 (1967) 267–288.
- [6] C. Wild, N. Herres, P. Koidl, *Texture formation in polycrystalline diamond films*, J. Appl. Phys. 68 (1990) 973–978.
- [7] T. Liu, D. Raabe, W. M. Mao, *A review of crystallographic textures in chemical vapor-deposited diamond films*, Signal, Front. Mater. Sci. China 4 (2010) 1–16.
- [8] F. Silva, F. Bénédic, P. Bruno, A. Gicquel, *Formation of 110 texture during nanocrystalline diamond growth: An X-ray diffraction study*, Diam. Relat. Mater. 14 (3–7) (2005) 398–403.
- [9] W. Kulisch, C. Popov, *On the growth mechanisms of nanocrystalline diamond films*, Phys. Status Solidi. 203 (2006) 203–219.
- [10] K. J. Sankaran, B. R. Huang, A. Saravanan, D. Manoharan, N. H. Tai, I.N. Lin, *Nitrogen incorporated ultrananocrystalline diamond microstructures from bias-enhanced microwave N_2/CH_4 -plasma chemical vapor deposition*, Plasma Process. Polym. 13 (4) (2016) 419–428.
- [11] C. Kirchlechner, K. J. Martinschitz, R. Daniel, C. Mitterer, J. Keckes, *Residual stresses in thermally cycled CrN coatings on steel*, Thin Solid Films 517 (2008) 1167–1171.
- [12] N. Woehrl, T. Hirte, O. Posth, V. Buck, *Investigation of the coefficient of thermal expansion in nanocrystalline diamond films*, Diam. Relat. Mater. 18 (2–3) (2009) 224–228.

- [13] J. Michler, M. Mermoux, Y. Von Kaenel, A. Haouni, G. Lucazeau, E. Blank, *Residual stress in diamond films: Origins and modelling*, Thin Solid Films 357 (2) (1999) 189–201.
- [14] J. G. Kim, J. Yu, *A study on the residual stress measurement methods on chemical vapor deposition diamond films*, J. Mater. Res. 13 (1998) 3027–3033.
- [15] H. Li, B. W. Sheldon, A. Kothari, Z. Ban, B. L. Walden, *Stress evolution in nanocrystalline diamond films produced by chemical vapor deposition*, J. Appl. Phys. 100 (2006) 094309.
- [16] M. Mohr, L. Daccache, S. Horvat, K. Brühne, T. Jacob, H. J. Fecht, *Influence of grain boundaries on elasticity and thermal conductivity of nanocrystalline diamond films*, Acta Mater. 122 (2017) 92–98.
- [17] C. Hua, X. Yan, J. Wei, J. Guo, J. Liu, L. Chen, L. Hei, C. Li, *Intrinsic stress evolution during different growth stages of diamond film*, Diam. Relat. Mater. 73 (2017) 62–66.
- [18] H. Windischmann, G. F. Epps, Y. Cong, R. W. Collins, *Intrinsic stress in diamond films prepared by microwave plasma CVD*, J. Appl. Phys. 69 (1991) 2231.
- [19] M. Hempel, M. Härting, *Characterisation of CVD grown diamond and its residual stress state*, Diam. Relat. Mater. 8 (8–9) (1999) 1555–1559.
- [20] R. S. Balmer, J. R. Brandon, S. L. Clewes, H. K. Dhillon, J. M. Dodson, I. Friel, P. N. Inglis, T. D. Madgwick, M. L. Markham, T. P. Mollart, N. Perkins, G. A. Scarsbrook, D. J. Twitchen, A. J. Whitehead, J. J. Wilman, S. M. Woollard, *Chemical vapour deposition synthetic diamond: Materials, technology and applications*, J. Phys. Condens. Matter. 21 (36) (2009) 364221.
- [21] J. Philip, P. Hess, T. Feygelson, J. E. Butler, S. Chattopadhyay, K. H. Chen, L. C. Chen, *Elastic, mechanical, and thermal properties of nanocrystalline diamond films*, J. Appl. Phys. 93 (2003) 2164.
- [22] M. Mohr, A. Caron, P. Herbeck-Engel, R. Bennewitz, P. Gluche, K. Brühne, H. J. Fecht, *Young's modulus, fracture strength, and Poisson's ratio of nanocrystalline diamond films*, J. Appl. Phys. 116 (2014) 124308.
- [23] O. A. Williams, A. Kriele, J. Hees, M. Wolfer, W. Müller-Sebert, C. E. Nebel, *High young's modulus in ultra thin nanocrystalline diamond*, Chem. Phys. Lett. 495 1–3 (2010) 84–89.

- [24] H. D. Espinosa, B. Peng, N. Moldovan, T. A. Friedmann, X. Xiao, D. C. Mancini, O. Auciello, J. Carlisle, C. A. Zorman, M. Merhegany, *Elasticity, strength, and toughness of single crystal silicon carbide, ultrananocrystalline diamond, and hydrogen-free tetrahedral amorphous carbon*, Appl. Phys. Lett. 89 (2006) 073111.
- [25] F. S. Kachold, M. A. Lodes, S. M. Rosiwal, R. F. Singer, *Direct measurement of Young's modulus, fracture strength and fracture toughness of nanocrystalline diamond foil by means of tensile testing*, Acta Mater. 61 (2013) 7000–7008.
- [26] P. Hess, *The mechanical properties of various chemical vapor deposition diamond structures compared to the ideal single crystal*, J. Appl. Phys. 111 (2012) 051101.
- [27] J. M. Wheeler, R. Raghavan, J. Wehrs, Y. Zhang, R. Erni, J. Michler, *Approaching the Limits of Strength: Measuring the Uniaxial Compressive Strength of Diamond at Small Scales*, Nano Lett. 16 (2016) 812–816.
- [28] J. E. Butler, A. V. Sumant, *The CVD of Nanodiamond Materials*, Chem. Vap. Depos. 14 (2008) 145–160.
- [29] M. Wiora, K. Brühne, A. Flöter, P. Gluche, T. M. Willey, S. O. Kucheyev, A. W. Van Buuren, A. V. Hamza, J. Biener, H.-J. Fecht, *Grain size dependent mechanical properties of nanocrystalline diamond films grown by hot-filament CVD*, Diam. Relat. Mater. 18 (2009) 927–930.
- [30] X. Li, D. Diao, B. Bhushan, *Fracture mechanisms of thin amorphous carbon films in nanoindentation*, Acta Mater. 67 (1997) 4453–4461.
- [31] C. S. Pickles, *The fracture stress of chemical vapour deposited diamond*, Diam. Relat. Mater. 11 (2002) 1913–1922.
- [32] K. An, L. Chen, X. Yan, X. Jia, J. Liu, J. Wei, Y. Zhang, F. Lu, C. Li, *Fracture strength and toughness of chemical-vapor-deposited polycrystalline diamond films*, Ceram. Int. 44 (2018) 17845–17851.
- [33] J. Keckes, M. Bartosik, R. Daniel, C. Mitterer, G. Maier, W. Ecker, J. Vila-Comamala, C. David, S. Schoeder, M. Burghammer, *X-ray nanodiffraction reveals strain and microstructure evolution in nanocrystalline thin films*, Scr. Mater. 67 (2012) 748–751.

- [34] J. Keckes, R. Daniel, J. Todt, J. Zalesak, B. Sartory, S. Braun, J. Gluch, M. Rosenthal, M. Burghammer, C. Mitterer, S. Niese, A. Kubec, *30 nm X-ray focusing correlates oscillatory stress, texture and structural defect gradients across multilayered TiN-SiO_x thin film*, *Acta Mater.* 144 (2018) 862–873.
- [35] J. Kieffer, D. Karkoulis, *PyFAI, a versatile library for azimuthal regrouping*, *J. Phys. Conf. Ser.* 425 (2013) 202012.
- [36] M. Stefenelli, J. Todt, A. Riedl, W. Ecker, T. Müller, R. Daniel, M. Burghammer, J. Keckes, *X-ray analysis of residual stress gradients in TiN coatings by a Laplace space approach and cross-sectional nanodiffraction: A critical comparison*, *J. Appl. Crystallogr.* 46 (2013) 1378–1385.
- [37] W. C. Oliver, G. M. Pharr, *Measurement of hardness and elastic modulus by instrumented indentation: Advances in understanding and refinements to methodology*, *J. Mater. Res.* 19 (2004) 3–20.
- [38] M. J. Pfeifenberger, M. Mangang, S. Wurster, J. Reiser, A. Hohenwarter, W. Pfleging, D. Kiener, R. Pippin, *The use of femto-second laser ablation as a novel tool for rapid micro-mechanical sample preparation*, *Mater. Des.* 121 (2017) 109–118.
- [39] K. Matoy, H. Schönherr, T. Detzel, T. Schöberl, R. Pippin, C. Motz, G. Dehm, *A comparative micro-cantilever study of the mechanical behavior of silicon based passivation films*, *Thin Solid Films* 518 (2009) 247–256.
- [40] D. S. Olson, G. J. Reynolds, G. F. Virshup, F. I. Friedlander, B. G. James, L. D. Partain, *Tensile strength of synthetic chemical-vapor-deposited diamond*, *J. Appl. Phys.* 78 (1995) 5177–5179.

*20 Hz synchrotron X-ray diffraction analysis in laser-pulsed WC–Co hard metal reveals oscillatory stresses and reversible composite plastification**

David P. GRUBER ^{a,b}, Dominik KIEFER ^c, Ralf RÖSSLER ^c, Felix BECKMANN ^d, Michael TKADLETZ ^a, Thomas KLÜNSNER ^e, Christoph CZETTL ^f, Jozef KECKES ^{a,b} and Jens GIBMEIER ^c

Abstract

THE LIFETIME of WC–Co inserts used in cutting processes, such as milling, is limited by millisecond temperature and mechanical pulses, which occur as a result of interrupted tool–workpiece contact, thermal fatigue and wear. In the current work, synchrotron X-ray diffraction (XRD) was used in conjunction with a pulsed laser heating set-up to characterise the time-dependent development of stresses and microstructure in locally irradiated WC–Co inserts coated by chemical vapour deposition with 6.5 μm and 3.5 μm thick TiCN and $\alpha\text{-Al}_2\text{O}_3$ films, respectively. Diffraction data from the WC–Co phase were used to evaluate the time and temperature-dependent evolution of in-plane stresses, thermal strains and integral breadths of WC diffraction peaks in experiments with a single and five successive laser shocks applied within 2.2 and 20 seconds, respectively, using a laser spot diameter of ~ 5.8 mm and an X-ray beam size of 1×1 mm². The laser heating induces the formation of compressive stresses in the inserts' substrates. Above a temperature of ~ 750 °C, at the onset of WC–Co composite plastification, compressive stresses relax and then vanish in WC at the maximal applied temperature of ~ 1300 °C, followed by the build-up of tensile stresses. The applied cyclic heating up and cooling down led to the repetitive formation of compressive and tensile stresses, with temperature dependencies oscillating with the number of applied laser pulses. The observed relatively high tensile stress level of ~ 1100 MPa in WC was a consequence of the stabilising function of the coating, which hindered the initiation of surface hot cracks and stress relaxation.

* This piece of research was first published in *International Journal of Refractory Metals and Hard Materials* vol. 82 (August 2019) pp. 121–128, DOI: 10.1016/j.ijrmhm.2019.04.004.

The version presented here features marginal stylistic and typographical corrections.

a Department of Materials Physics, Montanuniversität Leoben, Leoben, Austria

b Erich Schmid Institute for Materials Science, Austrian Academy of Sciences, Leoben, Austria

c Institute of Applied Materials, Karlsruhe Institute of Technology, Karlsruhe (KIT), Germany

d Institute of Materials Research, Helmholtz-Zentrum Geesthacht (HZG), Geesthacht, Germany

e Materials Center Leoben Forschung GmbH, Leoben, Austria

f Ceratizit Austria GmbH, Breitenwang, Austria

Introduction

WC-CO HARD METAL cutting inserts are composite materials based on hard ceramic tungsten carbide and a cobalt metallic binder. They are extensively used in the machining tool industry due to their high hardness and toughness as well as excellent wear and high-temperature characteristics. In order to increase the life-time of the inserts, ceramic coatings such as TiN, Al₂O₃, TiAlN and CrAlN with a thickness of several micrometres are usually deposited onto the hard metal by means of chemical (CVD) or physical (PVD) vapour deposition processes [1]. In metal cutting operations, the friction between insert and metal induces localised high temperature shocks on the cutting inserts with peak temperatures reaching more than 1000 °C [2]. During cyclically interrupted cutting processes, such as milling, the tool lifetime is affected by millisecond temperature and mechanical pulses, which occur as a result of interrupted tool-workpiece contact and cause wear and thermal fatigue. The periodic localised thermal shocks cause rapid changes in lateral and depth-dependent stress distributions, as a result of (i) thermal stress changes caused by the mismatch of coefficients of thermal expansions (CTEs) between coating and substrate, (ii) intrinsic stress changes as a result of microstructural (and also phase) changes in the coating and (iii) non-uniform temperature distributions across the cutting insert [3]. Consequently, there exist several stages of cutting insert damage caused by the thermo-mechanical fatigue, as discussed by Kirchhoff *et al.* [2] involving the formation of surface and delamination cracks and coating spalling. Crack formation is fostered by the build-up of tensile residual stresses triggered by localised plasticity of substrate [4] and coating [5]. For a particular coating-substrate system, the degree of damage depends on the maximum temperature and duration of applied pulses as well as on the magnitude of the friction-induced thermo-mechanical stress and the number of applied cycles. The cyclic thermo-mechanical fatigue of WC-Co composites has been studied both experimentally [6–8], as well as using simulation tools to quantify thermal metal machining tool loads [9, 10]. In order to predict the degree of local damage induced by the interrupted tool-workpiece contact and wear, a variety of material parameters have to be taken into account, such as CTEs, thermal conductivities and elasto-plastic properties of the coating-substrate composite, all of which are dependent on temperature, crystallite size as well as geometry and the time-scale of the underlying process. Most recent experimental studies were devoted primarily to the ex-situ analysis of thermo-mechanically loaded inserts from real cutting experiments [2] and WC-Co composites treated in laser thermal shock experiments [7, 8, 11]. The latter provide the opportunity to evaluate the influence of controllably induced thermomechanical damage, separated from occurring friction loads. The ex-situ studies of the laser shocked samples manifested the complex nature of thermal fatigue resulting from the formation of lateral and depth gra-

dients of stresses, microstructure and phases, as discussed by Bartosik *et al.* [11]. Although several studies have been performed on laser shock induced damage in coating-substrate composites, the underlying localised time and temperature-dependent evolution of phases, microstructure, and stresses as well as the incorporated mechanisms in terms of materials science still remain unknown. Recently, a novel in-situ characterisation approach based on a millisecond synchrotron X-ray diffraction (XRD) analysis coupled with a pulsed laser sample treatment was introduced by Kostov *et al.* [12]. The complex experimental set-up makes it possible to characterise temporal evolutions of lattice strain, stress and microstructure, as well as to perform real-time monitoring of phase transformations of rapidly heated samples in the laser focus of several millimetres, which overlaps with the synchrotron X-ray beam footprint on the investigated sample surface. Predominantly, this set-up was applied to investigate the laser surface hardening of steel [13]. In the current work, this well-established synchrotron X-ray setup [12] was used to in-situ characterise WC-Co inserts coated with a PVD TiCN/Al₂O₃ bilayer, which was locally heated using a high-power diode laser (HPDL) up to a maximum temperature of 1300 °C, applying (i) a single and (ii) five successive heating cycles. The objectives were (i) to test the transferability of the synchrotron XRD set-up to the field of cutting inserts analysis, (ii) to evaluate the time-dependent evolution of stresses and finally the formation of residual stresses, the evolution of microstructure and (iii) to assess thermally driven mechanisms governing stress build-up and relaxation.

Experiment and methodology

The medium grained WC-Co inserts studied in this work came in SNUN 120412 geometry (according to ISO 1832) with a chemical composition of 77 wt% WC, 12 wt% mixed carbides and 11 wt% Co. All inserts were mechanically fine-polished to minimise surface roughness and subsequently coated with a CVD bilayer architecture featuring a TiCN base layer with a thickness of ~6.5 µm and a top layer of α -Al₂O₃ with a thickness of ~3.5 µm. The TiCN base layer was deposited from precursors of TiCl-CH₃CN-H₂-N₂-CO at a temperature of 900 °C and a pressure of 100 mbar, while the overlying α -Al₂O₃ top layer was grown using AlCl₃-CO₂-H₂-H₂S precursors at a temperature of 1000 °C and a pressure of 75 mbar. The coating deposition was carried out in an industrial scale *SucoTec SCT600TH* CVD plant. Subsequent to the deposition, the coated inserts were subjected to a wet blasting treatment with the central aim of changing the residual stress state of coating and substrate from tensile to compressive as summarised in our previous work [14]. The inserts were analysed using the dedicated in-situ XRD set-up described by Kostov *et al.* in [12] at the P05 beamline of the PETRA III synchrotron source of DESY in Hamburg, Germany. Enhancements of

FIGURE 1: Schematic drawing of the experimental set-up at the p05 beamline of PETRA III at DESY showing the geometrical arrangement of sample, X-ray beam, HPDL, pyrometer and the four detectors. The set-up was installed in a process chamber, which guaranteed laser radiation protection and application of a defined atmosphere for the temperature controlled process (see also [12]).

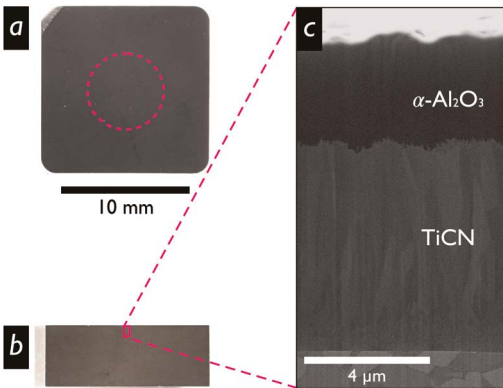
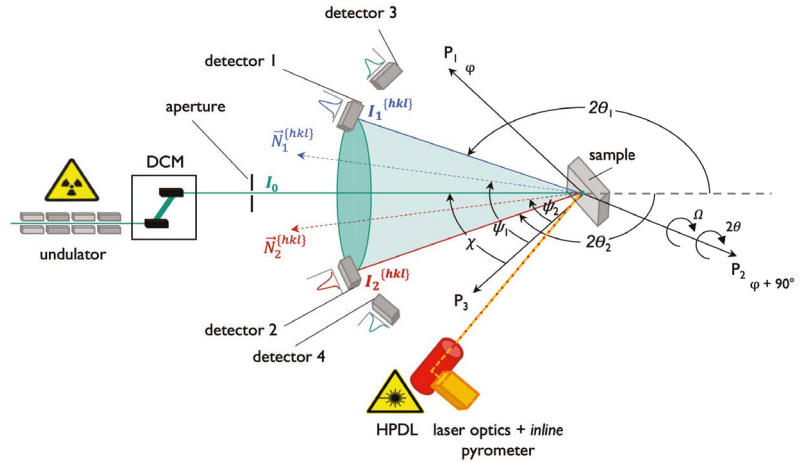


FIGURE 2: Optical (a,b) and secondary electron SEM (c) micrographs from the cutting insert surface (a) with indication of the area irradiated by the laser beam and cross-sections (b,c) of the WC-Co/TiCN/ Al_2O_3 sample, which indicated no structural sample damage after applying five successive laser pulses.

the set-up were reported in [15, 16]. In the used experimental configuration (Fig. 1) the incident focussed X-ray beam with intensity I_0 hit the laser heated cutting insert at an angle χ with respect to the sample normal. Diffracted intensities $I_1^{hkl_1}$ and $I_2^{hkl_2}$ from the two hkl Debye-Scherrer rings were collected by the stripe detectors 1 to 4, positioned at four different orientations with respect to the sample normal. Each of the hkl_1 and hkl_2 reflections was recorded at two different diffraction vectors $\mathbf{N}_i^{hkl_1}$ and $\mathbf{N}_i^{hkl_2}$ at orientations ψ_i , ($i = 1, 2$) and allowed the analysis of stresses according to the $\sin^2\psi$ method. The set-up featured a helium-filled process chamber with a sample stage and a HPDL unit *LDM 4000-100* from *Laserline GmbH*, Mühlheim-Kärlich, Germany, with a maximum power of ~ 4 kW at a wavelength of 1020 nm. The laser beam possessed a Gaussian intensity distribution with a focus spot diameter of ~ 5.8 mm. The sample surface temperature and thereby the laser power output was controlled during laser shocks using a one-colour pyrometer operating at a sampling rate of 100 Hz in the temperature range of 190–1500 °C. The coated inserts were heated to a maximum temperature of 1300 °C, applying a heating rate of 1000 °C s⁻¹. The cooling phase was, in an analogous manner, realised by means of temperature control at a cooling rate of -1000 °C s⁻¹ down to a temperature of ~ 200 °C or, finally to ambient temperature, *i.e.* the controlled cooling was achieved by adjusting the laser power. However, starting at a temperature of ~ 600 °C the cooling rate was smaller, due to the relatively large sample volume and the non-zero heat capacity of the cutting inserts. In the XRD experiment, a photon energy of 10.180 keV ($\lambda = 0.12189$ nm) was used, while the X-ray spot was set to dimensions of 1×1 mm² by use of a cross slit aperture. The diffraction signal from the samples was collected using four fast silicon strip line detectors *Mythen 1K* from *Dectris Ltd.*, Switzerland, featuring a pitch size of 50 μm , of which the angular positions were calibrated using a LaB_6 powder standard. Throughout the in-situ experiments, the detector sampling rate was set to 20 Hz, resulting in an exposure

time of 50 ms. During all performed in-situ experiments, the four detectors recorded the diffraction signal from multiple different hkl crystallographic planes with four distinct orientations with respect to the sample normal (Fig. 1). Due to the weak diffraction signal from the coatings, it was, unfortunately, not possible to evaluate the diffraction data from the Al_2O_3 and TiCN coating sublayers and the measurements provided sufficient diffraction information from the WC phase only. At a heating rate of $1000^\circ\text{C s}^{-1}$ and the applied sampling time of 50 ms, the resulting temperature resolution was $\sim 50^\circ\text{C}$. In the temperature range of $25\text{--}1300^\circ\text{C}$, it was possible to collect hkl diffraction peaks at diffraction angle positions $2\vartheta_{\Psi_i}^{hkl,T}$, using each of the two detector pairs, where Ψ_i represents the angle between the diffraction vector and the sample normal (Fig. 1). The detector pairs were mounted in such a fashion, that detectors 1 and 2 covered a 2ϑ -range of $140\text{--}158^\circ$, while detectors 3 and 4 covered the range of $121.5\text{--}133^\circ$. The recorded diffraction peaks were fitted using a Pseudo-Voigt function, followed by the evaluation of integral breadths $\beta_{\Psi_i}^{hkl,T}$ and positions of Bragg's angle $\vartheta_{\Psi_i}^{hkl,T}$ of the peaks. The diffraction data were then used to quantify lattice spacings $d_{\Psi_i}^{hkl,T}$ according to Bragg's law. Subsequently, $\vartheta_{\Psi_i}^{hkl,T}$ versus Ψ_i dependencies were used to evaluate in-plane X-ray elastic strains $\varepsilon_{\text{el}}^{hkl,T}$ and thermal strains $\varepsilon_{\text{th}}^{hkl,T}$ by considering the strain free direction $\Psi^{hkl,*}$, which can be calculated based on the assumption of an equi-biaxial stress state and a negligible out-of-plane stress component in the WC phase as $\Psi^{hkl,*} = -2s_1^{hkl}/s_2^{hkl}$. In-plane X-ray elastic strains were used to quantify magnitudes of in-plane stress using $\sigma^{hkl,T} = \varepsilon_{\text{el}}^{hkl,T}/s_2^{hkl}$. Parameters s_1^{hkl} and s_2^{hkl} represent X-ray elastic constants calculated for WC based on the Kröner grain interaction model [17], using WC single crystal elastic constants $c_{11} = 7.2 \times 10^{11}$ Pa, $c_{12} = 2.54 \times 10^{11}$ Pa, $c_{33} = 9.72 \times 10^{11}$ Pa and $c_{44} = 3.28 \times 10^{11}$ Pa [18]. Further details on the evaluation procedure can be found elsewhere [12].

In an entirely isotropic case, the evaluated in-plane stresses $\sigma^{hkl,T}$ would be independent of hkl , assuming that the applied grain interaction model is valid. It often occurs, however, that in the case of neutron and synchrotron diffraction analyses of stresses, the evaluation procedure results in strongly hkl -dependent values of $\sigma^{hkl,T}$. This effect can have various origins, such as the anisotropic elastic stiffness of individual diffracting grains, grain-size dependent plasticity, intragranular strains, anisotropic strain relaxation along specific slip systems etc. Therefore, it is convenient to introduce a weighted or average $\sigma^{\text{avg},T}$, which is determined as a mean value from the evaluated $\sigma^{hkl,T}$ with a texture index of 1 [19].

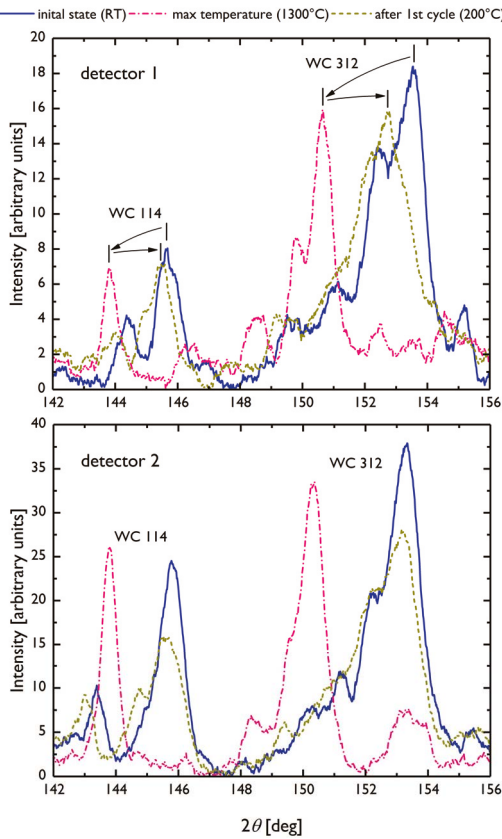


FIGURE 3: Examples of XRD patterns recorded by detectors 1 and 2, mounted at two different angular orientations Ψ_i with respect to the sample normal. The relative shifts in WC phase reflections recorded during one applied laser pulse at room temperature (RT), 1300°C and 200°C are the result of lattice parameter thermal expansion and the presence of stresses in the imprint of the X-ray beam on the sample surface. Unfortunately, the diffraction signal from the Al_2O_3 and TiCN phases was too weak to be further analysed.

Results and discussion

SEM analysis

The surfaces and cross-sections of the irradiated cutting inserts were analysed ex-situ using optical microscopy and scanning electron microscopy (SEM) after the laser shock experiments. Low-magnification surface (a) and cross-sectional (b) optical micrographs of the sample heated up for five cycles using the laser set-up are presented in Fig. 2, together with a secondary electron SEM cross-section (c) prepared by focussed ion beam milling. Neither the optical, nor the SEM analysis indicated apparent structural sample damage induced by thermal fatigue.

Single laser pulse experiment

In the first conducted experiment, the HPDL unit from Fig. 1 was used to heat a WC-Co/TiCN/ Al_2O_3 sample to a surface temperature of 1300°C, which was reached within ~ 1.1 s, followed by a controlled cooling down phase to a surface temperature below ~ 200 °C within a time span of ~ 2.2 s. In Fig. 3, examples of XRD patterns from two of the detectors indicate the relative shifts of WC 114 and 312 reflections due to the presence of stress in the probed WC volume, as well as the shifts of the individual reflections caused by the temperature changes. Furthermore, the selected diffractograms from detectors 1 and 2 indicate that the peak widths of the individual diffraction lines change during processing, indicating changes in the local microstructure through the laser irradiation. High temperature XRD (HT-XRD) data, recorded by detectors 1 and 2 during the temperature cycle, are presented together with temperature data from the pyrometer in Fig. 4 as a function of the processing time in a 2D contour plot. After initiating the laser heating, the sample surface reached a temperature of 200°C, which was the approximate sensitivity threshold of the pyrometer. Further heating resulted in a shift of WC diffraction peaks towards lower 2ϑ angles on all four detectors, as a consequence of WC thermal expansion and the related build-up of mechanical stresses. Diffraction peaks shifted back towards larger 2ϑ values during the temperature decrease in the subsequent controlled cooling down phase.

The recorded high-temperature data from the four detectors were subsequently used to evaluate thermal strains $\varepsilon_{\text{th}}^{hkl,T}$. The time-dependencies of $\varepsilon_{\text{th}}^{hkl,T}(t)$ presented in Fig. 5 show the increase and decrease of thermal strains during the single laser pulse experiment. Data of $\varepsilon_{\text{th}}^{hkl,T}$ can be correlated with the temperature changes while all dependencies $\varepsilon_{\text{th}}^{hkl,T}$, *i.e.* for the 114, 303 and 312 diffraction lines of WC, show a very similar behaviour (*cf.* Fig. 5). As indicated in Sec. 2, high-temperature diffraction data were used to evaluate the temperature-dependent evolution of in-plane stresses in the laser

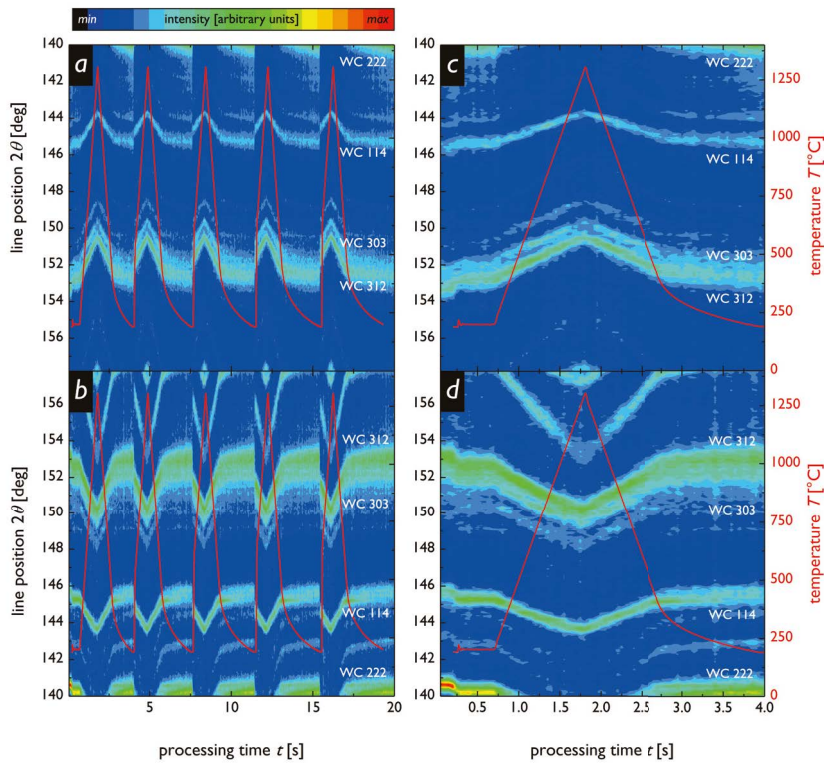


FIGURE 4: Examples of HT-XRD patterns (2D contour plot) recorded by detectors 1 (a,c) and 2 (b,d) revealed shifts of WC reflections during five successively applied laser pulses (a,b), as well as during the first pulse (c,d) with a maximum temperature of $\sim 1300^\circ\text{C}$ measured by the pyrometer. The shifts of the reflections were caused by the thermal expansion of WC and the related formation of stresses. The pyrometer employed in recording the sample surface temperature was calibrated for a T range of $190\text{--}1500^\circ\text{C}$.

heated sample volume. In Fig. 6, temperature dependencies of hkl -dependent in-plane stress $\sigma^{hkl,T}$ for three representative reflections are presented together with the average in-plane stress profile $\sigma^{\text{avg},T}$. It is apparent, that all $\sigma^{hkl,T}$ dependencies show similar qualitative behaviour, *i.e.* an increase in compressive stress and subsequent formation of radial tensile stresses, as discussed in our previous reports [3–20]. In the data, one can identify (i) varying maximum magnitudes of individual $\sigma^{hkl,T}$ dependencies (occurring in both domains, tensile and compressive alike) as well as (ii) slightly different shapes of the dependencies $\sigma^{hkl,T}(t)$.

The observation of hkl -dependent in-plane stresses can, in general, be interpreted by the (hkl) -dependent elasto-plastic anisotropy of hexagonal WC [21], which influences the WC deformation in both the elastic and plastic domains. Therefore, it is not trivial to obtain a continuum mechanics equivalent of elastic strains and stresses from the performed synchrotron X-ray diffraction measurements. The evaluated values of averaged in-plane stress $\sigma^{\text{avg},T}$, however, provide a reasonable representation of the temperature and time-dependent evolution of in-plane stresses within the sample (Fig. 6). Preceding the laser pulse experiment, the value of $\sigma^{\text{avg},T}$ is ~ -300 MPa. During the heating up to $T \sim 750^\circ\text{C}$, $\sigma^{\text{avg},T}$ increased in the compressive domain to a value of ~ -1300 MPa due to the thermal expansion of the laser irradiated WC-Co substrate volume and the constraint given by the colder surrounding material. Exceeding measured sample surface temperatures of $\sim 750^\circ\text{C}$ at $t \sim 1.2$ s led to plastification effects in the WC-Co composite, resulting in compressive stress relaxation.

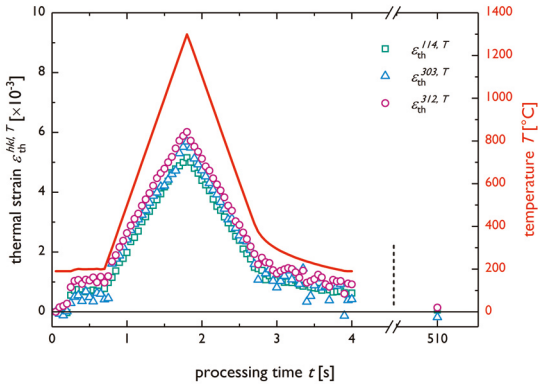


FIGURE 5: Time-dependent evolution of in-plane thermal strains $\varepsilon_{th}^{hkl,T}(t)$ for selected WC hkl reflections. The pyrometer employed in recording the sample surface temperature was calibrated for a T range of 190–1500°C.

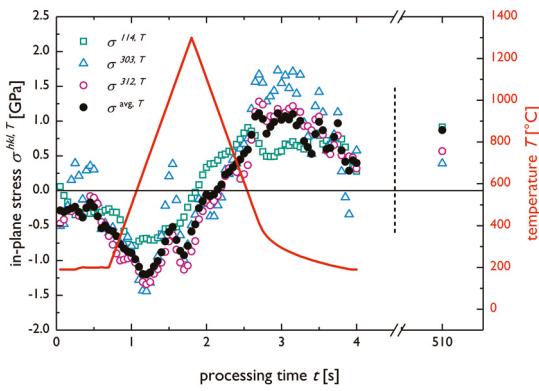


FIGURE 6: Time-dependent evolution of in-plane stresses $\sigma^{hkl,T}(t)$ for selected WC hkl reflections and averaged in-plane stress $\sigma^{avg,T}$ during one single laser pulse. Individual profiles of $\sigma^{hkl,T}$ differed significantly between particular hkl reflections.

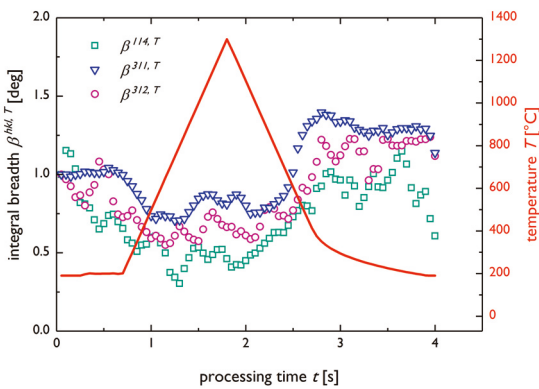


FIGURE 7: Time-dependent evolution of normalised integral breadths $\beta^{hkl,T}(t)$ for selected WC hkl reflections during one single laser pulse, indicating oscillatory peak broadening behaviour. The absolute changes in $\beta^{hkl,T}$ values differ significantly between the individual hkl reflections.

At the maximum applied temperature of $\sim 1300^\circ\text{C}$, $\sigma^{avg,T}$ relaxed to ~ -450 MPa. Subsequent controlled cooling down led to a further decrease of the compressive stress components, with $\sigma^{avg,T}$ reaching the zero level at a temperature slightly above $\sim 1000^\circ\text{C}$. Further cooling down initiated the build-up of average tensile stresses of up to ~ 1100 MPa, most probably as a consequence of the radial enlargement of the plastically deformed material in the centre of the laser focus. After the controlled cooling phase, tensile stresses relaxed to a plateau level of ~ 400 MPa within ~ 500 s as the temperature of the cutting insert converged to ambient temperature. A local minimum in $\sigma^{avg,T}$ occurring at $t \sim 1.7$ s coincided with the PVD coating deposition temperature and could be the consequence of coating-substrate interaction. In the experiments the pyrometer-based temperature measurement was calibrated for a T range of 190–1500°C, *i.e.* values presented in Figs. 4–8 below a threshold of 190°C at $T = 0$ to ~ 0.75 s did not reflect the true sample surface temperature. The measured temperature values reflected the temperature at the coating surface, while the heat transfer from the coating to the surface-near substrate region was assumed to take place quasi-instantaneously.

The individual diffractograms used to depict the time and temperature evolution of individual hkl reflections in Fig. 4 were fitted using a Pseudo-Voigt function. Values of integral breadths $\beta^{hkl,T}$ for selected reflections are presented in Fig. 7. Since the values of $\beta^{hkl,T}$ differed between individual reflections, data of $\beta^{hkl,T}$ presented in Figs. 7 and 8 have been normalised using the value of $\beta^{hkl,T}$ obtained at room temperature before the experiment, as a reference. Remarkably, the observed profiles of $\beta^{hkl,T}$ showed a periodic temperature evolution, *i.e.* all values of $\beta^{hkl,T}$ decrease during heating-up, succeeded by the appearance of a local maximum at the peak temperature of $\sim 1300^\circ\text{C}$, after which $\beta^{hkl,T}$ values started to rise again before saturating (*cf.* Fig. 7). In the main, the integral breadth of xrd peaks correlated with the size of coherently diffracting domains $\langle D \rangle$, as well as structural crystallographic defects such as dislocations and various other crystal lattice distortions, represented by inhomogeneous, *i.e.* non-directional, strains of 2nd and 3rd order [22]. In addition, $\langle D \rangle$ also correlates with the intrinsic contribution of the diffraction system, which is referred to as instrumental broadening. Since, in the present case, changes in $\langle D \rangle$ of the ceramic material can be supposedly neglected (at temperatures significantly smaller than the WC melting point temperature of $\sim 2870^\circ\text{C}$), the periodic integral breadth profiles in Fig. 7 can be interpreted by reversible annihilation and formation of structural defects in WC crystallites [20]. It is supposed that a certain type of structural recovery (*cf.* Sec. IV) occurs in the WC-Co composite material during heating up, and that during the cooling down phase, new defects are generated as a result of the formation of stresses in the laser irradiated sample volume. The appearance of the observed local maximum at $\sim 1300^\circ\text{C}$ and possible governing mechanisms are discussed in Sec. 4.

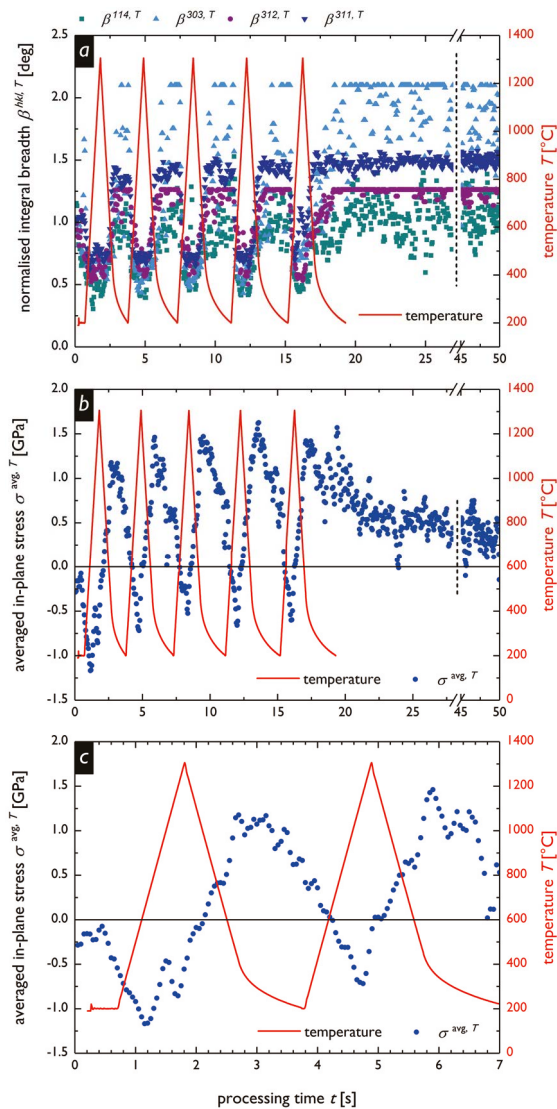


FIGURE 8: Time-dependent evolution of normalised integral breadth $\beta^{hkl,T}(t)$ (a) and averaged in-plane stress $\sigma^{avg,T}$ (b) during five successively applied laser pulses correlated with the corresponding substrate temperature. Detailed plot of $\sigma^{avg,T}$ for the first two applied pulses (c). The pyrometer used for recording the sample surface temperature was calibrated for a T range of 190–1500°C.

Multiple laser shot experiment

A follow-up in-situ experiment including five successive laser pulses in the temperature range of 25 to 1300°C was performed in order to evaluate the effect of multiple heating up and cooling down cycles on the evolutions of $\sigma^{avg,T}(t)$ and $\beta^{hkl,T}(t)$, which are presented together in Fig. 8. The temperature dependencies of $\beta^{hkl,T}$ (Fig. 8a) indicate similar behaviour as in the case of the single pulse experiment (*cf.* Fig. 7), *i.e.* inverse temperature dependence with pulse-number independent minimum $\beta^{hkl,T}$ values occurring at the peak temperatures of 1300°C for all five successive reflections and pulses.

Also, in the case of averaged in-plane stress $\sigma^{avg,T}$ presented in Fig. 8b,c, the $\sigma^{avg,T}(t)$ profile shows a behaviour similar to that from the single pulse experiment (*cf.* Fig. 6). The data reveal that the in-plane stresses turn compressive after the initiation of each heating

pulse, and become tensile during the successive cooling down phase. In a similar fashion as in Fig. 6, the maximum compressive stress was not observed at the peak temperature, but was reached at a time lag a few hundred degrees below. At the applied maximum substrate temperature, stresses were still in the tensile regime before reaching the zero level during cooling down at about $\sim 1000^\circ\text{C}$. Furthermore, the time-dependent behaviour of $\sigma^{\text{avg},T}(t)$ during five successive laser pulses shows the following attributes: (i) the maximum compressive stress during heating up of every pulse decreased with the number of applied laser pulses, while in a similar fashion (ii) the maximum magnitude of tensile stress of individual pulses was found to increase, before saturating. In the aftermath of the final pulse, the tensile stress level started to decrease exponentially and tended to saturate at a level of $\sim 400\text{MPa}$. This stress relaxation process appeared to continue until the insert reached ambient temperature (Fig. 8). Additionally, the detailed data in Fig. 8c, collected during the first heating cycle, indicated that the relaxations of compressive and tensile stresses start at $\sim 650^\circ\text{C}$ and 350°C , respectively.

Discussion on governing mechanism

In-situ synchrotron X-ray diffraction studies of coated WC-Co cutting inserts during laser processing revealed insight into strain, stress, and microstructure evolution in real time. Time resolved lattice strain and broadening of diffraction profiles can be used for the assessment of deformation and degradation mechanisms (*cf.* results presented in Figs. 6–8).

The mechanisms of compressive and tensile stress formation during heating up and cooling down are schematically depicted in Fig. 9a and b, respectively. The substrate heating up effects the rapid thermal expansion of the irradiated WC-Co volume, which is itself constrained by the cooler surrounding material, therefore resulting in the build-up of compressive stresses up to a level of the WC-Co composite's limit of plastic deformation. During the subsequent cooling phase, the plastically deformed material in the laser heated spot contracted but was constrained by the surrounding material which led to the development of tensile stresses.

Based on the lattice strain determined for various $\{hkl\}$ lattice planes, averaged stress values $\sigma^{\text{avg},T}$ were calculated following the approach proposed by Daymond [19] (*cf.* Figs. 6 and 8). The average stress distributions show that the maximum compressive stress of $\sim 1300\text{MPa}$ was reached in the laser heated spot at a temperature of $\sim 750^\circ\text{C}$ during the first heating cycle, while further heating up led to the relaxation of compressive stresses, with total relaxation reached during the cooling down process, with $\sigma^{\text{avg},1000^\circ\text{C}} \sim 0$. The observed decrease in stress during heating up at temperatures above $\sim 750^\circ\text{C}$ (Figs. 6 and 8b,c) can be correlated with the oscillatory behaviour of $\beta^{hkl,T}$ (Fig. 7), where values decreased, increased, and again decrea-

sed during one temperature pulse. In order to understand this unexpected behaviour, it must be considered that the yield stress $R_{p,0.2}$ of WC-Co composites of $\sim 3500\text{--}7000$ MPa at room temperature [4, 23] decreased rapidly by a factor of about five between 25°C and 900°C [24]. Above a temperature of 700°C , the yield strength was observed to decrease even more rapidly than at lower temperatures [24]. Also, pure WC was reported to show relatively ductile behaviour with a tensile fracture strain under bending conditions of larger than 0.2% at 1000°C [21]. Therefore, the start of the compressive stress relaxation observed at stress levels of $\sigma^{\text{avg},750^\circ\text{C}} \sim -1300$ MPa (cf. Figs. 6,8c) as well as the increase in $\beta^{\text{hkl},T}$ (Fig. 7) during heating up at $\sim 750^\circ\text{C}$ can be correlated with the onset of plastification of the WC crystallites. Additionally, it must be expected that the heating up also resulted in plastification and softening of the Co binder phase, of which the temperature evolution remained inaccessible. Therefore, it can be generally supposed that the decrease in compressive stress at $\sim 750^\circ\text{C}$ in Figs. 6 and 8 can be attributed to the softening of the interacting WC and Co phases within the hard metal composite.

Further heating to temperatures above 750°C most probably induces increased softening of the WC-Co composite accompanied by the stress relaxation in WC, and supposedly also Co, and the formation of microstructural defects like dislocations, slip planes and grain boundaries [21], which are responsible for the occurrence of the observed local maximum of $\beta^{\text{hkl},T}$ in Fig. 7. During the second (and later) pulses, the onset of WC-Co composite plastification points appeared to occur at higher temperatures, as can be observed in detail in Fig. 8c.

The interesting effects of (i) the increasing maximum magnitude of tensile stresses $\sigma^{\text{avg},T}$ in Fig. 8b,c with the increasing number of applied pulses and (ii) the shift of the stress relaxation temperature (Fig. 8c) already after the first heating cycle can be attributed to the pulse-number related (stepwise) hardening of the WC phase. The controlled cooling down resulted in the build-up of a three-dimensional tensile stress distribution, possessing a two-dimensional Gaussian lateral profile, which decreased exponentially as a function of sample depth [11, 20, 25, 26]. The presence of the coating protected the WC-Co substrate from (i) heat transfer into the substrate volume and (ii) the formation of hot cracks, as documented for CrN coated steel [26]. This behaviour was obviously indirectly observed also in the present case, where the cooling down after the laser pulses resulted in the formation of tensile stresses, with stepwise increasing amplitudes. Literature values of tensile strength of WC skeletons produced by removing the binder phase by etching, are in the range of ~ 500 MPa, and are most likely influenced by the presence of etching-induced microvoids [21]. However, measured maximum tensile stresses $\sigma^{\text{avg},T}$ in the WC phase showed values of up to ~ 1100 MPa. This observed relatively high tensile strength of the investigated substrate-coating composite structures is attributed to the

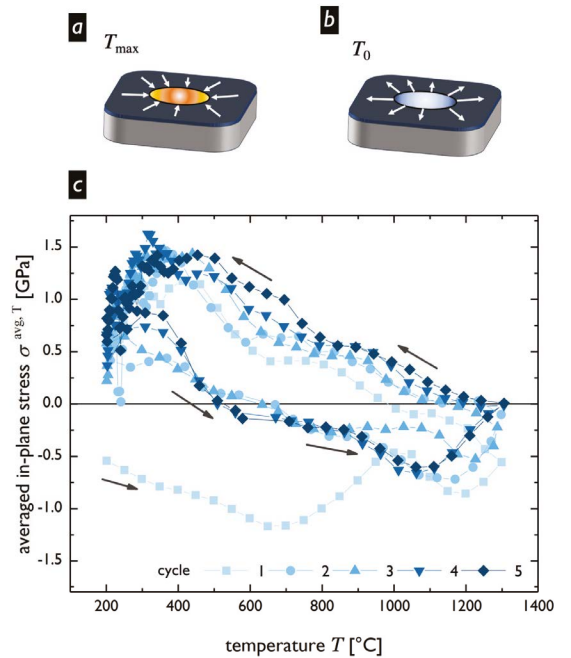


FIGURE 9: Schematic depiction of compressive (a) and tensile (b) stress formation in the material in and surrounding the laser irradiated spot in the investigated cutting inserts during heating up and cooling down, respectively. In (c), experimental data from Fig. 8c shows the time evolution of averaged in-plane stress $\sigma^{\text{avg},T}$ as a function of the measured sample temperature during five successive laser pulses. It reveals the realisation of a cycle-dependent quasi-steady state after a transient phase during the first laser pulse.

protective effect of the coating, which hinders the initiation of hot cracks at the surface of the WC-Co cutting insert, as demonstrated by Kirchlechner *et al.* [20], which is of relevance when considering the application of hard metals *e.g.* in metalworking operations. A similar effect was observed *ex-situ* in the case of CrN-coated steel. A further effect apparent in Fig. 8b, is the stepwise decrease of the maximum compressive stress values with the increasing number of applied pulses. This observation can be interpreted by the cyclic sample heating, reducing the lateral temperature gradient and subsequently also the compressive thermal stresses imposed on the irradiated spot by the surrounding material.

Furthermore, it is interesting to observe that the values of integral breadth belonging to individual hkl reflections are differently affected by the rapid local temperature changes within the sample. During heating up from 25 °C to 1300 °C, $\beta^{311,T}$ decreased only by $\sim 25\%$, while $\beta^{114,T}$ changed by $\sim 80\%$ (Fig. 7). The unequal changes in the broadening of the WC hkl reflections indicated anisotropic plastic deformation within the WC hexagonal crystal accompanied by anisotropic annihilation and formation of structural defects. As discussed by Östeberg *et al.* [21], there exist several plastic deformation mechanisms in hexagonal WC crystals, including plastic deformation by dislocation climb, glide and WC/WC grain boundary sliding. Transmission electron microscopy studies on plastically deformed samples confirmed that WC plastic deformation is a highly anisotropic process, occurring only along a limited number of families of crystallographic planes [21, 27]. Hence, the observed differences in the evolution of $\beta^{hkl,T}$ in Fig. 7 between various reflections can be interpreted referring to this anisotropic property of WC. It is supposed that the laser pulses resulted in the formation of tensile and compressive stresses in the WC phase, which are partly relaxed by particular slip mechanisms [21].

The development of $\sigma^{\text{avg},T}$ as a function of measured sample temperature is presented in Fig. 9c. The data show the transient behaviour of $\sigma^{\text{avg},T}$ during the heating up phase of the first applied laser pulse, starting in the compressive domain. For the successive pulses, a quasi-steady state of the hysteresis loops arises, with minor shifts of $\sigma^{\text{avg},T}$ towards higher tensile stress values for every pulse during cooling down, while during the heating up phase a shift of the cycle-dependent $\sigma^{\text{avg},T}$.

Conclusions and outlook

Time-dependent data of in-plane strains and stresses collected during *in-situ* laser pulse experiments indicated the formation of compressive and tensile stresses at 50 ms time resolution within the laser pulsed spot, with magnitudes decreasing and increasing with the number of applied pulses, respectively. Importantly, the *in-situ* stress and peak broadening values (Figs. 6–8) indicate the onset of plastic

deformation of both the Co and the WC phase at temperatures above $\sim 750^\circ\text{C}$, occurring during every applied heating cycle. Methodologically, the synchrotron diffraction set-up allowed the study of the complex stress build-up and relaxation in coated locally thermo-shocked WC-Co inserts at millisecond time resolution and revealed anisotropic microstructural processes accompanying reversible microstructural transition mechanisms.

Acknowledgements

The authors gratefully acknowledge the financial support under the scope of the COMET program within the K2 Center *Integrated Computational Material, Process and Product Engineering* (IC-MPPE) (Project No. 859480).

This program is supported by the Austrian Federal Ministries for Transport, Innovation and Technology (BMVIT) and for Digital and Economic Affairs (BMDW), represented by the Austrian research funding association (FFG), and the federal states of Styria, Upper Austria and Tyrol.

References

- [1] V. Sarin, *Comprehensive Hard Materials*, Elsevier, 2014.
- [2] G. Kirchhoff, T. Göbel, H. A. Bahr, H. Balke, K. Wetzig, K. Bartsch, *Damage analysis for thermally cycled (Ti,Al)N coatings – estimation of strength and interface fracture toughness*, Surf. Coat. Technol. 179 (2004) 39–46.
- [3] G. Abadias, E. Chason, J. Keckes, M. Sebastiani, G. B. Thompson, E. Barthel, G. L. Doll, C. E. Murray, C. H. Stoessel, L. Martinu, *Review Article: Stress in thin films and coatings: Current status, challenges, and prospects*, J. Vac. Sci. Technol. A 36 (2018) 020801.
- [4] T. Tepperneegg, T. Klünsner, P. Angerer, C. Tritremmel, R. Ebner, C. Czettl, J. Keckes, R. Pippan, *Residual stress and damage in coated hard metal milling inserts*, Adv. Tungsten, Refract. Hardmaterials IX – Proc. 9th Int. Conf. Tungsten, Refract. Hardmaterials, 2014.
- [5] T. Tepperneegg, P. Angerer, T. Klünsner, C. Tritremmel, C. Czettl, *Evolution of residual stress in Ti–Al–Ta–N coatings on hard metal milling inserts*, Int. J. Refract. Met. Hard Mater. 52 (2015) 171–175.
- [6] E. A. Álvarez, J. L. García, C. J. R. González Oliver, *Thermal cycling behavior of thin WC–Co sintered pellets*, Adv. Eng. Mater. 19 (2017) 1600544.
- [7] A. Kasterov, A. Shugurov, M. Kazachenok, A. Panin, C.-H. Cheng, I.-L. Chang, *The effect of laser treatment of WC–Co coatings on their failure under thermal cycling*, AIP Conf. Proc. AIP Publishing LLC, 2016, p. 020083.
- [8] C. Peng, Y. Meng, W. Guo, *Influence of laser shock processing on WC–Co Hardmetal*, Mater. Manuf. Process. 31 (2016) 794–801.
- [9] A. W. Nemetz, W. Daves, T. Klünsner, W. Ecker, T. Tepperneegg, C. Czettl, I. Krajcinovic, *FE temperature- and residual stress prediction in milling inserts and correlation with experimentally observed damage mechanisms*, J. Mater. Process. Technol. 256 (2018) 98–108.
- [10] A. W. Nemetz, W. Daves, T. Klünsner, W. Ecker, J. Schäfer, C. Czettl, T. Antretter, *Cyclic heat-up and damage-relevant substrate plastification of single- and bilayer coated milling inserts evaluated numerically*, Surf. Coat. Technol. 360 (2019) 39–49.

- [11] M. Bartosik, R. Daniel, Z. Zhang, M. Deluca, W. Ecker, M. Stefanelli, M. Klaus, C. Genzel, C. Mitterer, J. Keckes, *Lateral gradients of phases, residual stress and hardness in a laser heated $Ti_{0.52}Al_{0.48}N$ coating on hard metal*, Surf. Coat. Technol. 206 (2012) 4502–4510.
- [12] V. Kostov, J. Gibmeier, F. Wilde, P. Staron, R. Rössler, A. Wanner, *Fast in situ phase and stress analysis during laser surface treatment: a synchrotron x-ray diffraction approach*, Rev. Sci. Instrum. 83 (2012) 115101.
- [13] V. Kostov, *Untersuchungen zur zeitaufgelösten Spannungsentwicklung und Eigenspannungsentstehung beim Laserstrahlstandhärten am Beispiel des Stahls 42CrMo4*, Karlsruhe Institute of Technology, 2014 PHD thesis.
- [14] M. Tkadletz, J. Keckes, N. Schalk, I. Krajinovic, M. Burghammer, C. Czettel, C. Mitterer, *Residual stress gradients in α - Al_2O_3 hard coatings determined by pencil-beam X-ray nanodiffraction: the influence of blasting media*, Surf. Coat. Technol. 262 (2015) 134–140.
- [15] D. Kiefer, J. Gibmeier, F. Beckmann, F. Wilde, *In-situ monitoring of laser surface line hardening by means of synchrotron X-ray diffraction*, Mater. Res. Proc. Materials Research Forum LLC (2017) 467–472.
- [16] D. Kiefer, J. Gibmeier, F. Beckmann, *Fast temporal and spatial resolved stress analysis at laser surface line hardening of steel AISI 4140*, Mater. Res. Proc., Materials Research Forum LLC (2018) 91–96.
- [17] E. Kröner, *Berechnung der elastischen Konstanten des Vielkristalls aus den Konstanten des Einkristalls*, Z. Phys. 151 (1958) 504–518.
- [18] M. Lee, R. S. Gilmore, *Single crystal elastic constants of tungsten monocarbide*, J. Mater. Sci. 17 (1982) 2657–2660.
- [19] M. R. Daymond, *The determination of a continuum mechanics equivalent elastic strain from the analysis of multiple diffraction peaks*, J. Appl. Phys. 96 (2004) 4263–4272.
- [20] C. Kirchlechner, K. J. Martinschitz, R. Daniel, C. Mitterer, J. Donges, A. Rothkirch, M. Klaus, C. Genzel, J. Keckes, *X-ray diffraction analysis of three-dimensional residual stress fields reveals origins of thermal fatigue in uncoated and coated steel*, Scr. Mater. 62 (2010) 774–777.

- [21] G. Östberg, K. Buss, M. Christensen, S. Norgren, H.-O. Andrén, D. Mari, G. Wahnström, I. Reineck, *Mechanisms of plastic deformation of WC-Co and Ti(C, N)-WC-Co*, Int. J. Refract. Met. Hard Mater. 24 (2006) 135–144.
- [22] E. Mittemeijer, U. Welzel, *The ‘state of the art’ of the diffraction analysis of crystallite size and lattice strain*, Z. Kristallog. 223 (9) (2008) 552–560.
- [23] T. Klünsner, S. Marsoner, R. Ebner, R. Pippan, J. Glätzle, A. Püschel, *Effect of microstructure on fatigue properties of WC-Co hard metals*, Procedia Eng. 2 (2010) 2001–2010.
- [24] T. Teppernegg, T. Klünsner, C. Kremsner, C. Tritremmel, C. Czettl, S. Puchegger, S. Marsoner, R. Pippan, R. Ebner, *High temperature mechanical properties of WC-Co hard metals*, Int. J. Refract. Met. Hard Mater. 56 (2016) 139–144.
- [25] C. Kirchlechner, K. J. Martinschitz, R. Daniel, C. Mitterer, J. Keckes, *Residual stresses in thermally cycled CrN coatings on steel*, Thin Solid Films 517 (2008) 1167–1171.
- [26] C. Kirchlechner, K. J. Martinschitz, R. Daniel, M. Klaus, C. Genzel, C. Mitterer, J. Keckes, *Residual stresses and thermal fatigue in CrN hard coatings characterized by high-temperature synchrotron X-ray diffraction*, Thin Solid Films 518 (2010) 2090–2096.
- [27] M. Bl’anda, A. Duszová, T. Csanádi, P. Hvizdoš, F. Lofaj, J. Dusza, *Indentation hardness and fatigue of the constituents of WC-Co composites*, Int. J. Refract. Met. Hard Mater. 49 (2015) 178–183.

List of acronyms

2D	two-dimensional
BF-STEM	bright field scanning transmission electron microscope/microscopy
CAE	cathodic arc evaporation
CCD	charge-coupled device
CS	cross-sectional, cross-section
CSnanoXRD	cross-sectional X-ray nanodiffraction
CTE	coefficient of thermal expansion
CVD	chemical vapour deposition
DESY	Deutsches Elektronen-Synchrotron
DS	Debye-Scherrer
DSC	differential scanning calorimetry
EBSD	electron backscatter diffraction
EM	electron microscope/microscopy
ESRF	European Synchrotron Radiation Facility
FIB	focussed ion beam
FWHM	full width at half maximum
HAADF	high-angle annular dark field
HPDL	high-power diode laser
HT-XRD	high-temperature X-ray diffraction
IPF	inverse pole figure
KB	Kirkpatrick-Baez
MLL	multilayer Laue lens
MPECVD	microwave plasma-enhanced chemical vapour deposition
MW	microwave
NCD	nanocrystalline diamond
NIST	National Institute of Standards and Technology
PCD	polycrystalline diamond
PVD	physical vapour deposition
RT	room temperature
SEM	scanning electron microscope/microscopy
STEM	scanning transmission electron microscope/microscopy
TEM	transmission electron microscope/microscopy
TGA	thermogravimetric analysis
XRD	X-ray diffraction